THE UNIVERSITY *of* EDINBURGH

The interstellar medium in lensed star-forming galaxies at $z \sim 2.5$

Alasdair Thomson

A thesis submitted in fulfilment of the requirements
for the degree of Doctor of Philosophy
to the
University of Edinburgh
May 2013

Abstract

A significant fraction of the star formation density between $z = 1$–3 has been traced to luminous and ultra-luminous infrared galaxies. Among the most extreme objects seen are those identified via surveys at submillimetre wavelengths; the high infrared luminosities ($L_{\rm IR} = 10^{11-13}\,{\rm L}_{\odot}$) of these "submillimetre galaxies" (SMGs) arise due to the reprocessing of UV and optical light from massive, young stars by interstellar dust, and imply star formation rates SFR= 50–2000 $\rm M_{\odot}\,yr^{-1}$.

Such SFRs, combined with the observed increase in number density of SMGs by a factor $\sim 20\times$ out to $z = 2$ make them candidates to be the progenitors of the most massive "red and dead" elliptical galaxies which dominate the cores of clusters in the present day, yet limitations in the technical capabilities of radio and infrared telescopes have long hindered a detailed understanding of these galaxies, and in particular, the physics of the interstellar medium (ISM). Hence the following key questions remain unanswered: (i) how much molecular gas ($\rm H_2$) do SMGs contain, and what are the likely upper-limits on how long they can sustain their present level of activity?; (ii) do the prodigious luminosities of SMGs stem from a common origin, or does the selection criterion return a "mixed bag" of galaxies?; (iii) what are internal kinematics of SMGs, and to what extent do these influence the global and local star-formation (Schmidt-Kennicutt) law?; (iv) is star-formation in distant SMGs distributed across the entire galaxy, or does it occur in isolated clumps?; (v) what are the typical densities and temperatures of star-forming regions in SMGs, and do they adhere to the observed correlation between far-infrared and radio emission in star-forming galaxies?

Recent upgrades to the Karl G. Jansky Very Large Array (VLA), the inauguration of the Atacama Large Millimeter Array (ALMA), and the superlative

legacy of the *Herschel* Space Observatory have jointly provided the toolkit to study the gas and dust emission in distant galaxies in unprecedented detail, and thus to begin to address these fundamental questions.

In this thesis, I present ∼120 hours of new VLA observations of ^{12}CO $J=1-0$ emission – the best tracer of molecular gas – in a sample of four lensed SMGs. The combination of high angular resolution with the VLA and the magnifying effects of gravitational lensing allow the ISM properties of these $z \sim 2.5$ star-forming galaxies to be seen for the first time on sub-galactic scales, implying gas masses of $10^{9-10}\,M_{\odot}$ (subject to the ^{12}CO-luminosity-to-H_2-mass conversion factor, α_{CO}), and demonstrating the presence of an extended, low-excitation gas reservoir. In conjunction with observations of the excited gas phase from the Plateau de Bure Interferometer (PdBI), these new data point to variations in the densities and temperatures of H_2 throughout each galaxy.

The wide bandwidth and phenomenal sensitivity of the VLA yields the first detections of 115-GHz continuum emission at high redshift, which I use in conjunction with well-sampled dust spectra from *Herschel* and data at longer wavelengths from the VLA to decompose the radio spectra of two galaxies into contributions arising from thermal dust emission, optically-thin free-free emission from HII regions, and non-thermal synchrotron emission. From these measurements, estimates of SFR_{radio} are made, providing an independent check on SFR_{IR}, and enabling the degeneracy between the heating of dust due to star formation and that due to hidden AGN activity to be broken. Via this spectral index de-convolution, I find $L[AGN]/L_{IR}$ fractions of 35% and 55% for the two SMGs, in broad agreement with previously published estimates for these sources based on their mid-IR spectral properties.

In the exceptional case of SMM J23152–0102, magnification by the foreground cluster is so extreme ($\sim 32.5\times$) that the VLA synthesised beam traces regions of order ~ 130 pc in the source plane, and identifies a series of cool, dense clumps ($T_k = 30$–70 K; $\log[n(H_2)/cm^{-3}] = 3.6$–$3.9$) within the gas reservoir, which contain between them 10–60% of the total molecular gas of the system. These clumps are offset from the far-infrared/radio correlation, which I argue has implications for their ages.

Declaration

I hereby declare that this thesis entitled "The interstellar medium in lensed star-forming galaxies at $z \sim 2.5$" is not substantially the same as any that I have submitted for a degree or diploma or other qualication at any other University or professional institution. I further state that no part of my thesis has already been or is being concurrently submitted for any such degree, diploma or other qualication.

Except where otherwise stated, the research undertaken in this thesis was the unaided work of the author. Where the work was done in collaboration with others, a significant contribution was made by the author.

The work in Chapter 3 was originally carried out for publication in a peer-reviewed journal[1], and has been subject to minor editing for inclusion in the present thesis in order to maintain consistency of style.

A. Thomson
May 2013

[1]Thomson et al., 2012, MNRAS, 425, 2203

Acknowledgements

This thesis is the culmination of three and a half years' of research in the Institute for Astronomy at the Royal Observatory Edinburgh, and would not have been possible without the help and support of a great many people along the way.

Prime among them are my supervisors, Rob Ivison and Philip Best, who have always made time for me and contributed useful scientific and stylistic suggestions on my work, especially so in the difficult closing stages of my write-up. I'd like to thank Rob especially for demonstrating exceptional patience in teaching his eager newbie the black arts of interferometry, and for having the time and the interest to help me think about and plan for life beyond the PhD. His combination of a prodigious scientific output as well as being an exceptionally nice chap are, and will remain something for me to look up to during the next stages of my career.

I am indebted too to my growing list of collaborators, particularly Ian Smail and Mark Swinbank, whose regular contributions, both tangible and intellectual, have vastly improved the quality of this work, and of me as a researcher. I also extend my thanks to Andrew Baker, Pierre Cox, Alice Danielson, Andy Harris, Jean-Paul Kneib, Steven Longmore, Gustaaf van Moorsel, Roberto Neri, Frazer Owen, Padeli Papadopoulos, Chelsea Sharon and Axel Weiss, whose contributions of data and ideas have greatly enhanced the scope of my science. I thank NRAO for building and operating the VLA, the best radio telescope on the planet and an inspiring place to spend some time, and also STFC, without whose support in the form of a postgraduate studentship I could not have even begun this work.

I would also like to thank my friends and acquaintances, both inside and outside of ROE. Vinodiran Arumugam, Victoria Bruce, Peter Gibbons and Jack Mayo; it's been a pleasure sharing an office with you all this past year. I don't know how any of us would have got through the year without a constant supply

of amusing YouTube videos to break the tension! To the wider ROE community and to the people of Edinburgh; thank you for making Edinburgh such a great place to work and play. To Thomas Tyrrell and Alan Wilson; thank you for our continuing friendship, for your support and encouragement, and for making our weekly sci-fi nights something to look forward to.

Lastly, I would like to thank my family for their support and encouragement. Grant, your interest in science once inspired a wee boy to choose physics and chemistry at school. Thanks for setting me off on the right path, and for being a decent enough big brother in the 15 or so years since then! Karen, thank you for putting up with me, for listening to me when I felt the need to rant, and for being there when I needed you to pick me up. And finally, to Mum and Dad, who have been my role-models for hard work, persistence and personal sacrifice, who have instilled in me the inspiration to set high goals, and given me the opportunity to achieve them.

This thesis is dedicated to the memory of my father, Kenny Thomson (1944–2013), for inspiring my fascination with nature and science, and for working tirelessly to allow me to fulfil my ambitions.

Contents

List of Figures

List of Tables

Chapter 1

Introduction

1.1 Island universes and star formation throughout cosmic history

The Universe today is comprised of billions of galaxies of varying colour, morphology, mass and age, with widely differing star formation histories, star formation rates, varying levels of active galactic nuclear (AGN) activity and varying quantities of interstellar gas and dust. One of the key goals of modern astronomy is to understand the range of processes by which this menagerie of galaxies was assembled, and the ways in which galaxies selected on the basis of different observational techniques can be related to each other in a unified, self-consistent model of galaxy formation and evolution.

Our own galaxy, the Milky Way, appears to us as a glowing band of light stretching from horizon to horizon across the night sky. Its name derives from the Hellenistic *galaxías kýklos*, or "milky circle", and was described by Democritus (*c.* 460–370 BC) as *"the splendour which ariseth from the coalition of many small bodies, which being firmly united amongst themselves, do mutually enlighten one another"* (Plutarch, *c.* 80 AD). In 1610 AD, Galileo Galilei published the results of his first telescopic investigation into the night sky, his *Sidereus Nuncius*, and showed that the Milky Way was indeed comprised of millions of individual stars too distant to be resolved individually without the aid of a telescope. By the middle of the 18^{th} Century, the philosopher Immanuel Kant had demonstrated that the Milky Way could exist as a self-gravitating, rotating disc, and in 1784, using observations made with his "40 foot" telescope, William Herschel estimated

its extent to be $\sim 5\,\mathrm{kpc}$ (Leverington, 1995; Binney & Merrifield, 1998). Kant also began to speculate that many of the dim "nebulae" that were becoming apparent in telescopic studies were in fact stellar systems similar in nature to the Milky Way, but at much greater distances – "island universes".

Controversy regarding the nature and provenance of these "nebulae" persisted (Shapley, 1921; Curtis, 1921) until Edwin Hubble's (1929) application of the established period-luminosity relation for Cepheid variable stars, which determined for the first time an accurate distance of 300 kpc to M 31 – far greater than any estimate of the size of the Milky Way – and thus showed definitively that it, and by inference other "nebulae" were massive sources at great distance, distinct from the Milky Way.

In the time since Hubble's discovery, hundreds of billions of distant galaxies of differing morphologies have been discovered. The Hubble sequence, or "tuning fork" diagram (Hubble, 1926) remains one of the most widely-used morphological classification schemes to this day. In this scheme, (Fig. 1.1) galaxies are broadly classified based on their optical appearance in one of three categories:

1. Early-type/elliptical galaxies (E0 – E7), typically red in colour – denoting an evolved, dormant stellar population, and characterised by their generally elliptical shape and a light profile that decreases with radius from the centre of the galaxy.

2. Spiral galaxies (Sa – Sc and SBa – SBc), consisting of a red, spheroidal bulge of old stars, orbited by bluer spiral arms of various intricacy containing gas and a generally younger stellar population, the sites of ongoing star-formation. Spiral galaxies are further sub-divided into "normal spirals", in which the spiral arms coil around the central bulge and "barred spirals" in which a clear central bar produces longitudinal asymmetry.

3. Lenticular galaxies (S0), which sit at the morphological fork between spiral and elliptical galaxies. Lenticular galaxies typically consist of a bright central bulge surrounded by an extended disk-like structure, but without any obvious spiral arm pattern and with little measurable star-formation activity.

A fourth category exists – (4) irregular galaxies – to accommodate galaxies

that do not fit on the "tuning fork" diagram, due to their apparent lack of structure.

Typically, galaxies are not randomly distributed on the sky, but instead cluster in massive gravitationally-bound groups, consisting of up to tens of thousands of galaxies, separated by hot intra-cluster gas and with typically a high fraction of the total cluster mass in the form of dark matter.

Studying the census of galaxies that make up such clusters in the local Universe, we see a preponderance of massive elliptical galaxies with high stellar masses ($\geq 10^{11}\,\mathrm{M}_{\odot}$; e.g. Forte et al., 2012) but with low present-day star formation rates (SFR: $\sim 1\,\mathrm{M}_{\odot}\,\mathrm{yr}^{-1}$). Had these galaxies undergone such passive evolution throughout their lives, it would have taken multiple times the age of the Universe to form their stellar populations. The obvious implication of this is that present day massive galaxies formed the bulk of their stars more rapidly at earlier epochs. It has long been established that the giant elliptical galaxies that lie at the heart of nearby clusters already had a significant stellar content prior to $z \sim 1$ (e.g. Ellis et al., 1997; Lubin et al., 1998), the passive evolution we see now being only the latest snapshot in their evolutionary lineage. We are thus faced with an implied evolution in the nature of the star-forming galaxy population with redshift, with the evolutionary progenitors of local elliptical galaxies being required to have had much higher star-formation rates in the past than their descendants do today.

In order to investigate the build-up of stellar mass in the Universe, it is therefore necessary to determine the nature of the galaxies in which star formation most conspicuously takes place, as a function of redshift. Numerous studies (e.g. Caputi et al., 2006, 2007; Serjeant et al., 2008, etc.) have shown that massive [Ultra–]Luminous Infrared Galaxies ([U]LIRGs: $L_{\mathrm{IR}} > 10^{10-11}\mathrm{L}_{\odot}$) play an increasingly important role in mass assembly at higher-redshift, with only a fraction of massive ($M_{\star} > 10^{11}\,\mathrm{M}_{\odot}$) galaxies in the local Universe having infrared luminosities $L_{\mathrm{IR}} > 10^{11}\,\mathrm{L}_{\odot}$ compared to $\sim 50\%$ at $z \geq 2$. The large L_{IR} of such galaxies arises due to emission from interstellar dust, which is warmed by the absorption of UV/optical photons that may themselves originate either as a result of prodigious star formation events, powerful AGN, or some combination of the two (e.g. Pope et al., 2008). Light emitted from a galaxy at redshift z is stretched by a factor $(1+z)$ *en route* to the observer, such that an (U)LIRG-like galaxy whose spectral energy distribution (SED) peaks at $\sim 250\,\mu\mathrm{m}$ at $z \sim 2.5$

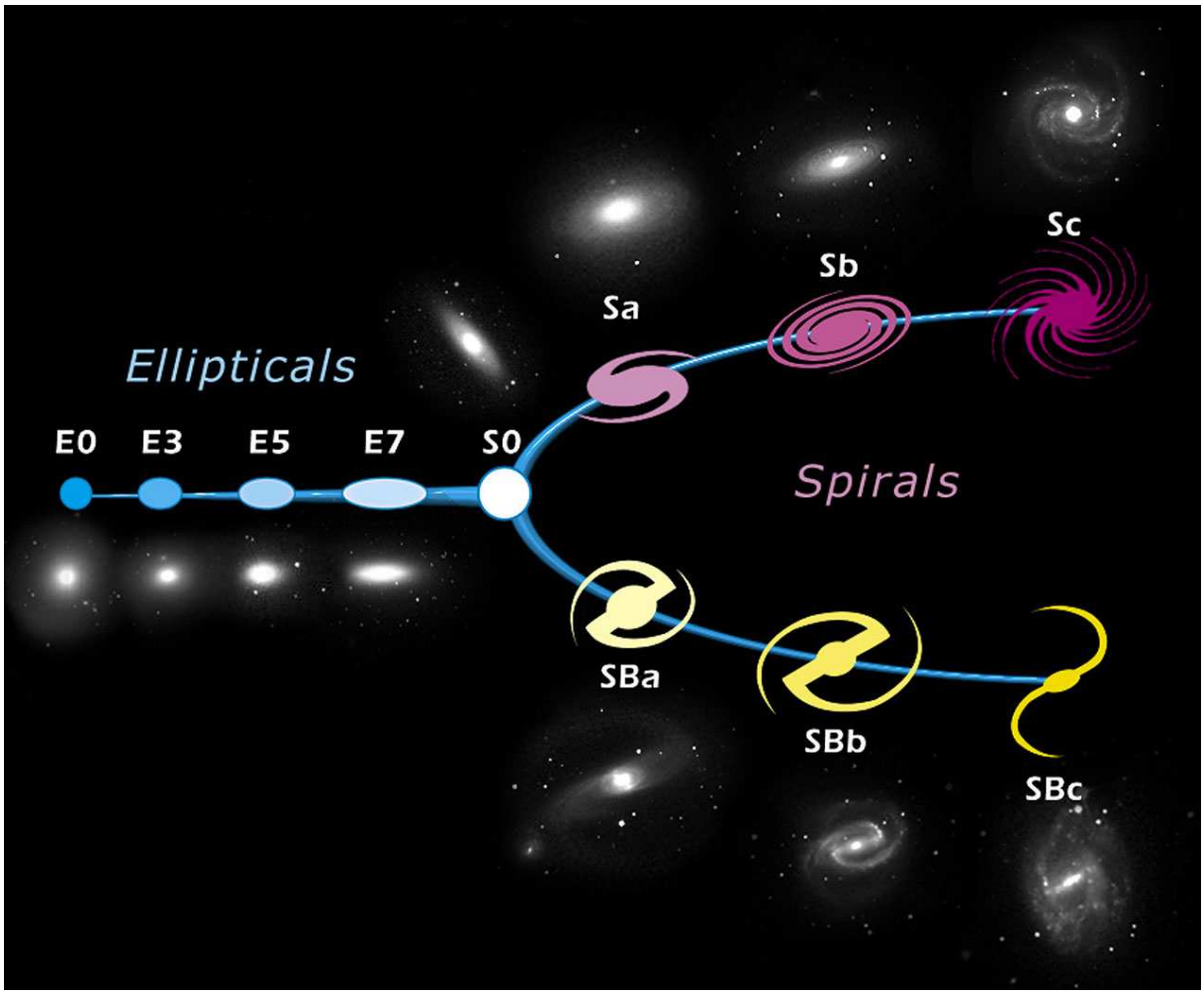

Figure 1.1: Hubble's (1926) tuning fork diagram for the classification of galaxies based on visible morphology. The Hubble Sequence is one of the most commonly-used morphological classification schemes for galaxies to this day, delineating "early-type" elliptical galaxies (E0 – E7) from barred (SBa – SBc) and non-barred (Sa – Sc) "late type", or spiral galaxies. Figure adapted from original at `http://www.spacetelescope.org/images/heic9902o/`

is detectable to us in the submillimetre (submm) band at $\sim 850\,\mu$m.

Observations of the unresolved infrared/submillimetre extra galactic background with the Far Infrared Spectrophotometer (FIRAS) on-board the Cosmic Microwave Background Explorer (COBE) satellite in the mid-1990s showed that as much light has been emitted through cosmic history at infrared and submillimetre wavelengths as at optical/ultraviolet (UV) wavelengths (Fixsen et al., 1998; Smail et al., 2000a). Nevertheless, the difficulties of building submillimetre telescopes – functioning as they do on the technological boundary between the photon-counting techniques of optical telescopes and the antenna-based techniques of radio astronomy – precluded any detailed, systematic search for the individual sources that gave rise to this unresolved background emission until the revolutionary Submillimetre Common-User Bolometer Array (SCUBA: Holland et al., 1999) detector, built at the Royal Observatory Edinburgh, was mounted on the 15-m James Clerk Maxwell Telescope (JCMT) on Mauna Kea, Hawaii. The 2.5-arcmin field of view and 15-arcsec resolution of SCUBA at 850-μm facilitated the discovery of a large population of infrared-bright ($L_{\rm IR} \geq 10^{12}\,{\rm L}_{\odot}$), dust-obscured, high-redshift ($z > 2$), adolescent star-forming galaxies. These galaxies – the submillimetre galaxies (SMGs) – have been found to be responsible for a significant fraction of the energy-release of all galaxies over cosmic history (e.g. Smail et al., 1997; Barger et al., 1998; Greve et al., 2005; Kovács et al., 2006).

In this thesis, I use radio interferometric imaging obtained with the Karl G. Jansky Very Large Array (VLA) in New Mexico to study molecular gas (the fuel for potential future star-formation) and ionised gas (which traces *recent* star formation) in a sample of lensed SMGs with a view to determining the masses and excitation conditions of their molecular gas reservoirs, and in order to determine the relative AGN contribution to the bolometric luminosity. In the following section (§ 1.2), I present a summary of the concordance cosmological model, which provides the framework within which observations of distant galaxies are interpreted. In § 1.3, I discuss the key observational properties of SMGs, summarise some of the important developments there have been in their study in the 15 years since the earliest SCUBA detections, and highlight areas of ongoing debate as to their nature and the extent to which they contribute to the build-up of stellar mass in the Universe. In § 1.4 a prescription for modelling the state

of the interstellar medium (ISM) in galaxies via molecular line observations is presented. Finally in this chapter, in § 1.5 I outline the scientific aims of this thesis.

1.2 An observer's toolkit for cosmology

In order to make sense of observations of distant galaxies, it is necessary to analyse them within the context of a cosmological framework which relates redshift, age and look-back time, which enables us to relate the intrinsic luminosities of objects to the flux we observe via some measure of the luminosity distance, and define the relationship between angular separation on the sky and physical (angular-diameter) distance between objects seen at a redshift z.

Since the confirmation in the last century of a Universe beyond our own Milky Way, a remarkably robust "Concordance" model of cosmology has emerged, in which is contained the framework for the interpretation of such observations.

In the following, I aim to provide a brief motivation for some of the key cosmological parameters used throughout the rest of this thesis; for a full treatment of the underlying physics, see Peacock (1998) and Combes et al. (2006).

1.2.1 The scale factor and Hubble's constant

In a homogeneous and isotropic Universe, obeying the Copernican Principle, we can envisage a team of observers sitting in different galaxies, each of which is at rest with respect to the local velocity field, such that each observer sees all the others recede at a speed that is linearly proportional to their distance. That is to say, the separation vectors between each of the observers at some time t are just the separation vectors at some reference time t_0, multiplied by a time-dependent scale factor:

$$\mathbf{x}(t) = R(t)\mathbf{x}(t_0) \tag{1.1}$$

Observational evidence from Slipher (1917) and Hubble (1926) showed that the recession velocities of galaxies at moderate distance (outside of the local group) scaled linearly with their distance:

$$v = HD \tag{1.2}$$

The constant of proportionality H has become known as "Hubble's constant", and was estimated by Hubble himself to be $\sim 500\,\mathrm{km\,s^{-1}\,Mpc^{-1}}$. Differentiating Equation 1.1 and comparing with 1.2, we see that H is in fact a function of time, and is the ratio between the first derivative of the scale constant, and the value of the scale constant itself at time t:

$$H(t) = \frac{\dot{R(t)}}{R(t)} \tag{1.3}$$

1.2.2 The Robertson–Walker metric

Suppose each of our distant observers marks the passage of time with a clock, and suppose they synchronise their clocks via the exchange of light signals; then we can define the global time coordinate, t, and realise that the time intervals dt measured by such observers between events are then related to the proper time intervals $d\tau$ via a metric of the form

$$c^2 d\tau^2 = c^2 dt^2 - R^2(t)\left[f^2(r)dr + g^2(r)d\psi^2\right] \tag{1.4}$$

in which we represent distances as the product of a time-dependent scale factor $R(t)$ and a time-independent co-moving coordinate r. The functions $f(r)$ and $g(r)$ may be constrained by a suitable choice of radial coordinate, while in spherical polar coordinates, the transverse distance element $d\psi^2 = d\theta^2 + \sin^2\theta d\phi^2$.

Thus, the Robertson–Walker Metric, derived independently by Robertson (1935) and (Walker, 1937) is commonly written as

$$c^2 d\tau^2 = c^2 dt^2 - R^2(t)\left[dr^2 + S_k^2(r)(d\theta^2 + \sin^2\theta d\phi^2)\right] \tag{1.5}$$

where $S_k^2(r)$ is a tri-valued function representing angular distances, and has the following three possible values depending on the nature of spatial curvature:

$$S_k^2(r) = \begin{cases} \sin r & \text{if } k = 1 \text{ (positive curvature; closed Universe)} \\ r & \text{if } k = 0 \text{ (zero curvature; flat Universe)} \\ \sinh r & \text{if } k = -1 \text{ (negative curvature; open Universe)} \end{cases} \tag{1.6}$$

1.2.3 Redshift, distance and time

Photons travel along geodesic paths, for which the angular terms in the Robertson–Walker metric are zero, and since they travel at the speed of light, proper time intervals $d\tau = 0$. Hence, the Robertson–Walker metric for photons takes on a particularly concise form:

$$0 = c^2 dt^2 - R^2(t) dr^2 \Rightarrow \int_{t_{\rm emit}}^{t_{\rm obs}} \frac{cdt}{R(t)} = -\int_{r_{\rm emit}}^{0} dr \tag{1.7}$$

where $t_{\rm emit}$ and $t_{\rm obs}$ are the times at which the photon is emitted and observed respectively, and $r_{\rm emit}$ is the radial distance between source and observer. For a galaxy that is co-moving (i.e. at rest with respect to the local Hubble flow), then $r_{\rm emit} \equiv r_0$ is an unchanging quantity of time. Since a photon emitted some time Δt later will satisfy an analogous relationship to 1.7 with the same right hand side, we have that

$$\int_{t_{\rm emit}}^{t_{\rm obs}} \frac{cdt}{R(t_{\rm emit})} = \int_{t_{\rm emit}+\Delta t}^{t_{\rm obs}+\Delta t} \frac{cdt}{R(t)} \tag{1.8}$$

from which we have that

$$\frac{\Delta t_{\rm emit}}{R(t_{\rm emit})} = \frac{\Delta t_{\rm obs}}{R(t_{\rm obs})} \tag{1.9}$$

If an astrophysical source emits radiation with frequency $\nu_{\rm emit} = 1/\Delta t_{\rm emit}$, then we have that

$$\frac{\nu_{\rm emit}}{\nu_{\rm obs}} = \frac{R(t_{\rm obs})}{R(t_{\rm emit})} \equiv 1 + z \tag{1.10}$$

Redshift z is a measure of the amount by which a photon's frequency has decreased between being emitted and being observed, and is hence also a measure of the amount by which the scale factor has changed, and of the amount of time that has elapsed in between.

1.2.4 Expansion dynamics; the Friedmann Equation

The dynamics of cosmic expansion are described by the Friedmann equation, which is the equation of motion governing the growth of the scale factor:

$$\dot{R}^2 - \frac{8\pi G}{3}\rho R^2 = -kc^2 \tag{1.11}$$

One of the most important implications of the Friedmann equation is that spatial curvature k is related to cosmic density, and that there exists a critical density

$$\rho_c = \frac{3H^2}{8\pi G} \tag{1.12}$$

for which the curvature $k = 0$; a flat Universe. Defining $\Omega \equiv \rho/\rho_c$, we have that for $\Omega > 1$, $k = 1$ (positive curvature; a spatially-closed), whereas for $\Omega < 1$, $k = -1$ (negative curvature; an open Universe).

The cosmic density ρ consists of contributions due to matter (which scales as $\rho \propto R^{-3}$), radiation ($\rho \propto R^{-4}$) and vacuum energy (ρ =constant). Bearing this in mind, and introducing the dimensionless scale factor $a \equiv R/R_0$, the density term in the Friedmann equation may be re-written as

$$\frac{8\pi G\rho}{3} = H_0^2(\Omega_m a^{-3} + \Omega_r a^{-4} + \Omega_v) \tag{1.13}$$

Substituting Equation 1.13 in to the zero-curvature case of Equation 1.11 and using the relationship established between the scale factor and redshift (1.10), we have the important relation that

$$H^2(z) = H_0^2\left[\Omega_m(1+z)^3 + \Omega_r(1+z)^4 + \Omega_v\right] \tag{1.14}$$

1.2.5 Distance estimators in cosmology

Measurements of the present day values of Ω_v, Ω_m and Ω_r in addition to an accurate determination of H_0 thus allow us to determine the value of $H(z)$ at all earlier (and future) epochs.

This is an important connection to make, in that it allows us to establish a mapping of observed redshift to co-moving distance, so giving the observable Universe a physical scale. Since the radial equation of motion of a photon is $Rdr = cdt = cdR/(dR/dt) = cdR/(RH)$, we have the general relation that:

$$R_0 dr = \frac{c}{H(z)} dz \tag{1.15}$$

in which the relationship 1.10 has again been used. In the zero-curvature case, this becomes:

$$\boxed{R_0 dr = \frac{cdz}{H_0\sqrt{\left[\Omega_m(1+z)^3 + \Omega_r(1+z)^4 + \Omega_v\right]}}} \tag{1.16}$$

With the co-moving distance thus defined, we can define two additional useful cosmological distance scales relatively;

Angular luminosity distance

In Euclidean space, the relationship between the luminosity L of an isotropically emitting source and the observable flux S at distance D is

$$S = \frac{L}{4\pi D^2} \tag{1.17}$$

where $4\pi D^2$ is the area of the imaginary sphere, centred on the source, on which we as observers sit. This relationship holds for isotropic and homogeneous, expanding spaces of arbitrary geometry, providing we deduce an appropriate functional form for D. First, consider that in curved space, photons travel along geodesics; hence $D \rightarrow R_0 S_k(r)$. Next, we recognise that expansion affects the received flux in two ways; first by reducing the arrival rate of photons, and secondly by increasing their wavelength (hence decreasing the energy carried by each photon: Hogg, 1999). Each of these effects implies a division in the observed flux of $(1+z)$, hence

$$S = \frac{L}{4\pi R_0^2 S_k(r)^2 (1+z)^2} \tag{1.18}$$

By analogy with Equation 1.17, we can define the luminosity distance D_L:

$$\boxed{D_L \equiv R_0 S_k(r)(1+z)} \tag{1.19}$$

Angular diameter distance

The related concept of angular diameter distance gives the ratio of an object's physical transverse size to the angle it subtends on the sky.

If we consider a distant galaxy to have emitted light at some time $t_{\rm then}$ which is only reaching us now, then the proper distance D_A subtended by the infinitesimal angular distance $d\psi$ is given by

$$D_A d\psi \equiv R(t_{\rm then}) S_k(r) d\psi \tag{1.20}$$

Then from identity 1.10,

$$D_A d\psi = \frac{R_0 S_k(r)}{1+z} d\psi \tag{1.21}$$

Thus the angular diameter distance is

$$\boxed{D_A = R_0 S_k(r)(1+z)^{-1}} \tag{1.22}$$

1.2.6 Concordance cosmology

Large surveys of galaxy clustering such as the 2 degree Field Galaxy Redshift Survey (2dFGRS) and Sloan Digital Sky Survey (SDSS) and efforts to map the anisotropies of the cosmic microwave background (CMB) with the *COBE*, *WMAP* and most recently *Planck* satellites have jointly developed a paradigmatic model of the Universe, which is flat, dominated by cold dark matter and vacuum energy (Λ), and in which structure on the largest scales ($> 1\,$Mpc) arises due to the hierarchical merging of dark matter halos along sites of primordial cosmological over-density.

Springel et al. (2005) presented the results of a large-scale cosmological simulation developed within this paradigm, following 2160^3 dark matter particles in a $500\,h^{-1}\,$Mpc box from $z = 127$ to the present day – the *Millennium Simulation* – in which the spatial clustering, dynamics and intrinsic properties of a large number of halos were matched to the available observational evidence.

The best fitting combination of physical parameters from the Seven Year *WMAP* data release suggest a present-day value for the Hubble constant $H_0 = 70\,\mathrm{km\,s^{-1}\,Mpc^{-1}}$, and $\Omega_m = 0.27$ and $\Omega_\Lambda = 0.73$ (Jarosik et al., 2011); hereafter, all references to distance made in this thesis are made with this combination of physical parameters in mind.

1.3 Submillimetre galaxies

Submillimetre galaxies (SMGs) are extragalactic sources with observed flux densities $S_{850\mu m} \geq 3$–$5\,\mathrm{mJy}$. Lying at cosmological redshifts ($z > 1$: Chapman et al., 2005), this emission originates in the rest-frame far-infrared, the two main sources of which are thermal continuum emission from cool dust grains and spectral line emission from atomic and molecular gas in the ISM. Assuming that the 850-μm flux in SMGs arises mainly due to thermal dust emission, rest-frame luminosities $L_{\mathrm{IR}} > 10^{12}\,\mathrm{L}_{\odot}$ are implied (e.g. Blain et al., 2002), making SMGs among the most IR-luminous galaxies at any redshift.

In spite of their intrinsic brightness in the far-infrared, and the improving sensitivity of submillimetre telescopes, gravitational lensing – either by chance, line-of-sight foreground galaxies (e.g. Rowan-Robinson et al., 1991; Graham & Liu, 1995; Negrello et al., 2010) or by deliberate exploitation of massive foreground clusters (e.g. Smail et al., 1997; Kneib, 2010) – remains a powerful tool for uncovering populations of such distant star-bursting galaxies. Usually buried in the confusion noise, these galaxies become relatively easy to detect and spatially resolve when lensed, by virtue of the magnification they experience. Surveys of such lensed objects have produced statistical samples of SMGs, from which star formation rates (SFRs) of $\geq 500\mathrm{M}_{\odot}\,\mathrm{yr}^{-1}$ (Pope et al., 2008), stellar masses $\sim 10^{11}\,\mathrm{M}_{\odot}$ (Hainline et al., 2011; Michalowski et al., 2012) and molecular gas masses $\geq 3 \times 10^{10}\,\mathrm{M}_{\odot}$ (Genzel et al., 2003; Greve et al., 2005) have been determined, suggesting that SMGs may host sufficient fuel and vigorous-enough star formation to make them significant contributors to the integrated cosmic star formation history of the universe (e.g. Swinbank et al., 2006).

In the following subsections, the key observed properties of SMGs selected with SCUBA and *Herschel* are summarised – including a review of their redshift distribution, dust temperatures, AGN component, star formation rates, stellar and gas masses, number counts, clustering and cosmological significance – and this section concludes with a short discussion of the relation of SMGs to the paradigmatic "main-sequence" of star-forming galaxies (e.g. Daddi et al., 2010; Genzel et al., 2010; Rodighiero et al., 2011).

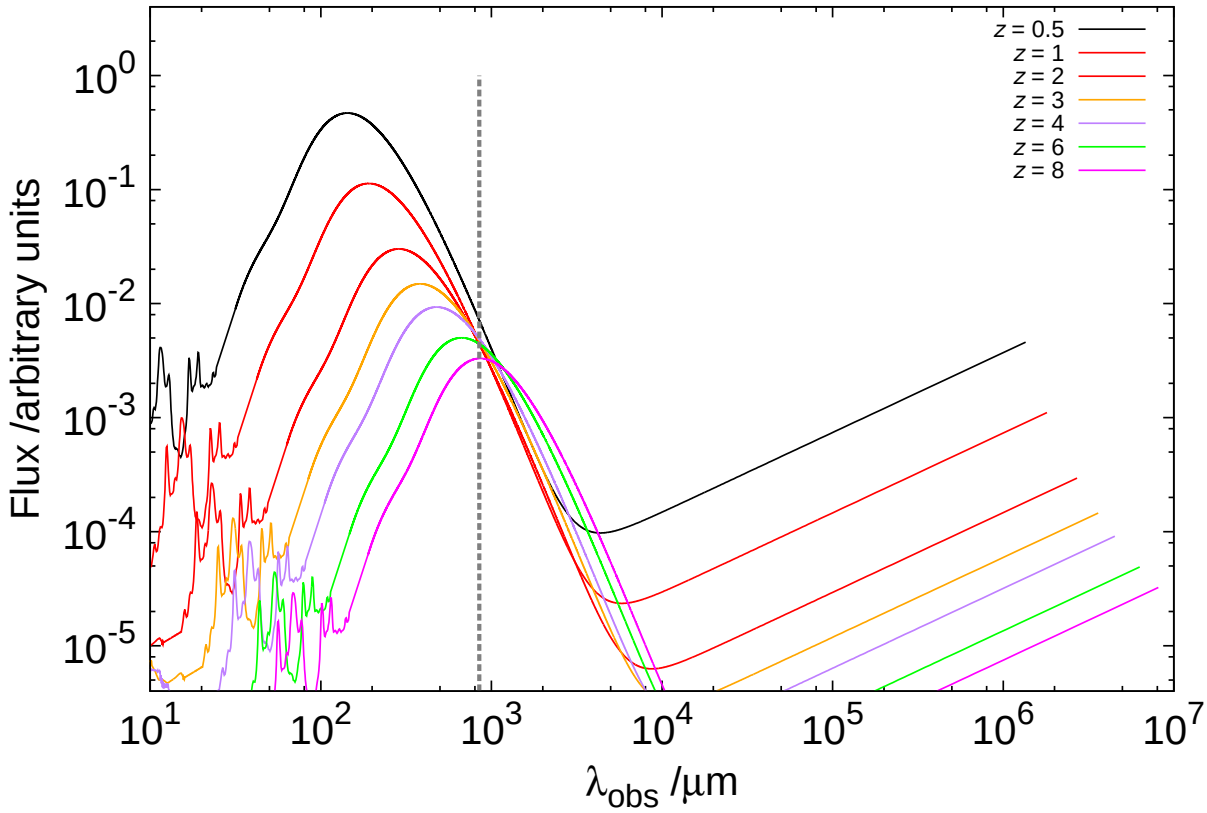

Figure 1.2: Infrared/radio SED of SMM J21352 (Swinbank et al., 2010b; Ivison et al., 2010c) exemplifying negative K-correction - bolometric dimming of the SED as a function of redshift is approximately compensated for at $\lambda_{\rm obs} = 850\mu$m (dotted vertical line) by the shape of the Rayleigh-Jeans tail. Up to $z \sim 8$, the 850-μm band probes a successively brighter portion of the rest-frame SED, negating the bolometric dimming due to inreased distance, resulting in a selection function for SMGs that is more or less flat for $1 < z < 8$.

1.3.1 Redshift distribution

Flux-limited 850-μm selection enables the detection of galaxies between $1 < z < 8$ in a roughly redshift-independent manner, due to the shape of the spectral energy distribution (SED) of far-infrared dust emission and negative K-correction (Fig. 1.2). Negative K-correction compensates for the bolometric dimming of a galaxy as it is moved to higher redshift by the fact that we probe shorter rest-frame wavelength, intrinsically-brighter emission at higher-redshift, until by $z \sim 8$ the peak of the dust spectrum has passed through the 850-μm band, whereupon the submillimetre selection function sharply turns over.

The poor resolution of early submillimetre telescopes long hindered attempts to determine SMG positions to greater than $\sim$ 10-arcsec accuracy, making it difficult to identify optical and near-IR counterparts and determine their redshifts. However, exploitation of the strong correlation between the far-infrared (FIR) and radio flux densities of star-forming galaxies – the far-infrared/radio correlation (FIRRC; Helou et al., 1985; Condon, 1992) – has enabled the positions of many unresolved submillimetre sources to be determined to sub-arcsecond accuracy in deep radio maps (e.g. Ivison et al., 1998; Smail et al., 2000b), thus providing the astrometric anchorage necessary to conduct follow-up studies at multiple wavelengths.

The linear far-infrared/radio correlation in star-forming galaxies applies over several orders of magnitude in luminosity ($10^{9}\mathrm{L}_{\odot} < L_{\mathrm{IR}} < 10^{12.5}\mathrm{L}_{\odot}$), and on scales ranging from those of individual giant molecular clouds (GMCs) up to the most massive star-bursting galaxies. This remarkable correlation is canonically interpreted as being due to the way in which young, massive stars indirectly give rise both to: (i) infrared emission (as their UV photons are absorbed and re-radiated by dust grains); and (ii) to non-thermal radio continuum emission as their eventual supernovae accelerate cosmic ray electrons to relativistic speeds, which radiate as they encounter interstellar magnetic fields (Condon, 1992; Helou & Bicay, 1993; Lacki & Thompson, 2010).

For "normal" galaxies obeying the far-infrared radio correlation (i.e. those not hosting a dominant AGN), the spectral index $\alpha_{1.4}^{350}$ between 850 μm (350 GHz) and 1.4 GHz emission may be used as a coarse redshift estimator (Carilli & Yun, 1999). This is possible because of the relative shapes of the SED at 850 μm and 1.4 GHz, where emission observed in the former band benefits from negative K-correction while radio continuum fluxes do not; however this is subject to large uncertainties ($\Delta z \sim 0.5$) due to the degeneracy between redshift and dust temperature T_{d}.

The first spectroscopic redshift surveys of SMGs by Chapman et al. (2003) and Chapman et al. (2005) exploited the far-infrared/radio correlation only to the extent that it provided precise astrometry for each submillimetre source via detection of its radio counterpart at sub-arcsecond resolution, enabling some 850 μm-selected sources to be followed up in deep rest-frame UV/optical surveys. Using the Low Resolution Imaging Spectrograph (LRIS: Oke et al., 1995) on the Keck I telescope, the median redshift of 73 SCUBA-selected SMGs in eight

survey fields was found to be $< z > \sim 2.3$. However, with the fraction of SMGs detected at radio wavelengths being only 60–80% (Chapman et al., 2005) and the fact that radio fluxes do not benefit from negative K-correction, the survey was implicitly biased against detecting SMGs at redshifts significantly higher than $z \sim 3$. Additionally, the Chapman et al. redshift distribution exhibits a dearth of sources at $z \sim 1.5$, primarily due to the lack of strong spectral features accessible to LRIS at that redshift. In recent deep, multi-wavelength imaging of the COSMOS field, Smolčić et al. (2012) find that 20% of 870-μm-selected SMGs lie at $z > 3$, while individual SMGs are known to exist at $z > 4$ (e.g. Riechers et al., 2010; Cox et al., 2011; Wardlow et al., 2011; Ivison et al., 2013).

1.3.2 Dust temperatures

Dust in galaxies, warmed by absorption of stellar UV/optical photons, re-emits as a "greybody" (flux density $S_{\rm dust} \propto \nu^{\beta} \mathrm{B}_{\nu}$) at far-infrared wavelengths, where

$$B_{\nu} = \frac{2k_{\rm B}T_{\rm d}\nu^2}{c^2} \tag{1.23}$$

is the Planck function in the long-wavelength Rayleigh Jeans limit. The dust temperature $T_{\rm d}$ of a galaxy at a known redshift may be deduced from its infrared SED by producing a library of template dust SEDs in which $T_{\rm d}$ and the spectral index β vary as free parameters, and picking the template which best-fits the observations (Dunne et al., 2000). One may only deduce a temperature once an assumption has been made regarding β or vice-versa, however β is typically assumed on theoretical grounds to lie between 1 – 2 (Hildebrand, 1983), which greatly reduces the parameter space over which fits need be made. For a sample of 104 local submillimetre-bright galaxies detected at 60- and 100-μm with the InfraRed Astronomical Satellite (*IRAS*) and at 850-μm with SCUBA, Dunne et al. (2000) derive mean dust temperatures and spectral indices of $\overline{T_{\rm d}} = 35.6 \pm 4.9\,\mathrm{K}$ and $\overline{\beta} = 1.3 \pm 0.2$ respectively.

The thermal nature of far-IR SMG SEDs renders the problems of determining temperatures and photometric redshifts degenerate, as both an increase in redshift and a decrease in temperature produce similar effects in the observed SED (and vice versa; Blain et al., 2002). In order to deduce temperatures from dusty

greybody fits to infrared and submillimetre observations of distant sources, an estimate of the redshift from some other method – e.g. spectroscopy (Chapman et al., 2005), or via the radio-to-submillimetre spectral index (Carilli & Yun, 1999) – is required.

1.3.3 Active galactic nuclei

When interstellar dust is bathed in UV/optical light, it is liable to reprocess and re-emit that flux at infrared wavelengths regardless of whether the source of incident light is predominantly stellar, or owing to an enshrouded and accreting super-massive black hole (SMBH) – an AGN (e.g. Dunne et al., 2000; Alexander et al., 2005; Floc'h & Cosmos Collaboration, 2011). It is thus not immediately clear from only IR/sub-mm data to which of these processes SMGs owe their prodigious bolometric luminosity. Studies in different wavelength regimes are necessary to break the star-formation/AGN degeneracy, including estimates derived from the strengths of Polycyclic Aromatic Hydrocarbon (PAH) emission lines in the mid-IR band (e.g. Pope et al., 2008) and hard X-Ray emission (e.g. Alexander et al., 2005). Typically such studies indicate that the majority ($\sim 75\%$) of (radio-selected) SMGs host AGN, but that they do not dominate the bolometric output. In Chapter 3 of this thesis and in Thomson et al. (2012), I present a new method for estimating the AGN contribution to $L_{\rm IR}$ in individual SMGs via the $\sim 115\,$GHz optically-thin free-free radio emission, and corroborate the claim that AGN can provide a significant, but typically sub-dominant contribution to the bolometric output of SMGs.

1.3.4 Star formation rates

In passively-evolving disk galaxies, where there are relatively few young stars and stars of a wide range of ages and mass may contribute to the heating of dust in equal measure, the relationship between dust-heating and the star formation rate (SFR) is non-trivial. In starburst galaxies, however, a small population of young, OB stars whose spectra peak in the UV ($\mathrm{T} \sim 30{,}000\,\mathrm{K}$) can dominate the thermal dust emission of the entire galaxy. As these massive stars are by definition short-lived, there is thus a direct coupling between the infrared luminosity ($L_{\rm IR}$) and the recent star formation rate (SFR), which is most commonly expressed via the

Kennicutt (1998) conversion factor

$$\frac{\mathrm{SFR_{IR}}}{1\ \mathrm{M_\odot yr^{-1}}} = \frac{L_{\mathrm{IR}}}{5.8 \times 10^9\,\mathrm{L_\odot}} \tag{1.24}$$

which assumes that star-formation occurs in 10–100 Myr bursts, from solar metallicity material, following a 0.1–100 $\mathrm{M_\odot}$ Salpeter IMF, and that star-formation (rather than AGN activity) dominates L_{IR}. Prior to the commissioning of *Herschel*, infrared luminosities in SMGs and other high-z star-forming galaxies were typically determined by extrapolation of mid-infrared, sub-mm or radio observations (Chapman et al., 2005; Pope et al., 2006; Kovács et al., 2010). With the launch of *Herschel* and its coverage with the Photodetecting Array Camera and Spectrometer (PACS) at 55–210-μm and SPIRE at 194–672-μm, direct measurements of L_{IR} over the peak of the dust SED in $z > 2$ star-forming galaxies have become possible, reducing the observational uncertainties associated with infrared-derived SFRs (Elbaz et al., 2011), though systematic uncertainties inherent in the Kennicutt (1998) conversion factor itself remain.

The prodigious L_{IR} typical of SMGs ($> 10^{12}\,\mathrm{L_\odot}$) thus corresponds to SFR $\geq$ $200\,\mathrm{M_\odot\,yr^{-1}}$, while a handful of submillimetre-detected "hyper-luminous" infrared galaxies (HyLIRGs; $L_{\mathrm{IR}} \geq 10^{13}\,\mathrm{L_\odot}$) have even higher star formation rates – SFR > $1000\mathrm{M_\odot\,yr^{-1}}$– the highest seen in the Universe (Ivison et al., 2013; Riechers et al., 2013).

1.3.5 Stellar masses

The problem of determining stellar masses in distant star-forming galaxies is one of fitting stellar population synthesis models, star-formation histories and AGN models to the observed panchromatic SEDs, taking into consideration the likely effects of extinction in each band due to dust. Using *Spitzer*-IRAC and U, B, V, R, I and z' optical/near-IR measurements of the Chapman et al. (2005) spectroscopically-selected sample, Hainline et al. (2011) determine a mean stellar mass $M_\star \sim 7 \times 10^{10}\,\mathrm{M_\odot}$ for the 70 SMGs. This mean stellar mass estimate is determined by fitting combinations of the Bruzual & Charlot (2003, hereafter BC03) and Maraston (2005, hereafter M05) stellar population synthesis models, with a Kroupa (2001) IMF and star-formation histories (SFH) that

are either instantaneous, continuous, or exponential (SFR(t) $\propto \exp(-t/\tau)$ with $\tau = 0.1, 0.25, 0.5, 1, 2, 5\,\mathrm{Gyr}$) in nature. The main quantitative difference between the BC03 and M05 models is the emphasis placed in the latter on thermally pulsating asymptotic giant branch (TP-AGB) stars, which act to lower the mass-to-light ratio in the near-IR for young stellar populations. For a typical SMG, Hainline et al. (2011) find that 4 of the 6 histories produce χ^2 values with respect to the available photometry within ± 0.1 of each other, and attribute this inability to distinguish between even the most simple star-formation histories as being due a failure to detect the 4000 Å break in any of the spectra, and due to the general difficulty in distinguishing a young, heavily dust-obscured galaxy from an old, unobscured galaxy in broad band photometry (e.g. Shapley et al., 2001).

By contrast, Michalowski et al. (2010) study the *same* objects using photometry from 1.6 μm through to 1.4 GHz, a Chabrier (2003) IMF, the SED templates of Iglesias-Páramo et al. (2007) and fix the star formation law to a hybrid Schmidt-type, ongoing star-formation history (SFR $\propto M_{\mathrm{gas}}$) with a 50 Myr old starburst superimposed to determine a mean $M_\star \sim 4 \times 10^{11}\,\mathrm{M}_\odot$ – a factor $\sim 6\times$ higher than the Hainline et al. (2011) measurements for the same sample. Variations in the choice of IMF and stellar population synthesis model each contribute factors $\sim 2\times$ uncertainty to the integrated stellar mass in SMGs (Michalowski et al., 2012) and remain controversial between groups. Michalowski et al. (2012) further argue that the single-component SFH employed by Hainline et al. (2011) artificially lowers the derived age of the stellar population – and hence the total mass assembled – due to being luminosity-weighted to the age of the bright, recent starburst.

A program of observations with the IRAM Plateau de Bure Interferometer (PdBI) of ^{12}CO $J=4-3$ and $J=6-5$ emission carried out by Engel et al. (2010) in four of the SMGs mutually studied by Hainline et al. (2011) and Michalowski et al. (2010) have provided dynamical and gas mass estimates which appear to be consistent with the former set of stellar mass estimates but not the latter (under the condition that $M_\star + M_{\mathrm{gas}} \leq M_{\mathrm{dyn}}$). ^{12}CO-derived gas mass estimates can be very imprecise in galaxies where the ^{12}CO spectral line energy distribution (SLED) is not well sampled, however (Harris et al., 2010; Ivison et al., 2011; Bothwell et al., 2013; Ivison et al., 2012; Thomson et al., 2012). Furthermore, mid-J ^{12}CO observations are now recognised as providing a biased view of the extent of a galaxy's gas reservoir due to the excitation conditions of the lines, and

hence provide a potentially misleading picture of its dynamical state (Weiß et al., 2001; Walter et al., 2002). How these effects conspire to influence the conclusions reached in Engel et al. (2010) with regards to discriminating between stellar mass estimates in SMGs remains uncertain.

1.3.6 Gas masses and internal dynamics

The availability of high-precision redshifts for SMGs obtained via multi-wavelength follow-up observations (e.g. Chapman et al., 2005) has facilitated the study of their molecular gas content – the fuel from which new stars are formed – via their carbon monoxide (^{12}CO) line emission. Detecting and mapping this emission provides insight into the structure and internal dynamics of galaxies and enables estimates of the gas mass to be made (via the ^{12}CO-luminosity-to-molecular-gas-mass conversion factor, $\alpha_{\rm CO}$; e.g. Richardson, 1985; Young & Scoville, 1991), and hence act as a diagnostic to the state and availability of fuel for future star formation. In conjunction with estimates of SFR from $L_{\rm IR}$, ^{12}CO observations may also provide constraints on the gas-consumption timescale ($\tau_{\rm gas} \equiv M_{\rm gas}/{\rm SFR}$), enabling the likely evolutionary descendants of SMGs to be determined. Observations of the ^{12}CO molecule, which emits radiation at multiples of $\sim 115\,{\rm GHz}$ as its angular momentum quantum number changes from the $J^{th} \rightarrow J-1^{th}$ energy level are often employed as proxies for the H_2 molecule which comprises the bulk of the molecular gas content of galaxies but which itself is only rarely seen in absorption, and never in emission (§1.4).

The process of determining gas masses via ^{12}CO in distant SMGs has traditionally been a rather convoluted one (e.g. Greve et al., 2005), wherein (i) submillimetre sources are detected in blank-field surveys (e.g. Smail et al., 1997), (ii) the far infrared/radio correlation is used to determine robust radio counterparts (Ivison et al., 2002) with a high degree of positional accuracy, (iii) spectroscopic redshifts are obtained in deep optical follow-up observations as per Chapman et al. (2003, 2005), and then (iv) searches for ^{12}CO emission are conducted with narrow-band receivers tuned appropriately for the derived redshift. If the ^{12}CO line emission observed is not of the $J\!=\!1\!-\!0$ transition, then (v) an assumed brightness temperature conversion factor is used to convert the observed ^{12}CO $J \rightarrow J-1$ luminosity to an inferred ^{12}CO $J=1-0$ brightness, before finally (vi) the $\alpha_{\rm CO}$ luminosity-to-gas-mass conversion factor (Downes &

Solomon, 1998) is used to derive the total molecular gas mass.

Following early efforts to observe mid-J ($J \geq 3$) ^{12}CO lines in individual, strongly-lensed SMGs (e.g. Frayer et al., 1998; Genzel et al., 2003; Neri et al., 2003), the first attempt to conduct a mid-J ^{12}CO survey among radio-detected SMGs (Greve et al., 2005) with the PdBI yielded a median ^{12}CO line luminosity of $\langle L'_{\rm CO} \rangle = (3.8 \pm 2.0) \times 10^{10}\,{\rm K\,km\,s^{-1}}$ for the 18 sources, and a median line full width at zero intensity $\langle {\rm FWZI} \rangle = (780 \pm 320)\,{\rm km\,s^{-1}}$. Converting this ^{12}CO luminosity to an H_2 gas mass via the typical "star-forming galaxy" $\alpha_{\rm CO} \sim 0.8\,{\rm M_\odot\,(K\,km\,s^{-1}\,pc^2)^{-1}}$ this mean luminosity corresponds to $\langle M_{\rm gas} \rangle = (3.0 \pm 1.6) \times 10^{10}\,{\rm M_\odot}$. Given pre-existing estimates of the SFR based on $L_{\rm IR}$, a median gas consumption timescale $\tau_{\rm gas} \sim 40\,{\rm Myr}$ is implied.

The primary reason why early extragalactic ^{12}CO surveys focused on mid-J lines is that these lines are typically brighter than ^{12}CO $J = 1-0$ for gas at a given temperature T_k above the excitation requirements of the transition (e.g. $E_{\rm u}/k_{\rm B} \sim 33\,{\rm K}$, $n_{\rm crit} \sim 10^4\,{\rm cm^{-3}}$ for ^{12}CO $J = 3-2$ Papadopoulos et al., 2012), yet these very same excitation requirements imply that such observations are sensitive only to regions of warmed, star-forming gas, and are blind to the presence of any extended, low-excitation gas component (Bothwell et al., 2013). Indeed, observations of mid-J ^{12}CO lines in M 82 would expose only the highly-excited, $\sim 400\,{\rm pc}$ star-forming core of the molecular gas reservoir (Weiß et al., 2001), and not the more extended ($\sim 1.7\,{\rm kpc}$) cool gas component in which it is embedded (e.g. Walter et al., 2002). Reliance only on mid-J observations would hence yield a biased estimate of the total molecular gas mass in M 82 as well as an inaccurate representation of the dynamical field of the galaxy. In order to detect the *bulk* of the molecular gas reservoir *and* trace its spatial extent (which is an important component of dynamical mass estimates), observations of ^{12}CO $J = 1$–0, the lowest rung on the ^{12}CO ladder are necessary. ^{12}CO $J = 1-0$ is notoriously difficult to detect in high-z galaxies due to the faintness of the line ($\sim 1/9^{th}$ as bright as ^{12}CO $J = 3$–2 for the same kinetic temperature), and difficult to spatially resolve due to its low frequency, necessitating long, interferometric baselines and large collecting areas. Nevertheless, recent unresolved single-dish (Harris et al., 2010, 2012) and resolved, interferometric (Ivison et al., 2011; Riechers et al., 2011a,b; Thomson et al., 2012) studies of SMGs conducted with new or recently upgraded instruments and facilities have jointly served to underline the importance of ^{12}CO

$J = 1-0$ observations, uncovering brightness temperature ratios $r_{(3-2)/(1-0)} < 1$ and velocity line width ratios $\sigma_{(1-0)/(3-2)} > 1$, implying $\sim 2\times$ higher gas masses and greater spatial extents (and thus higher dynamical masses) in SMGs than had previously been assumed on the basis of mid-J-only studies.

1.3.7 Number counts and clustering

Following the detection of the first SMGs, numerous submillimetre surveys were initiated which aimed to characterise the role played by SMGs in the cosmic star formation history, and constrain galaxy evolution models. Among the key objectives of any such survey is that of determining the number of sources found as a function of flux. Early, flux-limited submillimetre surveys, covering both blank-fields (Hughes et al., 1998; Barger et al., 1998) and massive gravitational cluster lenses (Smail et al., 1997) – where both sensitivity and resolution are boosted by the lensing potential of the foreground cluster – were hindered by small number statistics, yet all pointed toward a surface density of $S_{850\mu\mathrm{m}} > 5\,\mathrm{mJy}$ galaxies of several $100\,\mathrm{deg}^{-2}$, with the majority lying at $z > 2$. For the observed redshift distribution of the Chapman et al. (2005), the sky density of SMGs suggests a co-moving volume density comparable to that of giant local ellipticals (Blain et al., 2003). By comparison, the luminosity function of similarly IR-bright IRAS galaxies at low redshift, if extrapolated out to SMG redshifts without evolution, would predict number counts $\sim 0.25\,\mathrm{deg}^{-2}$ (Blain et al., 2002, and references therein). Given the relatively flat selection function of SMGs between $z = 1$–8 caused by negative K-correction (Fig. 1.2), the obvious interpretation of these results is that the co-moving volume density of intensely star-forming, IR-bright, optically-obscured galaxies was much higher at $z \sim 2$ than it is today, an evolution $\propto (1+z)^4$ (Smail et al., 1997; Blain et al., 1999). The preponderance of bright, star-forming SMGs at high redshift and their match in co-moving volume density with present day elliptical galaxies makes them strong candidates for being the progenitors of local massive cluster galaxies (Wardlow, 2010).

1.3.8 SMGs and the "main sequence" of star-forming galaxies

Given the observed SFRs, stellar masses and gas masses of SMGs, various interpretations have been developed which argue that they are fundamentally different from "normal" star-forming galaxies. This dichotomy is variously expressed in terms of SMGs: (i) being divergent from the "main sequence", a tight, empirical relation between the specific star formation rates (sSFR=SFR/$M_\star$) and redshifts of star-forming galaxies (Daddi et al., 2007; Rodighiero et al., 2010, 2011); (ii) having anomalous dust properties, making them outliers on the $L_{\rm IR}^{\rm tot}/L_{8\,\mu{\rm m}}$ diagnostic plot (Elbaz et al., 2011); and (iii) as followers of a star-formation law distinct from that of "normal" galaxies (Daddi et al., 2007; Genzel et al., 2010).

Evolution in (s)SFR with z in star-forming galaxies

The SFRs and sSFRs of typical star-forming galaxies are seen to rise in a tight relationship by more than an order of magnitude from the present day out to $z \sim 2$, where sSFR reaches a plateau of $\sim 2 \pm 2\,{\rm Gyr}^{-1}$ (Daddi et al., 2007; Rodighiero et al., 2010). The low level of scatter in this relationship has led to its use as defining a "main sequence" for star-forming galaxies. This elevation in the typical sSFR of star-forming galaxies at more remote epochs has been associated with higher molecular gas fractions at high redshift (which may be the legacy of a prolonged period of cold mode accretion from the surrounding intra-galactic medium; sometimes referred to in the literature as "secular" evolution; Dekel et al., 2009; Carilli et al., 2010), while it also correlates with the increase in merger rates out to $z \sim 2$ predicted by ΛCDM cosmology, suggesting that a significant fraction of star forming galaxies may be merger-driven (Carilli & Walter, 2013).

At all redshifts, some galaxies are seen to lie above the main sequence; in a recent study, Rodighiero et al. (2011) looked at ~ 700 *Herschel*–PACS detected and $\sim 19,500$ BzK-selected galaxies, labelling those galaxies elevated 0.6 dex ($4\times$ or 2.5σ) above the main sequence "starburst galaxies". So-defined, starburst galaxies appear to contribute only $\sim 10\%$ of the cosmic star formation rate density, although the mapping of galaxies identified via this criterion to more physically-motivated sample boundaries is unclear; within this terminology, 80%

of SFR$> 100\,\mathrm{M}_\odot\,\mathrm{yr}^{-1}$ galaxies and 50% of SFR$> 1000\,\mathrm{M}_\odot\,\mathrm{yr}^{-1}$ galaxies (including therefore the majority of SMGs) are "main sequence" provided they have high enough stellar masses to begin with, regardless of the instantaneous processes behind responsible for their observed L_{IR}, while the evolving nature of the main sequence with look-back time allows for the possibility that even the analogue of an archetypal starburst like M 82 would be viewed as "main sequence" if observed at $z = 2$.

The $L_{\mathrm{IR}}^{\mathrm{tot}}/L_{8\,\mu\mathrm{m}}$ diagnostic

Another method for selecting samples of unusual infrared galaxies is presented by Elbaz et al. (2011), who, utilising 100–500-μm measurements across the GOODS-N and GOODS-S fields with *Herschel*, observe a Gaussian distribution in the IR8 parameter (IR8 $\equiv L_{\mathrm{IR}}/L_{8\,\mu\mathrm{m}}$) in star-forming galaxies, centred on IR8 $= 4 \pm 1.6$. A tail in the distribution encompassing $\sim 20\%$ of the sample extends to higher IR8 values. This high-IR8 tail is seen to correlate well with the outlying population in SFR–$M_\star$ space of Rodighiero et al. (2010). In addition to the correlation with SFR–$M_\star$ outliers, the high-IR8 tail appear to exhibit systematically "peakier" infrared SEDs implying dust temperatures up to $\sim 9\,\mathrm{K}$ higher than in the "main sequence", and also a dearth of vibrational polycyclic aromatic hydrocarbon (PAH) emission line features relative to the bulk of the population. While *strong* PAH emission features are typically assumed to be a tracer of intense star-formation and *weak* PAH emission a tracer of the harder radiation fields associated with AGN (Genzel et al., 1998; Peeters et al., 2004), the interpretation of Elbaz et al. (2011) is that IR8 serves both as a sSFR indicator and as an infrared luminosity surface density indicator (it correlates with $\Sigma_{\mathrm{IR}} \equiv L_{\mathrm{IR}}/2\pi r_{\mathrm{IR}}^2$) – galaxies with high IR8 are deemed *more* likely to have high Σ_{IR} and thus host prodigious, compact star formation events (high Σ_{SFR}).

Different star formation laws for disks and starbursts

An important constituent of any attempt to understand galaxy evolution is the relationship between SFR and the availability of molecular gas – often understood in terms of a prescriptive "star formation law". The most commonly-referenced star formation law is that of Schmidt (1959), which relates the gas surface density to the SFR surface density: $\Sigma_{\mathrm{SFR}} \propto \Sigma_{\mathrm{gas}}^N$, where a single line of slope $N = 1.4 \pm 0.2$

provides a good empirical fit for normal star-forming galaxies over six orders of magnitude in $\Sigma_{\rm SFR}$ (Kennicutt, 1998).

Early observations of molecular gas in ULIRGs and SMGs have indicated the existence of a parallel sequence – and hence a different star-formation law – in merger galaxies, displaced vertically from the "normal sequence" by $\sim 0.9\,$dex (Daddi et al., 2007; Genzel et al., 2010). Since "merger" galaxies appear to produce systematically more far-infrared luminosity per unit gas luminosity, and since these two properties are believed to trace SFR and $M_{\rm gas}$ respectively, merger-driven star formation is thus claimed to produce a systematically higher $\Sigma_{\rm SFR}/\Sigma_{\rm gas}$. Caution is necessary in interpreting these results, however, because determination both of the "gas luminosity", and conversion of that number to a physical gas mass are non-trivial problems. "Gas luminosity" is typically understood to mean $L'_{\rm CO(1-0)}$, yet until recently, direct ^{12}CO $J=1$–0 detections at high-z were rare and mid-J ^{12}CO lines were observed instead, which are subject to uncertain brightness temperature conversion factors. In addition, the choice of $\alpha_{\rm CO}$ used to convert $L'_{\rm CO(1-0)}$ to $M_{\rm gas}$ has the potential to greatly affect the distribution of galaxies on the $\Sigma_{\rm SFR}/\Sigma_{\rm gas}$ Schmidt-Kennicutt (SK) plot. Typically a bi-modal $\alpha_{\rm CO}$ is assumed, with the Galactic $\alpha_{\rm CO} = 5\,{\rm M}_\odot\,({\rm K\,km\,s^{-1}\,pc^2})^{-1}$ being deemed appropriate for "normal" star-forming galaxies and Milky Way giant molecular clouds (Solomon & Barrett, 1991), and $\alpha_{\rm CO} = 0.8$ for "merger" galaxies, including ULIRGs and SMGs (Downes & Solomon, 1998; Tacconi et al., 2008).

As a number of recent papers have shown (e.g. Harris et al., 2010; Ivison et al., 2011; Bothwell et al., 2013; Ivison et al., 2012), ^{12}CO $J=1-0$ luminosities in SMGs are typically seen to be $\sim 2\times$ higher than those which would have been inferred on the basis of mid-J observations only, which has the instant effect of moving SMGs systematically to the right on the Schmidt-Kennicutt (S–K) diagram, and back towards the high-mass end of the main sequence.

In addition, the use of a bi-modal $\alpha_{\rm CO}$ in calculating $M_{\rm gas}$ has the obvious potential to create a bi-modal population in $\Sigma_{\rm SFR}$ v $\Sigma_{\rm gas}$ space, re-emphasising the importance of determining its value correctly for each galaxy in question before interpreting the distribution of galaxies on the S–K plot. Downes & Solomon (1998) were the first to suggest that $\alpha_{\rm CO}$ in energetically merging galaxies might differ from the value taken for Galactic giant molecular clouds (GMCs), deriving

$\alpha_{\rm CO} = 0.8\,{\rm M}_{\odot}\,({\rm K\,km\,s^{-1}\,pc^2})^{-1}$ for ULIRGs on the basis of radiative transfer models through sub-thermally-excited ^{12}CO in molecular disks. The models were constrained by ^{12}CO $J = 1-0$ and $J = 2-1$ observations in Arp 220, Arp 193 and Mrk 273, and the resulting $\alpha_{\rm CO}$ has been used since Tacconi et al. (2008) for SMGs. Yet, while $\alpha_{\rm CO} = 0.8\,{\rm M}_{\odot}\,({\rm K\,km\,s^{-1}\,pc^2})^{-1}$ appears to be an appropriate statistical value for local ULIRGs (Downes & Solomon, 1998), determining $\alpha_{\rm CO}$ *in general* remains a problem which depends intricately on the dynamical field of the galaxy, and the gas densities and background temperatures (§1.4; Richardson, 1985; Glover & Mac Low, 2011; Narayanan et al., 2011, 2012; Papadopoulos et al., 2012). $\alpha_{\rm CO}$ likely varies from galaxy to galaxy, even if it is certainly lower on average in merging starburst galaxies than in quiescent disk galaxies. It remains an open question, therefore, how much the variation in $\alpha_{\rm CO}$ and the updated estimates of $L'_{\rm CO(1-0)}$ in starburst/merging galaxies have the potential to "wash away" some of the observed bi-modality of the S–K plot.

1.3.9 Disks or mergers? The morphologies of SMGs

In spite of the decade-and-a-half of effort that has gone into studying SMGs and attempting to determine the origin of their bolometric output, there remains a lack of agreement as to some of their basic morphological properties. The once paradigmatic view of SMGs as a population of major-merger events (e.g. Swinbank et al., 2006, 2008; Ivison et al., 2002; Tacconi et al., 2006, 2008) has recently been called into question by a number of papers which claim that SMGs are merely the high-mass end of the "normal" disk-like, star-forming galaxy population (e.g. Carilli et al., 2010; Dunlop, 2011; Michalowski et al., 2012; Targett et al., 2013). Because of the ubiquity of SMGs at $z \sim 2$ and the high star-formation rates involved, the resolution of this debate is likely to have ramifications for our understanding of galaxy evolution; the Baugh et al. (2005) ΛCDM model requires both a preponderance of major-mergers and a top-heavy IMF to reproduce the observed 850-μm number counts, while other groups (e.g. Davé et al., 2010) identify and simulate SMGs as massive galaxies at the centres of large potential wells, whose star-formation is powered by a combination of smooth accretion and the consumption of multiple gas-rich satellites (minor mergers).

Evidence that some SMGs are major-mergers

High-resolution spectroscopic and kinematic results form the basis for the interpretation of SMGs as major merger events. In particular, ^{12}CO emission line maps and data cubes have informed much of our understanding of the internal dynamics of SMGs (e.g. Frayer et al., 1999; Neri et al., 2003; Greve et al., 2005; Tacconi et al., 2008; Ivison et al., 2011), yet acquisition of high-fidelity ^{12}CO data prior to the availability of a full complement of ALMA antennas is a very time-consuming process, with a circuitous route of observations typically being necessary to establish both the position and frequency of any likely ^{12}CO emission, and then $\sim$ 10s of hours of on-source integration time with PdBI or the VLA required to map the ^{12}CO lines themselves. As such, sample sizes for which this work has been undertaken are necessarily small. Integral field unit (IFU) spectroscopy of the ionised gas component (Swinbank et al., 2005, 2006; Banerji et al., 2011; Alaghband-Zadeh et al., 2012) provides an alternative means of probing the spatially resolved dynamics of SMGs in a manner that is less demanding in terms of telescope time, but carries with it potential biases due to excitation and the uncertain dust extinction which plagues short wavelength measurements of dusty sources.

Common among such studies are the ubiquity of multiple spatial components with velocity offsets, and disturbed morphologies featuring broad – often double-peaked – emission line profiles whose FWHM$=$ 500–1000km s^{-1} . Clear velocity gradients (from position-velocity – PV – diagrams) on scales of up to $\sim$ 10 kpc are often seen. Together, these may indicate mergers in differing stages of completion. Alaghband-Zadeh et al. (2012) use the ratio of the maximum velocity across a source to its average velocity dispersion, $V_{obs}/2\sigma$ as an indicator of the degree to which the source's kinematics are dispersion/rotation dominated, which they compare with the observed Hα half-light radii, $r_{1/2}$. They find no correlation between the two quantities for their sample of nine SMGs, in contrast to the strong correlation noted by Förster Schreiber et al. (2009) for UV/optically-selected star-forming galaxies in the same redshift range. The systematically higher $\langle V_{obs}/2\sigma \rangle$ of SMGs compared to that of more quiescent star-forming galaxies at the same redshift highlights a dichotomy in the kinematics between the two populations.

Evidence that some SMGs are star-forming disks

An alternative interpretation of SMG data has recently emerged, in which SMGs simply represent the high-mass end of the normal star-forming galaxy population at $z = 2$–3 (e.g Davé et al., 2010; Targett et al., 2011; Dunlop, 2011). From the stellar mass estimates of Michalowski et al. (2010), the sSFR of SMGs is "as expected" for galaxies occupying the massive end of the main sequence of Daddi et al. (2007), while the rest-frame optical morphological studies of Targett et al. (2011) and Targett et al. (2013) indicate that the optical light of $\sim 95\%$ of SMGs is well described by a clumpy exponential disk profile, with Sersic indices $n \sim 1.1$ and half-light radii $r_{1/2} \sim 3.1\,\mathrm{kpc}$. Swinbank et al. (2010a), in a similar morphological analysis of SMGs do note, however, the SMGs differ more in their UV vs. optical appearances than do normal disk-like galaxies, and interpret this as evidence of structured dust obscuration, which has the potential to hinder the precision of rest-frame UV/optical morphological studies in these systems.

In an interferometric ^{12}CO $J = 2-1$, $J = 1-0$ and $J = 6-5$ study of the remarkable $z = 4.05$ SMG GN 20, Carilli et al. (2010) and Hodge et al. (2012) find compelling evidence of cold mode accretion fuelling star formation in a massive clumpy disk $\sim 14\,\mathrm{kpc}$ in extent. In 120 hours with the upgraded VLA, Hodge et al. (2012) detect a colossal gas reservoir of $M_{\mathrm{gas}} = 1.3 \pm 0.4 \times 10^{11} \times (\alpha_{\mathrm{CO}}/0.8)\,\mathrm{M}_{\odot}$ (their choice of the standard ULIRG α_{CO} as opposed to the value normally associated with disk-like galaxies is justified via dynamical analysis), whose velocity field is well-modelled by a rotating disk with a flat rotation curve and $i \sim 30°$.

A complex, heterogeneous group

There are still clearly fundamental disagreements over the "specialness" of SMGs, relating to whether they have systematically elevated sSFR for their redshift and/or a different star formation law (governing SFR per unit gas mass), concerning the shape of their infrared dust SEDs (as probed via the IR8 diagnostic), and indeed concerning their basic morphology. Each of these disagreements has potentially crucial consequences in informing our choice of cosmological model (Baugh et al., 2005; Davé et al., 2010), and the question duly begged is how much of this disagreement is due to real variation in SMG properties, and how much of it arises out of the over-interpretation of results

obtained via uncertain conversion factors, incorrect translation of observed to physical properties, and/or simple systematic selection effects.

Blain et al. (2004), Farrah et al. (2006) and Kovács et al. (2010) observe that the typically large beam sizes (> 15 arcsec) of submillimetre telescopes have the potential to "sum up" the flux of multiple distinct but apparently nearby galaxies – none of which would qualify as an SMG individually – and smear it into one "detection". If such "detections" are present in large numbers in SMG catalogues and are used as the priors in searches for counterparts at other wavelengths, then the runaway boot-strapping of subsequent mis-identifications may have the potential to seriously undermine our understanding of SMGs.

In addition to concerns over potential mis-identifications, Hayward et al. (2011), in a review of the submillimetre galaxy selection criterion, remind us that 850-μm selection does not straightforwardly select the brightest/most intensely star-forming galaxies at a particular redshift, but is explicitly biased toward the discovery of galaxies with *cold* dust temperatures by virtue of the shape of the Rayleigh-Jeans tail. As such, $S_{850\,\mu\mathrm{m}}$ is not expected to linearly correlate with SFR. Indeed, on the basis of their 3D dust radiative transfer calculations on hydrodynamic simulations of isolated and merging disk galaxies, Hayward et al. (2011) find that $S_{850\,\mu\mathrm{m}} \propto \mathrm{SFR}^{0.4}$ in quiescent disk galaxies, and $S_{850\,\mu\mathrm{m}} \propto \mathrm{SFR}^{0.1}$ in mergers, where the sharp decrease in dust mass and compact geometry raise T_{dust} and hence suppress $S_{850\,\mu\mathrm{m}}$ even as the bolometric output of the galaxy increases in correspondence with the starburst. The implication of this result therefore is that a $\sim 16\times$ increase in SFR at the height of merger activity compared to the quiescent pre-merger average may be masked within a $\sim 2\times$ increase in $S_{850\,\mu\mathrm{m}}$ flux density. Taken into consideration along with the possibility of multiple sources blending into one 850-μm peak ("galaxy pair SMGs"), this argues that selection of SMGs on the basis of a simple $S_{850\,\mu\mathrm{m}}$ flux density cut is liable to produce a mixed bag of galaxy types whose contents can only be reliably disentangled via consistent application of a unified set of multi-wavelength identification criteria, or by the availability of large-scale, high-resolution submillimetre source catalogues as will soon be available with a full complement of ALMA antennas (e.g. Hodge et al., 2013; Karim et al., 2013).

1.4 Modelling the molecular interstellar medium

The interstellar medium (ISM) in galaxies typically accounts for only a few percent of the baryonic mass present (Omont, 2007), yet contains within it the material (gas) *from* which and also comprises the environment *in* which stars form, as well as the remnants left behind after their death in the form of metal-enriched, complex dust grains. As such, detailed study of the ISM is a necessary step in constructing accurate galaxy evolution models. Processes during the stellar life cycle, such as accretion, jets, stellar winds, supernovae and shocks can affect the composition and structure of the ISM, which in turn affects the initial conditions for subsequent star-formation events. The ISM within a galaxy may also appropriate new material, either by smooth, steady accretion from the intra-cluster medium (ICM), by merging with another galaxy of roughly equal mass (a *major merger*), or by wholesale devouring of a much smaller galaxy (a *minor merger*).

Molecular gas represents a significant and important constituent of the ISM, being found in the densest regions and representing the refined fuel from which stars ultimately form via gravitational collapse. By far the most abundant constituent of the molecular gas supply is H_2 – which is formed when single H atoms combine on the surface of dust grains, and is destroyed when exposed to strong UV radiation fields (Tielens, 2005) – yet despite occasionally being observable in *absorption* (if a sufficiently strong UV background is present), the bulk of this gas is rarely seen in *emission* due to the lack of a strong dipole moment in the H_2 molecule (e.g. Israel, 1997).

The systematic study of cold molecular gas in galaxies therefore in practice is carried out vicariously, through the study of tracer molecules which are assumed to be concomitant with the underlying H_2 reservoir, and to interact with it in fundamentally predictable ways. The most commonly-used tracer molecule is ^{12}CO, which is collisionally-excited by kinetic interactions with H_2 and photo-excited by the background radiation field, and whose rotational emission spectrum produces a series of lines $\sim J \times 115\,\mathrm{GHz}$ apart for increasing rotational quantum number J. While the mid-J ^{12}CO lines ($J \geq 3$) have moderate excitation requirements ($n_{\mathrm{crit}} \sim 10^4\,\mathrm{cm}^{-3}$, $E_u/k_{\mathrm{B}} \sim 33\,\mathrm{K}$; Papadopoulos et al., 2012), typical of actively star-forming regions, the lowest-rung on the ^{12}CO ladder, ^{12}CO $J = 1-0$ is excited at much lower densities and temperatures ($n_{\mathrm{crit}} \sim 10^2\,\mathrm{cm}^{-3}$,

$E_u/k_{\rm B} \sim 10\,{\rm K}$; Tielens, 2005), and is thus the best probe of the *bulk* of the gas reservoir.

Were the ^{12}CO rotational lines to be optically *thin*, and the molecular abundance ratio of H_2-to-^{12}CO known, then it would be trivial to measure $L'_{\rm CO(1-0)}$, the velocity-integrated ^{12}CO $J=1-0$ luminosity, and deduce the total gas mass by "counting the molecules" of ^{12}CO. In practice, the former condition is not true (^{12}CO becomes optically-thick at moderate column-densities), and the latter condition is unknowable without an independent estimate of the total H_2 mass – itself the very quantity we wish to derive. The problem of determining H_2 gas masses by strictly analytical means is therefore insoluble, yet reliable estimates *can* be made by *modelling* the molecular excitation and emission conditions within the ISM for a set of physically-plausible input parameters and favouring solutions which predict a ^{12}CO rotational spectrum which closely matches that observed in and throughout the galaxy.

The physics of the relationship between ^{12}CO and H_2 is encapsulated via the "X factor":

$$X_{\rm CO} = \frac{{\rm N}_{\rm H_2}}{W_{\rm CO}} \tag{1.25}$$

where $\rm N_{H_2}$ is the column density of molecular hydrogen, and $W_{\rm CO}$ is the corresponding velocity-integrated ^{12}CO $J = 1-0$ line intensity (in $\rm K\,km\,s^{-1}$). Typically, observers express the conversion factor instead in terms of the total molecular gas mass $M_{\rm gas}$ and velocity-integrated ^{12}CO luminosity, $L'_{\rm CO(1-0)}$:

$$\alpha_{\rm CO} = \frac{{\rm M}_{\rm gas}}{L'_{\rm CO(1-0)}} \tag{1.26}$$

$X_{\rm CO}$ and $\alpha_{\rm CO}$ are related (Narayanan et al., 2012) via

$$\alpha_{\rm CO}(\,{\rm M_\odot}\,({\rm K\,km\,s^{-1}\,pc^2})^{-1}) = (1.59\times10^{-20}) \times X_{\rm CO}({\rm cm^{-2}}\,({\rm K\,km\,s^{-1}})^{-1}) \tag{1.27}$$

In the following, I present an outline of the principles of radiative transfer and excitation in the ISM, and discuss the large velocity gradient (LVG) approximation, by which the ISM of kinematically active galaxies may be studied.

1.4.1 Radiative transfer

The fundamental motivation behind constructing models of the molecular ISM in galaxies is to explain telescope observables (line intensities, line profiles, size) in terms of underlying physical conditions and processes (densities, abundance ratios, temperature/excitation, kinematics).

Emission line intensities are most commonly expressed at radio wavelengths in units of temperature. The *brightness temperature* of a spectral line is defined as the temperature at which a black body would have the same specific intensity I_ν as the observed line:

$$I_\nu(T) = \frac{2h\nu^3}{c^2}\frac{1}{e^{\frac{h\nu}{kT}}-1} \tag{1.28}$$

In the Rayleigh-Jeans limit, $e^{\frac{h\nu}{kT}} \sim 1 + h\nu/kT$, and so by substitution and rearrangement

$$T_B \equiv \frac{c^2}{2k\nu^2} I_\nu \tag{1.29}$$

Equation 1.29 may also be expressed in terms of the source properties $T_{\rm ex}$ (excitation temperature) and τ_ν (optical depth) by substituting for the source intensity as

$$T_B(\nu) = \frac{h\nu}{k}\left(\frac{1}{e^{\frac{h\nu}{kT_{\rm ex}}}-1}\right)\int_0^{\tau_{\rm total}} e^{-\tau_\nu} d\tau_\nu \tag{1.30}$$

In general, the source properties $T_{\rm ex}$ and τ_ν are not known *a priori*, and must be determined empirically, with respect to a particular cloud model. If the

observed spectral line is emitted by de-excitation from the j^{th} to the i^{th} energy levels, then $T_{\rm ex}$ is given as

$$\frac{n_j}{n_i} = \frac{N_j g_i}{N_i g_j} = e^{\frac{-h\nu}{kT_{\rm ex}}} \tag{1.31}$$

where N_i is the total population of the i^{th} level and g_i is that level's degeneracy, such that n_i is the relative population per degenerate sub-level and $\Sigma g_i n_i = 1$.

In the gigahertz regime in which molecular lines are emitted, the Rayleigh-Jeans approximation no longer holds, and thus Equation 1.29 does *not* correspond to a physical temperature in the medium, except under certain assumptions. Nevertheless, radio astronomers persist with the notation of brightness temperatures over specific intensity because of the advantages that: (i) it provides a means of specifying the brightness of a spectral line that is intimately related to the level populations of the emitting matter, and (ii) in thermal equilibrium it enables the radiative transfer equation to take on the particularly simple form

$$T_B(\tau_\nu) = T_B(0)e^{-\tau_\nu} + T_K(1 - e^{-\tau_\nu}) \tag{1.32}$$

for gas kinetic temperature T_K (Lequeux, 2005). If the optical depth is low and the background radiation field $T_B(0)$ is negligible, then the measured $T_B = \tau_\nu T_K$; if the optical depth is large and the material is in local thermal equilibrium (LTE) then $T_B = T_K$.

1.4.2 Modelling prescription

Having introduced the concepts of observable brightness temperatures (which act as a proxy for specific intensity) and excitation temperatures (which tell us about the excitation conditions of the molecular gas), the prescription for modelling the ISM is now as follows:

1. Specify the model free parameters, including the densities and molecular abundances of all relevant species relative to H_2 (e.g. $\alpha_{\rm CO}$), and kinematics.

2. Determine $T_{\rm ex}$ for all molecular transitions in the medium, as a function of position within the cloud.

3. Calculate Equation 1.30 to get a prediction for the radiation temperature T_B for each transition through each line of sight through the ISM.

4. Convolve the derived T_B with the (known) beam profile of the telescope in order to predict the observable quantity, T_B^*, which may be compared with observations.

In principle, steps 1, 3 and 4 are straightforward: step 2 is anything but, and requires further digression into the field of the radiative and collisional transitions that set the level populations which determine $T_{\rm ex}$.

1.4.3 The case of ^{12}CO emission

The energy of the J^{th} level of a purely rotational molecular transition in a linear molecule (such as ^{12}CO) is given (e.g Emerson, 1998) by

$$E_{J_\nu} = J(J+1)Bh - DJ^2(J+1)^2h \approx J(J+1)Bh \tag{1.33}$$

where B is the rotational constant of the molecule, D its centrifugal distortion constant and h is Planck's constant. D is typically very small compared to B, and in the *rigid rotor* approximation used in modelling, it is set to zero.

In order to calculate $T_{\rm ex}$ for a particular molecular rotational transition, Equation 1.31 tells us that it is necessary to consider the processes that contribute to populating and depopulating each energy level. Generally, both radiative processes (including absorption and both spontaneous and stimulated emission) and collisional processes play a role in establishing level populations, leading to the equilibrium condition

$$\frac{dn_j}{dt} = \frac{dn_{j_{\rm rad}}}{dt} + \frac{dn_{j_{\rm coll}}}{dt} = 0 \tag{1.34}$$

We now consider these two contributions separately.

Radiatively induced transitions

Dipole selection rules mean that for purely rotational transitions, only radiative transitions between adjacent levels ($\Delta j = \pm 1$) are allowed, and so the rate of change of the population of level j due to radiative processes depends solely on contributions coming from the levels below (i) and above (k)

$$\frac{dN_{j_{\rm rad}}}{dt} = -B_{jk}J_{\nu 2}N_j - B_{ji}J_{\nu 1}N_j + B_{kj}J_{\nu 2}N_k + B_{ij}J_{\nu 1}N_i - A_{ji}N_j + A_{kj}N_k \quad (1.35)$$

where terms including the Einstein coefficients A_{ji}, B_{ji} and B_{ij} relate respectively to spontaneous emission, stimulated emission and absorption, and $J_{\nu 1}$ and $J_{\nu 2}$ are the mean intensities of the radiation field due to transitions from the levels $k \rightarrow j$ and $j \rightarrow i$ respectively, with central frequencies ν_1 and ν_2. The Einstein coefficients are defined relative to the upward/downward transition rates R_{ij} and R_{ji} and to the radiation intensity J_ν as

$$R_{ij} = 4\pi B_{ij} J_\nu \quad (1.36)$$

$$R_{ji} = A_{ji} + 4\pi B_{ji} J_\nu \quad (1.37)$$

as in Emerson (1998). Relationships between the Einstein coefficients can be established by considering two-level case of Equation 1.35.

$$B_{ij}J_\nu N_i - B_{ji}J_\nu N_j = A_{ji}N_j \quad (1.38)$$

Rearranging for J_ν and invoking the Boltzmann relation (1.31) we may define the *source function* S_ν

$$S_\nu = \frac{A_{ji}N_j}{B_{ij}N_i - B_{ji}N_j} = \frac{A_{ji}}{\frac{n_i g_i}{n_j g_j}B_{ij} - B_{ji}} = \frac{(A_{ji}/B_{ji})}{(g_i B_{ij}/g_j B_{ji})exp\left(\frac{h\nu}{kT}\right) - 1} \quad (1.39)$$

In order for the latter-most expression to equal B_ν (as it must in LTE) for all T, we have that

$$\Rightarrow A_{ji} = \frac{2h\nu_{ji}^3}{c^2} B_{ji} \tag{1.40}$$

and

$$g_i B_{ij} = g_j B_{ji} \tag{1.41}$$

from which we may re-write Equation 1.35 in terms of the *relative* occupations ($\mathrm{n}_i = \mathrm{N}_i/\mathrm{g}_i$) of the three energy levels as

$$\frac{dn_{j_{\mathrm{rad}}}}{dt} = \frac{g_k}{g_j} A_{kj} \left(n_k + \frac{c^2}{2h\nu_2^3} J_{\nu 2} n_k - \frac{c^2}{2h\nu_2^3} J_{\nu 2} n_j \right) - A_{ji} \left(n_j + \frac{c^2}{2h\nu_1^3} J_{\nu 1} n_j - \frac{c^2}{2h\nu_1^3} J_{\nu 1} n_i \right) \tag{1.42}$$

Collisional transitions

Rotational transitions may also occur due to collisions with other molecules. Unlike radiative transitions, which in the case of a rigid linear dipole can only occur between adjacent energy levels, collisional transitions can occur between any pair of energy levels, depending on the amount of translational kinetic energy that is transferred during the collision. In general, the rate of change of the occupation of level j due to collisional processes is the sum of contributions due to transitions that take place between level j and those below it (L), and those that take place between j and higher levels (U)

$$\frac{dN_{j_{\mathrm{coll}}}}{dt} = \sum_{L=0}^{j-1} \left(N_L C_{Lj} - N_j C_{jL} \right) + \sum_{U=j+1}^{\infty} \left(N_U C_{Uj} - N_j C_{jU} \right) \tag{1.43}$$

where C_{Lj} etc are the collision rates which may be expressed as $C_{Lj} = R_{Lj}n(H_2)$ $= n(H_2)\langle\sigma_{Lj}v\rangle$, a rate constant multiplied by the number density of molecular hydrogen atoms. Hydrogen vastly outnumbers all other molecular species in the ISM and is hence, to all intents and purposes, the sole agent of collisional excitation in ^{12}CO.

In equilibrium the collision rates upwards and downwards between any pair of energy levels i and j may be related via the principle of *detailed balance* as

$$n_i C_{ij} = n_j C_{ji} \tag{1.44}$$

which from Equation 1.31 gives us

$$C_{ij} = C_{ji}\frac{g_j}{g_i}exp\left(\frac{-h\nu}{kT_{\rm K}}\right) \tag{1.45}$$

where $T_{\rm K}$ is the kinetic temperature of the gas. We thus need only compute either the upward *or* downward collision rates (or alternatively either one of R_{ij} or R_{ji} if we know or can reasonably assume the density $n(H_2)$) in order to compute the other.

Combining Equations 1.33 and 1.43, and again invoking $n_i = N_i/g_i$, we have

$$\begin{aligned}\frac{dn_{j_{\rm coll}}}{dt} = &\sum_{L=0}^{j-1}\left(\frac{C_{jL}}{g_L}g_L\right)\left\{n_L exp\left(\frac{-hB}{kT_{\rm K}}(j(j+1)-L(L+1))\right)-n_j\right\}\\ &+\sum_{U=j+1}^{\infty}\left(\frac{C_{Uj}}{g_j}g_U\right)\left\{n_U - n_j exp\left(\frac{-hB}{kT_{\rm K}}(U(U+1)-j(j+1))\right)\right\}\end{aligned} \tag{1.46}$$

Optical depth and opacity

The optical depth gives a measure of the transparency through a medium at a particularly frequency ν, and is defined as

$$\tau_\nu \equiv \int_{r_1}^{r_2}\kappa_\nu dr \tag{1.47}$$

where κ_ν is the *absorption coefficient*, such that $1/\kappa_\nu$ is the photon mean free path through the medium, so making τ_ν the number of mean free paths between r_1 and r_2 (Peraiah, 2001).

For purely monochromatic radiation arising due to a transition between two energy levels i and j, the absorption coefficient may be written in terms of the Einstein coefficients

$$\begin{aligned} \kappa_\nu &\equiv \frac{h\nu}{4\pi}\Big(N_i B_{ij} - N_j B_{ji}\Big) \\ &= \frac{c^2}{8\pi\nu^2} N_i A_{ij} \frac{g_j}{g_i}\left[1 - exp\left(\frac{-h\nu}{kT_{\rm ex}}\right)\right] \end{aligned} \tag{1.48}$$

where in the final step we have replaced B_{ij} and B_{ji} with the Einstein coefficient A_{ji}, and substituted in Equation 1.31 to have the absorption coefficient expressed in terms of the excitation temperature.

Real spectral lines of course are not purely monochromatic, but extend over a finite range of frequency. We account for this by introducing the concept of the normalised spectral distribution $\phi_{ji}(\nu)$, which defines the line of sight Doppler velocity profile of molecules at a particular point in the cloud

$$\int_{\rm line} \phi_{ji}(\nu) d\nu = 1 \tag{1.49}$$

and redefine κ_ν for our representative line by multiplying by $\phi_{ji}(\nu)$.

$$\kappa_\nu \equiv \frac{c^2}{8\pi\nu^2} N_i A_{ij} \frac{g_j}{g_i}\left[1 - exp\left(\frac{-h\nu}{kT_{\rm ex}}\right)\right]\phi_{ji}(\nu) \tag{1.50}$$

Towards a synthesis of radiative transfer and excitation

Having discussed the role played by radiative transfer and collisions between molecules in populating the relevant energy levels, we now drive the discussion back towards the observables that our models are designed to explain. From

Equation 1.30, we see that the brightness $T_B(\nu)$ of a spectral line originating from a transition between the j^{th} and i^{th} energy levels depends on $T_{\rm ex}$ and τ_ν. We have derived the functional form of τ_ν above; $T_{\rm ex}$ is related to the occupancies (n_i, n_j) of these levels via Equation 1.31, and n_i and n_j are determined by the balance between radiative and collisional transitions.

Combining Equations 1.34, 1.42 and 1.46, we have (in LTE) that

$$\begin{aligned}\frac{dn_j}{dt} = \frac{g_k}{g_j}A_{kj}\left(n_k + \frac{c^2}{2h\nu_2^3}J_{\nu 2}n_k - \frac{c^2}{2h\nu_2^3}J_{\nu 2}n_j\right) - A_{ji}\left(n_j + \frac{c^2}{2h\nu_1^3}J_{\nu 1}n_j - \frac{c^2}{2h\nu_1^3}J_{\nu 1}n_i\right) \\ + \sum_{L=0}^{j-1}\left(\frac{C_{jL}}{g_L}g_L\right)\left\{n_L exp\left(\frac{-hB}{kT_{\rm K}}(j(j+1) - L(L+1))\right) - n_j\right\} \\ + \sum_{U=j+1}^{\infty}\left(\frac{C_{Uj}}{g_j}g_U\right)\left\{n_U - n_j exp\left(\frac{-hB}{kT_{\rm K}}(U(U+1) - j(j+1))\right)\right\}\end{aligned} \tag{1.51}$$

where the first two terms are those arising due to radiative transitions and the latter two are those arising due to collisional processes.

It ought to now be evident that attempts to model the state of the molecular gas in galaxies in general is difficult to the point of being intractable. A surfeit of free parameters exists (density, kinetic temperature, and in the case of extragalactic sources, the number of discrete clouds per telescope beam), whose prior specification is likely to alter the emergent T_B that the model is designed to predict. Of particular concern is the dependence of $dn_{\rm coll}/dt$ on n(H_2), the molecular hydrogen density, which is encoded within the collision rate coefficients C_{Lj} and C_{Uj}; n(H_2) is typically the very thing we ultimately wish to determine by observing ^{12}CO emission in the first place! In practice, plausibility arguments can *a priori* rule out excessively high or low values of n(H_2), while observations of multiple ^{12}CO molecular lines (e.g. $J=1-0$, $J=3-2$, $J=4-3$, etc.) in the same gas cloud, each with their own T_B, can help to constrain τ_ν and narrow the parameter space within which the model can reproduce the data.

Of more fundamental concern is the presence of J_ν, the mean radiation intensity at frequency ν in Equation 1.42. This introduces a degree of circularity to the problem, whereby J_ν exerts influence on the level populations yet also is dependent *on* the level populations, due to the fact that molecular

transitions in the gas produce photons with exactly the right range of frequencies to interact with nearby molecules of the same species. We are thus faced with the uncomfortable conclusion that regions within the cloud can become radiatively coupled, which requires an iterative approach to solving the equations of statistical equilibrium, and introduces even more free parameters since *global* as well as *local* properties of the molecular gas complex can play a role in determining level populations.

Fortunately, observational evidence provides justification for the use of a few simplifying assumptions, which make the task of solving the equations of statistical equilibrium a more tractable problem. In the following subsections, we will explore two of the most commonly used simplifications and discuss their underlying assumptions.

1.4.4 Comparison with ^{13}CO emission

Within the Solar neighbourhood, the isotopologue ^{13}CO is $\sim 90\times$ less abundant than ^{12}CO. As such, it has an optical depth $\tau_{13} \sim \tau_{12}/90$, and is hence very probably optically thin on galactic scales (Combes et al., 2006). The similarity in the corresponding energy levels between ^{12}CO and ^{13}CO[1] means that they ought to be populated similarly between the two molecular species, and hence share a common $T_{\rm ex}$ (thermalisation). As such, we may re-write Equation 1.30 to obtain a relationship between $T_{R,^{13}\rm CO}$ and $T_{R,^{12}\rm CO}$, which in the Rayleigh-Jeans limit is

$$\frac{T_{R,^{13}\rm CO}}{T_{R,^{12}\rm CO}} = \frac{1-\exp(-\tau_{13})}{1-\exp(-I_{12/13}\tau_{13})} \tag{1.52}$$

where $I_{12/13}$ is the abundance ratio $[^{12}\rm CO]/[^{13}\rm CO]$. Hence for an assumed abundance ratio, observations of ^{13}CO provide a prediction for $T_{R,^{12}\rm CO}$, which can be used to measure the ^{12}CO optical depth of the system.

1.4.5 The Large Velocity Gradient (LVG) approximation

The thermal line-width of a static, homogeneous cloud of ^{12}CO at 30 K is $\sim 0.13\,\mathrm{km\,s^{-1}}$. This is approximately two orders of magnitude lower than the line-

[1] http://www.nist.gov/pml/data/molspec.cfm

widths observed in Galactic giant molecular clouds (e.g. Hopkins, 2012), and four orders of magnitude lower than that seen in the most violently merging galaxies (e.g. Greve et al., 2005), where spectral lines are Doppler-broadened by the kinematics of the system. If this Doppler broadening occurs due to large-scale gravitational collapse of molecular clouds (Goldreich & Kwan, 1974) as opposed to localised supersonic *micro-turbulence*, then local velocity element, dv, within the line profile traces a distinct region of size $l \approx dvR/\Delta V$, where ΔV is the total velocity width of the line and R is the depth of the medium along the line of sight.

Then the radiation field at a point r in the cloud is related to the source function S_ν and the *escape probability* $\beta(r)$, which expresses the likelihood of a photon reaching a distance r from its point of origin.

$$J_\nu(r) = [1 - \beta(r)]S_\nu(r) \tag{1.53}$$

For the large velocity gradient case outlined above, we expect that $\beta \ll 1$ for small r and $\beta \to 1$ for increasing distances from the point of origin.

For a homogeneously and isotropically collapsing cloud, de Jong et al. (1980) derive β in terms of the mean optical depth τ_0 as

$$\beta = \frac{1 - exp(-\tau_0)}{\tau_0} \tag{1.54}$$

In the LVG regime, we approximate the line profile ϕ_ν within an infinitesimal volume as a top hat function of width $d\nu$ and height $1/d\nu$, where

$$d\nu = \frac{\nu}{c}\frac{dv}{dr}dr \tag{1.55}$$

and dv/dr is the local velocity gradient, which we assume to be constant throughout the cloud. Then from Equation 1.50, the mean optical depth τ_ν becomes (e.g. Papadopoulos et al., 2012)

$$\tau_\nu = \kappa_\nu \frac{c}{\nu}\frac{dv}{dr} = \frac{c^3}{8\pi\nu^3}\frac{g_j}{g_i}\frac{N_i A_{ji}}{(dv/dr)}\left[1 - exp\left(\frac{-h\nu}{kT_{\rm ex}}\right)\right] \tag{1.56}$$

In the case of ^{12}CO which is collisionally excited via interactions with H_2, we may substitute $N_i = [\mathrm{CO/H_2}]\times \mathrm{n(H_2)}$ and obtain

$$\tau_\nu = \frac{c^3 A_{ji}}{8\pi\nu^3}\frac{g_j}{g_i}\left[1 - exp\left(\frac{-h\nu}{kT_{\rm ex}}\right)\right]\left[\frac{\mathrm{CO}}{\mathrm{H_2}}\right]\frac{\mathrm{n(H_2)}}{(dv/dr)} \tag{1.57}$$

.

Thus for a given set of multi-J ^{12}CO observations, each transition with its own observed $T_{\rm B}$, it is possible to generate models, and iterate over the remaining free parameters ([CO/H_2], n(H_2), $T_{\rm k}$), choosing the set which best fits the available spectral line data (e.g. Richardson, 1985; Sharon et al., 2013).

1.5 Aims and outline of the thesis

In the remainder of this thesis, I will present the results of a survey of the molecular gas content of a sample of four gravitationally lensed SMGs, in which I combine 120 hours of new VLA observations of spatially-resolved ^{12}CO $J = 1-0$ emission with infrared, submillimetre, radio and mid-J ^{12}CO results from the literature. In so doing, I aim to be able to characterise the state of the molecular gas reservoir in a representative sample of actively star-forming galaxies at $z \sim 2.5$, in order to determine: (i) $M_{\rm gas}$, and so determine how much fuel they have left to form stars, assign an upper limit to the duration of the present starburst, and determine whether a unique "merger" star formation law is observationally justified; (ii) the global and spatially-resolved excitation of the gas in the ISM, thus determining whether the star formation activity is localised or spread throughout the galaxy; and (iii) the relative importance of star formation and hidden AGN as mechanisms powering the prodigious $L_{\rm IR}$ of these sources.

The thesis is structured as follows; in Chapter 2, I review the technical capabilities of the upgraded VLA, and present a guide for the reduction of

spectral line data in the $\mathcal{AIPS}$ software package. In Chapter 3, I present the results of a study in to the molecular gas of three gravitationally lensed, yet still intrinsically bright SCUBA-selected SMGs, in which I determine gas masses via the use of certain physically-motivated assumptions, and use estimates of $\mathrm{SFR_{IR}}$ and $\mathrm{SFR_{radio}}$ to constrain the AGN bolometric contribution to L_{IR}. In Chapter 4, I perform a similar analysis for SMM J21352–0102 ("The Cosmic Eyelash"); strong gravitational lensing (32.5×) makes a remarkable object out of this otherwise typical SMG, in which high-resolution submillimetre and radio continuum and ^{12}CO maps allow the interplay between dust, star formation and gas to be studied in unprecedented detail for an object at $z \sim 2.5$. Finally, in Chapter 5, I aim to summarise my conclusions, and evaluate them within the context of the wider issues of galaxy evolution.

Chapter 2

Data reduction

2.1 Interferometry and the EVLA project

The angular resolution of a telescope $\theta_{\rm min} \sim \lambda/D$ is a measure of the smallest angular separation at which two point sources can be resolved as separate objects with a primary reflector of diameter D, operating at observing wavelength λ. In the visible region of the electromagnetic spectrum ($\lambda \sim 500\,{\rm nm}$), the 2.4-m primary mirror of the Hubble Space Telescope (*HST*) produces images with resolution of a few tens of milliarcseconds (mas), enabling detail to be resolved on $\sim 100\,{\rm pc}$ scales even in relatively distant galaxies ($z > 2$). To achieve comparable resolution at metre or even centimetre radio wavelengths would require telescope reflectors several tens of kilometres in diameter. Clearly the building of such structures is ruled out on grounds of cost and engineering practicality. Instead, radio astronomers have developed techniques by which the signals from multiple smaller telescopes, separated by a distance D can be coherently combined to produce images with the resolution that would have been achieved by a single dish of diameter D (albeit with sensitivity that is diminished by the smaller collecting area of the multiple small telescopes). This is the technique of *interferometry*. The process by which multiple signals from multiple pairs of antennas ("baselines") are combined to produce an image is called *aperture synthesis*.

In the following, I present a brief outline of the fundamentals of aperture synthesis, in order to set the subsequent discussion on data reduction with the NRAO Karl G. Jansky VLA in its proper context. For a fuller analysis of aperture

synthesis, see the textbooks by Wilson et al. (2009), Thompson et al. (2008) and the lectures that comprise the Sixth NRAO Synthesis Imaging Summer School (Taylor et al., 1999).

2.1.1 An introduction to synthesis imaging

The electric field

A radio antenna is a device which measures the electric field $E_\nu(\mathbf{r})$ at some point $\mathbf{r}$ coming from an astrophysical source at $\mathbf{R}$. We may treat the electric field as a scalar phenomenon (in which we may ignore polarisation properties) without loss of generality. If the source is very far away, and the space between us and it empty, then the electric field recorded from the source at point $\mathbf{r}$ is given as

$$E_\nu(\mathbf{r}) = \int \varepsilon_\nu(\mathbf{R}) \frac{e^{2\pi i\nu|\mathbf{R}-\mathbf{r}|/c}}{|\mathbf{R}-\mathbf{r}|} dS \tag{2.1}$$

where dS is an element of surface area on the celestial sphere, an imaginary sphere of radius $\mathbf{R}$, centred on the antenna, and $\varepsilon_\nu(\mathbf{R})$ is the distribution of the electric field on this celestial sphere.

Coherence

Signals from two radio telescopes may be combined electronically by a *correlator*, a device which computes the expectation of the product of the electric field at antenna one (at $\mathbf{r}_1$) and the complex conjugate of the field at antenna two (at $\mathbf{r}_2$)

$$V_\nu(\mathbf{r_1}, \mathbf{r_2}) = \langle E_\nu(\mathbf{r_1}) E_\nu^*(\mathbf{r_2}) \rangle = \left\langle \int\int \varepsilon_\nu(\mathbf{R_1}) \varepsilon_\nu(\mathbf{R_2}) \frac{e^{2\pi i\nu|\mathbf{R_1}-\mathbf{r_1}|/c}}{|\mathbf{R_1}-\mathbf{r_1}|} \frac{e^{2\pi i\nu|\mathbf{R_2}-\mathbf{r_2}|/c}}{|\mathbf{R_2}-\mathbf{r_2}|} dS_1 dS_2 \right\rangle \tag{2.2}$$

If we consider the field *not* to be spatially coherent – that is to say, $\langle \varepsilon_\nu(\mathbf{R_1}) \varepsilon_\nu^*(\mathbf{R_2}) \rangle = 0$ for $\mathbf{R_1} \neq \mathbf{R_2}$ – then we may write the correlation as the product

$$V_\nu(\mathbf{r_1}, \mathbf{r_2}) = \int \left\langle |\varepsilon_\nu(\mathbf{R})|^2 \right\rangle |\mathbf{R}|^2 \frac{e^{2\pi i\nu|\mathbf{R}-\mathbf{r_1}|/c}}{|\mathbf{R}-\mathbf{r_1}|} \frac{e^{2\pi i\nu|\mathbf{R}-\mathbf{r_2}|/c}}{|\mathbf{R}-\mathbf{r_2}|} dS \tag{2.3}$$

Then if $\mathbf{s}$ is the unit vector in the direction of the source ($\mathbf{s} \equiv \mathbf{R}/|\mathbf{R}|$), $I_\nu(\mathbf{s})$ is the observed intensity as a function of position ($I_\nu(\mathbf{s}) = |\mathbf{R}|^2 \left\langle |\varepsilon_\nu(\mathbf{s})|^2 \right\rangle$), the celestial sphere is again assumed to be far away ($|\mathbf{r}/\mathbf{R}| \equiv 0$) and the surface element dS is replaced by $|\mathbf{R}|^2 d\Omega$, we may express Equation 2.3 as

$$V_\nu(\mathbf{r_1}, \mathbf{r_2}) \equiv \int I_\nu(\mathbf{s}) e^{-2\pi i\nu \mathbf{s}.(\mathbf{r_1}-\mathbf{r_2})/c} d\Omega \tag{2.4}$$

This function – called the *spatial coherence function* of the field – depends only on the vector separation between our two antennas, *not* on their absolute positions. The *raison d'être* of an interferometer is to measure this spatial coherence function, from which the intensity of an astrophysical source as a function of position – *i.e.* an image – may be recovered by Fourier transform, under certain assumptions.

The uv coordinate system and sampling effects

The first useful assumption which allows us to recover I_ν from a set of measurements of $V_\nu(\mathbf{r_1}, \mathbf{r_2})$ is that the emission of interest comes from a small region of the celestial sphere. Then if the unit vector $\mathbf{s}_0$ points towards some reference position on the celestial sphere (e.g. the centroid of source/field), then any other position on source may be described by the unit vector $\mathbf{s} = \mathbf{s}_0 + \sigma$, where σ is a small position vector on the surface of the celestial sphere, perpendicular to $\mathbf{s}$.

If we then choose a coordinate system in which $\mathbf{s}_0 = (0, 0, 1)$, we may re-write Equation 2.4 as

$$V_\nu(u, v, w) = V_\nu^{'}(u, v, w) e^{2\pi iw} = \int\int I_\nu(l, m) e^{-2\pi i(ul+vm)} dl dm \tag{2.5}$$

where (u, v, w) are the components of $\mathbf{r}_1$ - $\mathbf{r}_2$, and (l, m, n) are the source plane coordinates (see Figure 2.1).

$V_\nu(u, v, w)$ is the coherence function relative to the reference vector $\mathbf{s}_0$, known as the *phase tracking centre*. Were the interferometer to consist of an infinite number of antennas/baselines, each with uniform sensitivity as a function of direction, then the intensity distribution as a function of (l, m) would be obtained by simple Fourier inversion of Equation 2.5.

In practice, however, the coherence function $V_\nu(u, v, w)$ is not known at all locations at once, but is sampled by antennas at discrete locations in the uv plane. We therefore introduce the sampling function $S(u, v)$, and define the *dirty image* as

$$I_\nu^D(l, m) = \int\int V_\nu(u, v) S(u, v) e^{2\pi i(ul+vm)} du dv = I_\nu * B \tag{2.6}$$

That is to say, the image produced by integrating the set of visibilities over all available baselines is the convolution of the "true" source intensity distribution I_ν and $B(l, m)$, where $B(l, m)$ is the synthesised (dirty) beam of the array

$$B(l, m) = \int\int S(u, v) e^{2\pi i(ul+vm)} du dv \tag{2.7}$$

The synthesised beam defines the resolution of an interferometric array, and is a function of the distribution of baseline lengths in the array, their orientations with respect to the celestial sphere, and the relative weightings applied between them (e.g. Briggs, 1995). While long baselines are necessary to achieve good angular resolution, the dynamic range of interferometric images depends on the uniformity of coverage of the uv plane.

As the Earth rotates during a long observing track, so the orientation of the array changes with respect to the source, filling in the uv plane. Additionally, many modern interferometers consist of antennas which may be moved on a semi-regular basis, such that repeated observations of the same object at different hour angles, in different array configurations sample the uv plane relatively well. Nevertheless, the effect of discrete sampling in the uv plane is that the operation

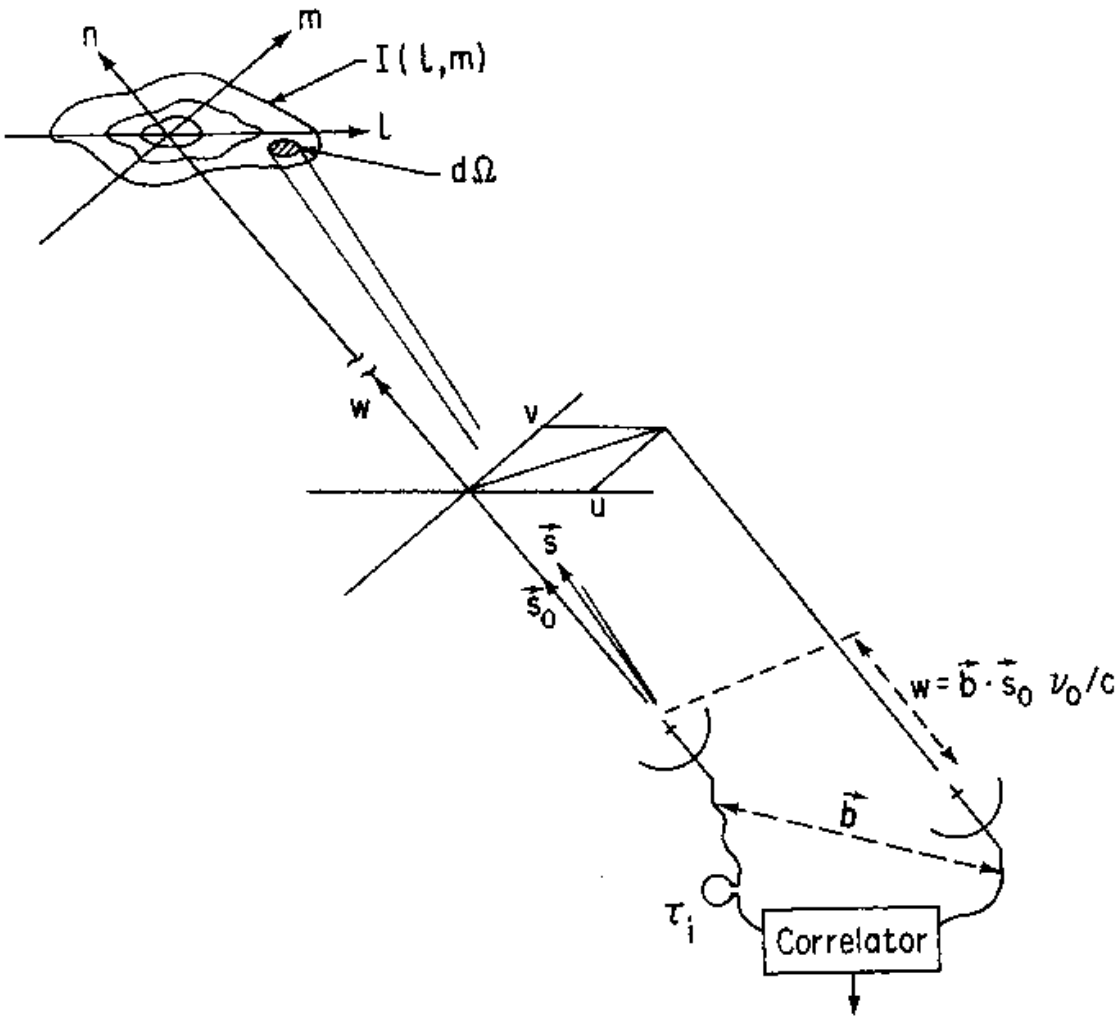

Figure 2.1: Schematic representation of the (u, v, w) and (l, m, n) coordinate systems used to express the interferometer baselines and the source brightness distribution, respectively. Reproduced from Thompson (1999).

of de-convolving I_ν and B (Equation 2.6) produces many degenerate solutions. From this *menagerie* of possible images, it is impossible to pick the "best" without introducing some physically-motivated assumptions and constraints.

The two most commonly used algorithms used in radio astronomy for solving Equation 2.6 for I_ν are CLEAN and the "maximum entropy method" (MEM). Briefly, the CLEAN algorithm represents the astrophysical source as a set of delta functions in an otherwise emission-less region of sky, and iteratively convolves these so-called "clean components" with the dirty beam and subtracts them from the dirty image (I_ν^D) until there remains no peak in the dirty image above a user-specified level. Then the accumulated list of clean components is convolved with the *clean beam* (a Gaussian best fit to the central lobe of the dirty beam) to produce a *clean image*. The fidelity of a CLEANed image can be improved via the introduction of plausible constraints. Of particular importance is the ability to introduce constraints on the source size and position via the use CLEAN boxes. The CLEAN algorithm will thence only search for clean components within the region of the map specified by the CLEAN boxes, thus mitigating the likelihood of a spurious noise peak or interferometer sidelobe being "cleaned" and finding its way in to the final clean image, where its presence would be mistaken for real source structure.

The maximum entropy method instead seeks to fit images to the data (within the noise levels) and then selects the image with maximal entropy, with respect to some *a priori* "default image" (e.g. a low resolution image of the same object). For a full discussion of the merits of each, see Cornwell et al. (1999). Throughout this work, I consistently use the Cotton-Schwab variant of CLEAN (Schwab, 1984), and provide details of the $\mathcal{AIPS}$ inputs used to create the finished data products in the relevant science chapters (Chapters 3 & 4).

2.1.2 The Karl G. Jansky Very Large Array

The Karl. G. Jansky Very Large Array (VLA) is a radio interferometer located near the town of Magdalena, some 50 miles West of Socorro, New Mexico, USA. It is run by the National Radio Astronomy Observatory (NRAO[1]), and for thirty years has been an extraordinarily productive scientific instrument, delivering unprecedented insights into astrophysical phenomena as diverse as planetary

[1] http://www.nrao.edu

nebulae (e.g. Condon & Kaplan, 1998), masers (e.g Sjouwerman & Pihlström, 2008), radio galaxies (e.g. Perley et al., 1984), and was even used to receive telemetry from the Voyager 2 spacecraft on its journey past Neptune (Stone & Miner, 1989).

Originally dedicated in 1980, the VLA is a multiple element interferometer, observing in several bands between 74 MHz – 50 GHz, and consisting of 27 × 25-m dishes, placed on pads next to a"Y" shaped railway track. The antennas are cyclically shifted along the tracks in four major configurations – A, B, C and D, in order of increasing compactness, such that the longest baseline in A-configuration is 27 km (cf. 1 km in D-configuration). The VLA also has three intermediate configurations – BnA, CnB, DnC – which have two arms in the more compact configuration and the Northern arm in the more extended configuration, to provide good *uv* coverage of Southern sources. In 2001, the National Science Foundation approved a complete overhaul of the array's receivers, correlator and data transmission systems using the latest technology, to create the Expanded Very Large Array. EVLA Early Science Programs began with the new array in 2010 March, and by 2013 January, the hardware upgrades were complete. Among the quantifiable improvements these upgrades have brought are: complete spectral coverage from 1–50 GHz (including the provision of Ka-band receivers, to observe in the hitherto inaccessible 26–40 GHz window); a factor 10× increase in continuum sensitivity; a 1024× increase in the number of spectral channels available, and; up to 8 GHz of instantaneous bandwidth per polarisation (Perley et al., 2011).

In 2012 March, the telescope was re-named the Karl G. Jansky Very Large Array, in honour of the telecommunications engineer whose serendipitous discovery of radio waves coming from the centre of the Milky Way heralded the start of radio astronomy[2].

2.2 Calibration and flagging of VLA spectral line data in $\mathcal{AIPS}$

Interferometer data require calibration prior to imaging, to correct the *observed* visibilities $\tilde{V_{ij}}$ for the distortions they experience – relative to the "true" visibilities

[2]http://www.nrao.edu/pr/2012/jansky/

Figure 2.2: The Karl G. Jansky Very Large Array in DnC configuration, 2010 June 13^{th}, during the NRAO Twelfth Synthesis Imaging Workshop. *Photo credit: Michel Schammel.*

V_{ij} – due to atmospheric and instrumental effects.

At any given time t, the observed and true visibilities are related through

$$\tilde{V_{ij}}(t) = \mathcal{G}_{ij}(t)V_{ij}(t) + \epsilon_{ij}(t) + \eta_{ij}(t) \tag{2.8}$$

where $\mathcal{G}_{ij}(t)$ is the *complex gain* of the baseline made by antenna pair ij, $\epsilon_{ij}(t)$ is the *complex offset* and $\eta_{ij}(t)$ is the stochastic complex noise. In modern interferometers with stable electronics, $\epsilon_{ij}(t) \approx 0$, while the effect of $\eta_{ij}(t)$ can be negated through appropriate time-averaging of the observed visibilities (Fomalont & Perley, 1999). The task of calibration thus reduces to that of computing both the amplitude and phase of the complex gains $\mathcal{G}_{ij}(t)$ as a function of time for each baseline in the array.

In general, $\mathcal{G}_{ij}(t)$ can be split in to the product of a complex gain $g_i(t)$ for each antenna, which in turn may be split in to antenna-based amplitude ($a_i(t)$) and phase ($\phi_i(t)$) based corrections

$$\mathcal{G}_{ij}(t) = g_i(t)g_j^{\star}(t)g_{ij}(t) = a_i(t)a_j(t)e^{i(\phi_i(t)-\phi_j(t)}g_{ij}(t) \tag{2.9}$$

$g_{ij}(t)$ is termed the *closure error*, and is the residual part of the baseline-based complex gain which cannot be factored out. This operation enables

calibration to be performed separately on amplitude and on phase on an antenna-by-antenna basis (providing $g_{ij}(t)$ is small), which is often considered preferable to performing baseline-based solutions for two important reasons: (i) corruptions of the true visibilities V_{ij} most often occur on a "per antenna" basis, whether due to receiver malfunctions or to atmospheric conditions particular to the location of each antenna, and (ii) because the number of independent baselines for an interferometer with N dishes is $N(N-1)/2$, antenna based solutions are more computationally efficient, and increasingly so for larger N.

In practice, amplitude and phase errors are calibrated out of interferometer data by frequently nodding the telescope dishes between standard calibrator sources – ideally, isolated, bright, unresolved sources of known flux density and spectral index – and the science target(s), computing the calibration solutions needed to make each scan of the calibrator match a model of the calibrator source visibilities, and then interpolating those solutions between calibrator scans to alter the visibilities of the science observations.

In some situations, such "ordinary" calibration is impractical; the refractive properties of the atmosphere vary with position and time, and the lack of a sufficiently strong, point-source calibrator in the vicinity of the science source can mandate the exploration of more inventive calibration strategies. One such strategy is that of *self-calibration*, in which the complex antenna gains are considered free parameters, and via the insertion of some plausible assumptions about the structure of the source, observations of a source may be used to calibrate themselves. The aim of self-calibration is to produce a model image $\hat{I}$, the Fourier transform of which (Equation 2.4) well matches the observed visibilities $\hat{V}_{ij}$ within the noise. The self-calibration algorithm of Schwab (1980) is that: (i) a "first guess" for the source model is made using the minimum of physically motivated constraints on the source structure; (ii) the observed visibilities are converted to those of a point source through division by these model visibilities; (iii) the complex gains are solved for; (iv) the corrected visibilities are deduced; (v) an updated model is created from the new visibilities; (vi) the process is repeated until the "best fit" model visibilities and the observed visibilities converge. Self-calibration unfortunately leads to the loss of information on the strength of the source to which the method is applied, but in many cases this loss may be recovered to an acceptable degree by "bootstrapping" the flux scale to that of a

set of (relatively infrequent) observations of a bright calibration source of known absolute flux density.

In addition to providing a route to calibration in situations where calibration would otherwise be impossible, self calibration can be used in conjunction with ordinary calibration to improve the efficiency of an observing run. The fact that self calibration allows a model image to be iteratively improved via successive applications of the procedure means that solutions of a given fidelity can be achieved with fewer scans of the calibrator source compared to simple interpolation of solutions, thus increasing the amount of time that the telescope can spend on the science source.

Having introduced the concepts underpinning synthesis imaging with radio interferometers, and having summarised the key capabilities of the upgraded VLA, I now present the details of how the ^{12}CO $J = 1-0$ observations used throughout the following science chapters were scheduled, edited and calibrated. Discussion specific to the imaging of each source in $\mathcal{AIPS}$ is deferred until the appropriate science chapter (Chapters 3 & 4).

2.2.1 ^{12}CO $J=1-0$ data editing and calibration

The formalism of data calibration expressed in Equation 2.8, which allows one to recover the "true" visibilities from a set of imperfect "observed" visibilities is only applicable when both $\epsilon_{ij}(t)$ and $\eta_{ij}(t)$ are small. In modern interferometers, this is generally true for most visibilities on most baselines, but the presence of heavily degraded visibilities – due to poor weather, receiver or correlator hardware malfunctions, poor dish pointing, imprecisely determined baseline coordinates, etc – can render this assumption invalid. If sufficiently degraded data are included in the calibration procedure, they can lead to the wrong complex gain term $\mathcal{G}_{ij}(t)$ being computed for all other baselines, and thus have a drastic negative effect on the fidelity of the final data product (image, spectrum or data cube). Editing of degraded visibilities is thus an essential first step in the process of calibrating interferometer data, and in the reduction of the redshifted ^{12}CO $J=$ 1–0 data presented in Chapters 3 and 4, an iterative approach of editing the most obviously poor quality data, calibrating, checking the fidelity of the data product and removing any remaining poor data before calibrating again was adopted.

Ka-band ^{12}CO $J = 1-0$ observations were made at various stages during

the Expanded Very Large Array upgrade project, during which the number of antennas with functioning Ka-band receivers increased from ~ 10 to the final 27. The data were retrieved from the NRAO science archive in multi-source *uv* FITS files, which were imported using the $\mathcal{AIPS}$ task FITLD, following which NX tables were created to hold an index of the *uv* data with INDXR. Prior to initial editing of the data, updated positions for each antenna were entered via the $\mathcal{AIPS}$ task VLANT, and the flux density of the primary calibrator was set using SETJY.

Following these two standard pre-calibration steps, the calibrator data were visually inspected using the $\mathcal{AIPS}$ task TVFLG. Data which are corrupt due to known mis-pointings of the antennas, or due to hardware errors (of which the telescope operators are aware) are typically auto-flagged while the observations are in progress, but often these and many more subtle errors remain unflagged by the online algorithms, and require careful inspection and editing by the user. By default, visibilities are presented in TVFLG in time-order along the vertical axis, with the horizontal axis grouping together baselines which share a common antenna. The quantity of interest (e.g. amplitude or phase) is then represented for each visibility by the brightness of the greyscale. Plotting amplitudes in TVFLG (Figure 2.3), it is often clear that certain baselines with a common antenna are systematically "darker" than the rest, reflecting probable hardware malfunctions. These data are most easily removed by "flagging by antenna". Plotting the amplitude vector difference (AMPVDIFF) reveals another common problem with VLA data – corrupt visibilities in the first integration of each scan. These data may be removed either by using the "flag a time" option in TVFLG, or by using the specially-written $\mathcal{AIPS}$ routine QUACK. Inspection of the calibrator sources in each track, in each polarisation, in each IF, in each channel in TVFLG in each of amplitude, phase, amp v diff, phase v diff, amplitude difference and phase difference reveal additional corrupt visibilities which may be flagged by antenna, by scan, or individually using the "clip interactive" option as necessary.

Flagged calibrator data are then corrected for issues arising from the poorly-recorded group delays and phases at the VLA[3] using the specially-written $\mathcal{AIPS}$ task FRING, which fits delay solutions to ~ 1 min of data towards the end of a good scan of the primary flux calibrator, and mitigates the periodic, linear phase slope/wrapping that would otherwise present itself in the data. Interferometer

[3] $\mathcal{AIPS}$ cookbook appendix E

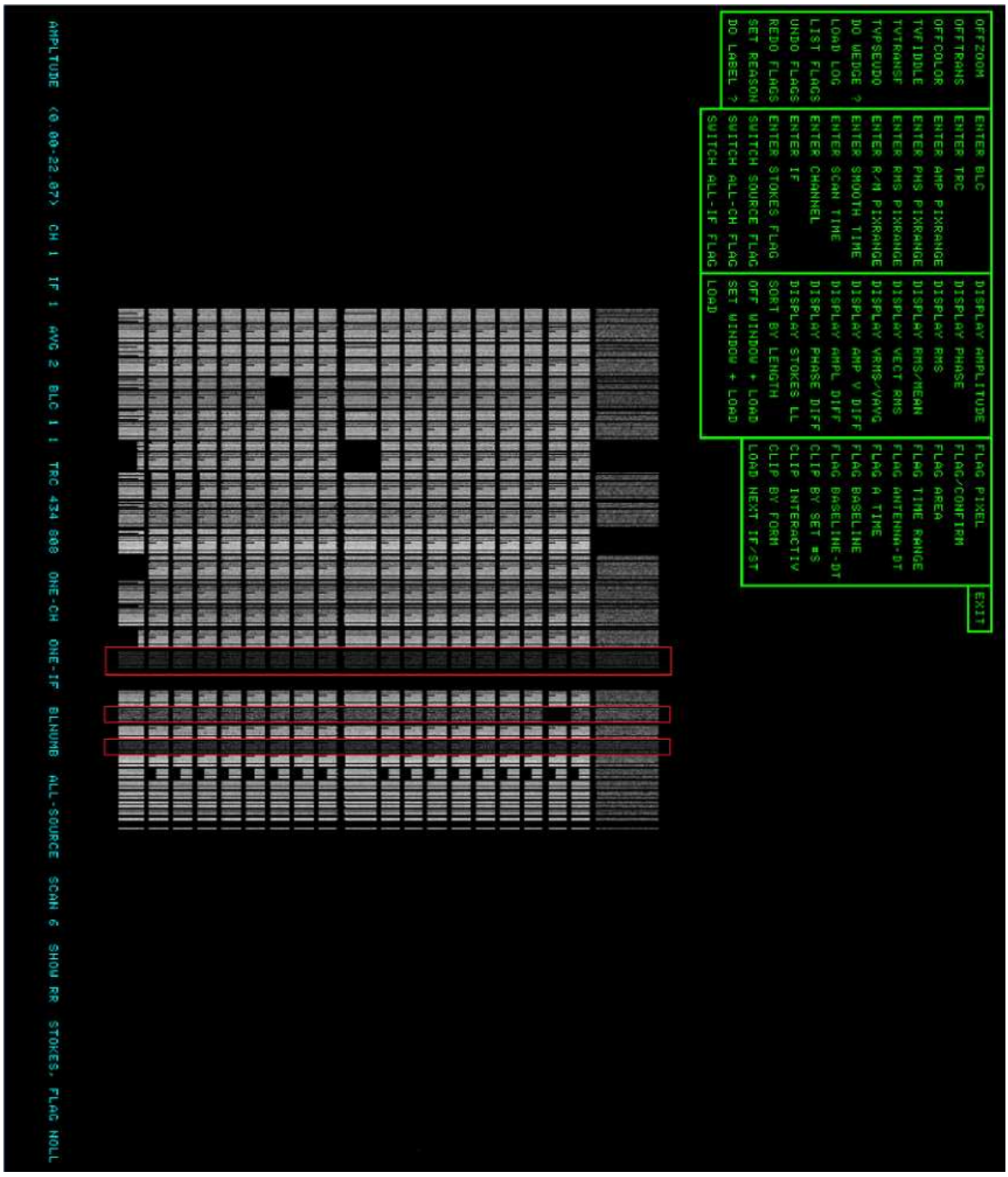

Figure 2.3: Typical TVFLG screen of visibility amplitudes for a track of VLA Ka-band data. All 64x2 MHz channels (at the time the data were recorded) in each IF are averaged and displayed, and the data are grouped in the x-axis by baseline (each x-axis pixel corresponds to one unique baseline, e.g. 1&2, 1&3... 1&27, 2&3... 2&27...) and each y-axis pixel corresponds to a single 1 s correlator integration interval. The greyscale represents the amplitude of each visibility. From these uncalibrated data, we can immediately pick out baselines with abnormally low amplitudes (here, all baselines featuring antennas 13, 16 & 18).

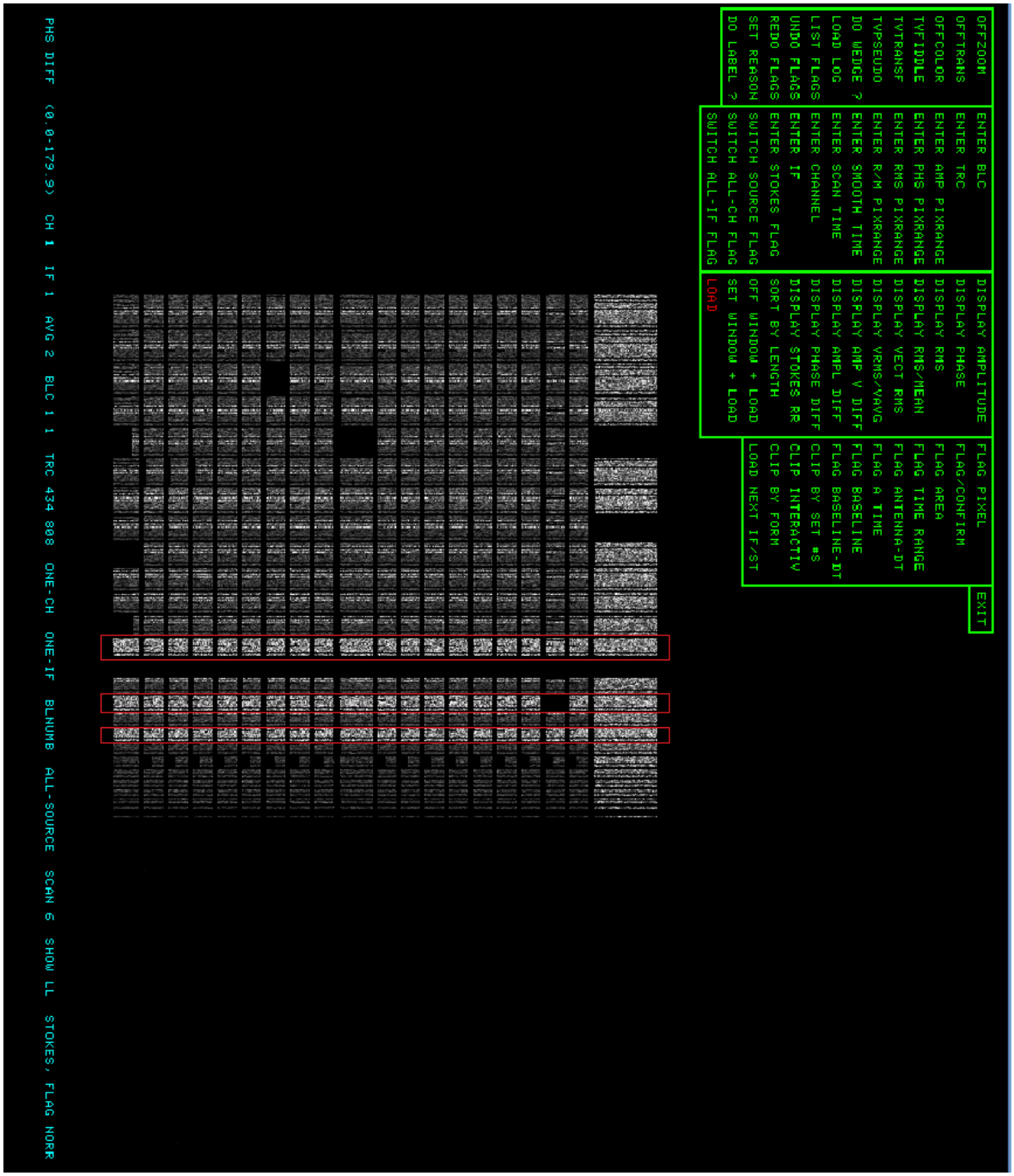

Figure 2.4: Typical TVFLG screen of visibility phase amplitudes for a track of VLA Ka-band data. As per Figure 2.3, data are gridded by baseline and by time. We see that the same three antennas which had anomalously low amplitudes (13, 16 & 18) also have anomalous phases. These visibilities are flagged, lest they contaminate the final data product.

phases are relative quantities, and may be determined only with respect to some fixed standard of reference. FRING – and all other calibration routines – therefore require that a suitable reference antenna be chosen, with respect to which all other antenna phases are computed. Choosing a suitable reference antenna is a non-trivial undertaking, with important ramifications for the subsequent calibration attempts. A suitable reference antenna is one which is present in a multitude of scans and is "well behaved" (i.e. records relatively consistent amplitudes and phases across all its baselines, even prior to calibration), and is relatively centrally located within the array in any given configuration. Solutions from FRING are stored in an SN table, and are applied to the data with CLCAL.

Following this initial calibration step, the next major step is to perform a bandpass calibration, to correct the observed visibilities for the frequency-dependent response of the antennas across their usable bandwidth. While the $\mathcal{AIPS}$ task BPASS contains a "self-cal" option within it to allow a bandpass table to be computed without the bandpass source having been previously calibrated ("divide by channel 0", turned on using the BPASSPRM(5)=0 flag), this method relies on the averaging of several channels, and actually involves both a subtraction of the average phase and a division by the average amplitude – the latter operation introducing a "Rician bias", wherein the "average" amplitude is systematically higher than the "true" amplitude. To circumvent this eventuality, I elected instead to perform a full, manual self-calibration of the bandpass calibrator source with CALIB, performing an initial calibration (solving for amplitude and phase simultaneously; SOLMODE='A&P') across a narrow range of channels in the centre of the bandwidth, and applying the correction with CLCAL prior to splitting the data for this source out from the multi-source file with SPLAT. The SPLAT'ted data were then self-calibrated using a point source model of arbitrary flux density 1 Jy located at the pointing centre (SMODEL = 1 *rest 0), before the bandpass (BP) table was computed from these self-calibrated data with the task BPASS, applying the calibration table determined from the self-calibration procedure (BPASSPRM(5)=1, to prevent the automatic "division by channel 0"). The resulting BP tables were inspected for suitability with POSSM, before being copied back to the corresponding multi-source file with TACOP.

The bandpass having been thus determined, the preliminary CL and SN tables used to facilitate the bandpass determination were deleted with EXTDEST, and

calibration of the data in earnest – using the appropriate BP table – began. The primary flux calibrator – in each case, a well-modelled, standard NRAO calibrator source – was calibrated for amplitude and phase using the appropriate K-band model image, and applying the BP table. Then, the secondary calibrator source was calibrated – again in amplitude and phase – and the antenna gain/phase solutions written to the *same* SN table, which was inspected for suitability with SNPLT. At this stage, the phase stability of each baseline could be determined, and antennas which frequently featured in baselines with a high degree of phase scatter were flagged, before the entire calibration process was un-done and repeated minus these bad antennas.

Following successful calibration, the absolute flux scaling of both sources was computed from the SN table using the $\mathcal{AIPS}$ task GETJY (the secondary calibrator flux being "bootstrapped" from the flux density of the primary calibrator already in the SU table). Finally, the calibration solutions stored in the SN table were written to a CL table with CLCAL, before the science target itself was visually inspected and edited in TVFLG, checking for amplitude, phase, amplitude vector difference and phase vector difference in each channel, in each polarisation and in each IF pair as before. After excision of sufficiently degraded visibilities, the final calibration (CL) was applied and the science data for each track split out from the multi-source files with SPLAT (during which the data were also time-averaged to 9 s/integration, to reduce the output file sizes) before all adjacent IFs were combined to create a single frequency spectrum with NOIFS.

The data weights were updated for each track with REWAY, before all tracks from each array configuration were concatenated with DBCON (REWEIGHT 0 0). The final multi-configuration *uv* FITS files for each science source were then created by quickly making dirty images from each array configuration separately, inspecting the "sum of gridded weights" in each image, and then using DBCON to concatenate the *uv* data from different array configurations with the REWEIGHT parameter set to provide the optimal 1:4 weighting ratio between adjacent array configurations, and so maximise the likelihood of the final data set producing a Gaussian synthesised beam when imaged (Frazer Owen, *private communication*).

A flowchart of the entire calibration process is presented in Figure 2.5.

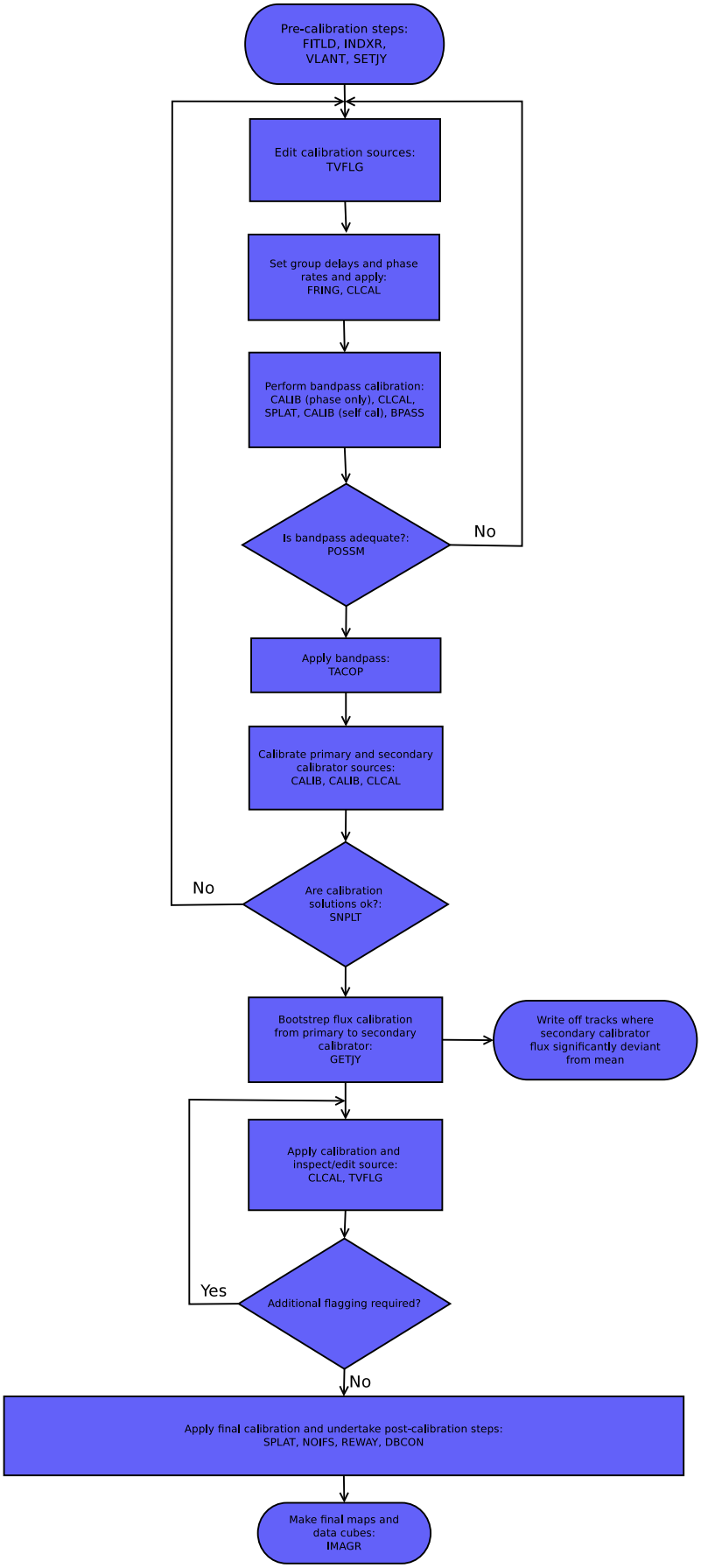

Figure 2.5: VLA ^{12}CO data reduction flowchart (see text for details)

Chapter 3

A trio of lensed submillimetre galaxies

3.1 Introduction

3.1.1 Lensed SMGs

Since the earliest detections of ^{12}CO in high-redshift galaxies (e.g. Brown & Vanden Bout, 1991; Solomon et al., 1992), much effort has been put into discerning the mass, extent and physical properties of the H_2 gas in galaxies across cosmic time; this offers a snapshot of their evolutionary state and narrows down the possibilities for their likely descendents. Until now, available technology has limited the study of ^{12}CO at high redshift to relatively bright, mid-J lines (^{12}CO $J = 3-2$ and above), which are shifted into broad, clean atmospheric windows such as that at 3 mm. The excitation requirements of these lines render such observations insensitive to any cool, extended gas component, of the type wherein much of the gas is routinely found (e.g. Papadopoulos & Seaquist, 1999; Weiß et al., 2005a; Bothwell et al., 2013). For local galaxies the intrinsically fainter $J = 1-0$ transition occupies the 3-mm atmospheric window and mid-J lines are more difficult to study, requiring high-frequency receivers and excellent atmospheric conditions. Efforts to conduct comparative studies at low and high redshift have therefore been few and far between, and the relationship between high-redshift galaxies and their myriad possible present-day descendants is not well understood.

I exploit the recent upgrades to the National Radio Astronomy Observatory's (NRAO's[1]) Karl G. Jansky Very Large Array (VLA), which includes the provision of Ka-band receivers (26.5–40 GHz), to study the redshifted ^{12}CO $J=1$–0 emission from three lensed SMGs: (i) SMM J14009+0252 lying at $z = 2.9344$ (Ivison et al., 2000; Weiß et al., 2009), lensed by Abell 1835 and one of the brightest SMGs detected in the SCUBA Cluster Lens Survey (SCLS; Smail et al., 2002); (ii) SMM J16359+6612, a bright SMG a $z = 2.5168$ (Kneib et al., 2004, 2005) and lensed into three images by the Abell 2218 cluster; and (iii) SMM J02399–0136 at $z = 2.808$ (Ivison et al., 1998), the first SCUBA galaxy and the brightest of the SCLS galaxies, lensed by Abell 370. I also search for ^{12}CO $J=1-0$ emission in (iv) the Lyman-break galaxy (LBG) A 2218 #284, located 22.1 arcsec from the centre of the lensing cluster in the same field as SMM J16359 (Ebbels et al., 1996). Observations of another SMG lensed by A 1835 from the same project, SMM J14011+0252 at $z = 2.5652$, have been presented in Sharon et al. (2013).

The optical spectrum of SMM J02399, coupled with its extreme luminosity and emission-line widths (FWZI $\sim 1,000\,\mathrm{km\,s^{-1}}$) have long been cited as evidence that this source contains a type-2 active galactic nucleus (AGN; Ivison et al., 1998). SMM J14009 too has long been suspected to host a dust-enshrouded AGN on the basis of the strength of its radio emission ($S_{1.4\,\mathrm{GHz}} = 529 \pm 30\mu$Jy) and compactness (Ivison et al., 2000, Biggs et al. *in prep.*).

The effects of lensing boost the flux density and apparent size of the targets, surface brightness being conserved. Excellent lens models exist for Abell 370, 1835 and 2218 and multi-wavelength imaging has constrained the ages, stellar masses and SFRs of the targets, as well as the mass of warm, star-forming gas as traced by, e.g., ^{12}CO $J=3-2$.

Throughout the chapter I use a cosmology with $H_0 = 71\,\mathrm{km\,s^{-1}\,Mpc^{-1}}$, $\Omega_\mathrm{m} = 0.27$, $\Omega_\Lambda = 0.73$, as outlined in § 1.2, which gives an average angular scale of $8.1\,\mathrm{kpc\,arcsec^{-1}}$ for the sample.

3.1.2 The sample

The observational challenges of conducting multi-wavelength follow-up of SMG sources outlined in Chapter 1 makes defining a ^{12}CO $J=1$–0 sample a formidable

[1]NRAO is operated by Associated Universities Inc., under a cooperative agreement with the National Science Foundation.

Table 3.1: VLA sample and observing log.

Target	Magnifi--ication	z	$\Delta\nu_{\rm obs}$ (GHz)	Configu--ration	Observing dates	Reference
SMM J14009	1.5	2.9344	29.23	DnC	Sep 25, 29, 30 (2010),	Weiß et al. (2009)
			–29.36	CnB	Jan 21, 24, 26, 27 (2011)	
SMM J16359	14, 22, 9[a]	2.5168	32.69	D	Apr 12, 14, 20, May 05, 20 (2010),	Kneib et al. (2004)
			–32.93	C	Dec 31, Jan 04, 06, 10, 11 (2011)	
SMM J02399	2.45	2.808	29.73	D	Sep 27, Oct 26 ×2,	Genzel et al. (2003)
			30.69		Nov 01 ×2 (2011)	

Note: [a]Images A, B, C, respectively.

undertaking. Each of the SMGs studied in the present chapter was initially detected by its rest-frame far-IR emission with SCUBA, whereupon the process of determining their positions and redshifts to the accuracy necessary to permit spectral line follow-up with the VLA began. In the following, I outline the brief observational history of each object in the sample.

SMM J02399–0136

Following the installation of the Submillimetre Common-User Bolometer Array (SCUBA: Holland et al., 1999) on the James Clerk Maxwell Telescope in 1997, SCUBA's "first born", the archetypal submillimetre galaxy SMM J02399–0136 (hereafter SMM J02399) arrived in mid-1997 (Smail et al., 1997). Detected in two 8-hour exposures at 450 and 850-μm in the field of the $z = 0.37$ lensing cluster A 370, the combination of a strong detection at 850-μm ($S_{850} = 13.3\,\mathrm{mJy}$) and weak detection at 450-μm ($S_{450} = 1.8\,\mathrm{mJy}$) immediately suggested that SMM J02399 had spectral properties more akin to those of a cosmologically-distant ($z > 1$) starburst galaxy than those of a hitherto undetected member of the foreground cluster, a conclusion which was subsequently confirmed by counterpart optical, infrared and radio detections at the Canada-France-Hawaii Telescope (CFHT), *HST* and the VLA (Ivison et al., 1998). These data, probing angular scales smaller than those of the JCMT primary beam, showed that SMM J02399 is in fact comprised of at least two distinct components, a broad absorption line (BAL) quasar denoted L1, and a lower surface brightness companion L2, associated with a large Lyman-α emitting cloud, each at a spectroscopically confirmed redshift of $z = 2.803$. The separation of the two optical components was calculated as $\sim 9\,\mathrm{kpc}$, after correcting for the mass model-derived lensing factor $\sim 2.5\times$ (Kneib et al., 1993), but with evidence of low surface brightness 1.4-GHz emission permeating throughout the system and extending across $\sim 24\,\mathrm{kpc}$, possibly the result of an extended, interacting, optically-faint starburst region (Ivison et al., 1998).

With a confirmed redshift in hand, efforts to study the important molecular gas component of SMM J02399 got underway. Using the Owens Valley Millimeter Array, Frayer et al. (1998) obtained an unresolved 8σ detection of ^{12}CO $J = 3-2$ emission ($S_{\mathrm{CO(3-2)}} = 3.3 \pm 0.4\,\mathrm{Jy\,km\,s^{-1}}$) corresponding to $M_{\mathrm{gas}} = 8 \times 10^{10}\,\mathrm{M_\odot}$ across an estimated $\geq 10\,\mathrm{kpc}$ region – assuming a "disk-like"

$\alpha_{\rm CO} = 4\ {\rm M}_\odot\,({\rm K\,km\,s^{-1}\,pc^2})^{-1}$ and a brightness temperature ratio of unity – and a dynamical mass $M_{\rm dyn} \leq 1.5 \times 10^{11}\,{\rm sin}^{-2}(i)\,{\rm M}_\odot$. Later, Genzel et al. (2003) studied 335-μm continuum and ^{12}CO $J = 3-2$ line emission in SMM J02399 at PdBI, finding a double-peaked ^{12}CO profile and that both sources of emission are astrometrically concomitant with L1 only. From this, they concluded that SMM J02399 is likely a massive and rapidly-rotating disk-like galaxy centred at L1, with the second UV peak, L2, representing nothing but back-scattered light from the AGN; however they were unable to rule out the alternative configuration of an interacting pair.

In an effort to map the dynamics of SMM J02399 at high angular resolution, Ivison et al. (2010b) brought together the available radio maps and mid-J ^{12}CO data cubes, and supplemented them with new, deep ACS F475W, F625W and F814W and NICMOS F110W and F160W *HST* images, *Spitzer* IRAC images in four bands from 2.6–8-μm, Keck-I long-slit spectroscopy and upgraded VLA C-configuration ^{12}CO $J = 1-0$ data. Using this new panchromatic dataset, an additional two components were uncovered; L1N, a bright, blue, compact source ~ 8 kpc North of L1, and L2SW, a red feature seen in the NICMOS imaging extending ~ 6 kpc south-east of L1 (see Fig. 1 of Ivison et al., 2010b). Based on these updated data, Ivison et al. (2010b) again argued that the extended radio halo in which these components are embedded more plausibly points toward an unseen, heavily dust-obscured starburst than it does to any special geometric arrangement of quasar, jet, shocked gas reservoir and observer as would be necessary to explain the observed morphology if such an obscured starburst were *not* present. Ivison et al. (2010b) additionally found that the region traced by ^{12}CO $J = 1-0$ – ~ 25 kpc in the source plane – is significantly larger than that traced by the warm mid-J ^{12}CO and hot, ionised gas traced by optical/IR studies, whose distribution traces the excitation structure in a galaxy more so than it traces its true morphology.

In the following analysis, I remain agnostic as to the morphology of SMM J02399, except in as much as I choose to use the "starburst/merger" value of $\alpha_{\rm CO} = 0.8\,{\rm M}_\odot({\rm K\,km\,s^{-1}\,pc^{-2}})$, which results in a total H_2 gas mass $\sim 5\times$ higher than that calculated using the standard Milky Way value.

SMM J16359+6612

SMM J163599+6612 – hereafter SMM J16359 – lies coincident with the core of the $z = 0.17$ A 228 cluster, and is gravitationally lensed by the cluster into three distinct images, each detected with SCUBA at 450 and 850-μm. The three images are marginally resolved at 850-μm, share a common 450/850-μm flux ratio of 4.0$\pm$ 0.4, and each have correspondingly red optical/near-IR counterparts, within the uncertainties due to crowding and differential amplification (Kneib et al., 2004). The three counterpart images are labelled from North-South as SMM J16359-A, SMM J16359-B and SMM J16359-C, and I adhere to this naming convention throughout this chapter.

Keck spectroscopic follow-up observations carried out in 2003 June revealed the Hα line and [NII] doublet at a redshift $z = 2.5165 \pm 0.0015$. After correcting for lensing, the observed Hα line flux corresponds to a SFR of $11\,\mathrm{M_\odot\,yr^{-1}}$ (Kneib et al., 2004), compared to that derived from the far-IR luminosity – $500\,\mathrm{M_\odot\,yr^{-1}}$ — which indicates that the bulk of the star formation event in SMM J16359 is heavily obscured.

The molecular gas properties of SMM J16359 were first studied via PdBI imaging of ^{12}CO $J = 7-6$ and $J = 3-2$ (Kneib et al., 2005), whereupon broad lines (FWZI $= 550\,\mathrm{km\,s^{-1}}$) were detected at a luminosity-weighted redshift of $z_{\mathrm{CO}} = 2.5174 \pm 0.0002$, with luminosity ratios between the three components in accordance with those of the single-dish submillimetre maps. The double-peaked ^{12}CO $J = 3-2$ line profile and velocity structure of the brightest component (B) are consistent with either the interpretation of SMM J16359 as a massive gas disk, or as the product of a late-stage major merger. The derived ^{12}CO total gas mass – $(4.5 \pm 1.0) \times 10^9\,\mathrm{M_\odot}$ – is significantly lower than that of SMM J02399, despite the SFR being similar, indicating that the star formation event in SMM J16359 will likely exhaust its gas supply much sooner, if it maintains its present SFR until depletion. This highly-efficient star formation may be interpreted as evidence for the major-merger hypothesis, though uncertainties due to α_{CO} are large enough to accommodate a $\sim 5\times$ more massive gas reservoir, and hence a $\sim 5\times$ less intense SFR/M_{gas} ratio.

SMM J14009

SMM J14009+0252 (hereafter SMM J14009), one of the brightest early SMGs ($S_{850\mu m}$ = 15.6 mJy; Ivison et al., 2000), and gravitationally lensed by A 1835 (z = 0.25), was first detected in 1998 with SCUBA, and in the same year at the VLA. Initial photometric redshift estimates constrained the source to lie between z = 2.8–5 (Ivison et al., 2000; Yun & Carilli, 2002; Hempel et al., 2008). Nevertheless, the extreme optical faintness of SMM J14009 long prohibited spectroscopic determination of its redshift, hindering efforts to study the source in detail, until the blind detection of ^{12}CO $J = 5-4$ and $J = 3-2$ by Weiß et al. (2009), carried out using the new Eight MIxer Receiver (EMIR) on the IRAM 30 m telescope, from which a precise spectroscopic redshift of $z = 2.9344$ was determined. With a lens magnification factor μ = 1.5 (Ivison et al., 2000), Weiß et al. (2009) measured $M_{\rm gas} = 6.5 \times 10^{10} {\rm M}_{\odot}$, while the measured $L_{\rm IR} \sim 3 \times 10^{12}\,{\rm L}_{\odot}$ – five times lower than that predicted from the 1.4-GHz flux density and the far-infrared/radio correlation – indicates SFR= $500\,{\rm M}_{\odot}\,{\rm yr}^{-1}$ and classifies SMM J14009 as a ULIRG hosting a radio-loud AGN.

3.2 Observations and data reduction

3.2.1 VLA ^{12}CO $J=1-0$ observations

Observations of SMM J14009 and SMM J16359 were carried out in blocks of 2–4 hr during excellent weather conditions between 2010 April and 2011 January (Project IDs: AI139 and AI142). Over this Open Shared Risk Observing period the available bandwidth from the new Wideband Interferometric Digital ARchitecture (WIDAR) correlator consisted of two sub-band pairs, each with 64 × 2-MHz dual-polarisation channels, and the number of useful Ka receivers roughly doubled, from ∼ 10 to ∼ 20. Due to the different redshifts of the targets, different tuning strategies had to be employed in each case: for SMM J16359 I used both sub-band pairs with the frequency of the redshifted ^{12}CO $J = 1-0$ line ($\nu_{\rm rest}$ = 115.27120256 GHz – Morton & Noreau, 1994) placed in channel 40 of the lower sub-band and a 10-channel overlap between the two sub-bands to mitigate the effects of noise in the edge channels. This configuration gave velocity coverage and resolution of ∼2,000 km s^{-1} and ∼18 km s^{-1} , respectively. For the

higher-redshift SMM J14009, the redshifted emission was accessible to only one of the two sub-bands and the line was placed in its centre providing ∼1,300 km s^{-1} coverage, the other sub-band being tuned to $\nu_{\rm obs} = 32.4$ GHz in order to constrain the ∼115-GHz radio continuum.

By the time SMM J02399 was observed during 2011 September through November (Project ID: AT400), the OSRO capabilities had been upgraded to include two independently tunable output pairs of eight sub-bands each, with 128 × 1-MHz dual-polarisation channels per sub-band, giving a total available bandwidth of 2,048 MHz. Again, however, the redshift of SMM J02399 could be reached by only the BD output pair, giving ∼20,000 km s^{-1} of coverage and ∼10 km s^{-1} resolution. The 8 sub-bands of output pair AC were tuned continuously at the lowest possible central frequency, 32.52 GHz, to constrain the radio continuum emission from this source.

For SMM J16359, approximately 19 and 14 hr of useful data were obtained in the VLA's D and C configurations; for the equatorial target SMM J14009, the DnC and CnB configurations (with their longer northern arms) were used, with integration times of 8 and 16 hr, respectively. 10 hr of on-source D configuration observations were performed for SMM J02399, though an unfortunate technical problem with the correlator resulted in only 1/3 of the observed data being recorded.

Antenna pointing was checked using the C-band receivers every 60–90 min, and immediately prior to scans of the flux calibrator (3C 286 for SMM J14009 and SMM J16359; 3C 48 for SMM J02399). Amplitude and phase were tracked with brief scans of J1642+6856 (for SMM J16359), J1354−0206 (for SMM J14009) and J0239−0234 (for SMM J02399), every 5 min. These data were also used to determine the bandpass.

The data were reduced in accordance with the $\mathcal{AIPS}$ data reduction outlined in Chapter 2, and imaged using IMAGR and the CLEAN algorithm. Cubes were made with 6-MHz (∼ 50-km s^{-1}) resolution by binning the native VLA channels in trios to boost signal-to-noise. I used natural weighting, and applied Gaussian *uv* tapers from 100–1000 kλ in steps of 100 kλ to check for any flux which may have been resolved out in the high-resolution images but found no evidence for significant missing flux in any of the sources. The resulting synthesised beam sizes are 0.88 × 0.72 arcsec^2 with position angle (PA) 125° for SMM J14009, 1.07 ×

0.72 arcsec^2 at PA 22° for SMM J16359 and 3.08 × 2.56 arcsec^2 at PA 160° for SMM J02399; the integrated maps (Fig. 3.1) reach down to a noise levels of 20, 11 and 20 μJy beam^{-1}, respectively.

Plots of the *uv* coverage of the final, multi-configuration files for each source are shown in Fig. 3.2.

Spectra (see Fig. 3.3) were extracted from the data cubes with the $\mathcal{AIPS}$ task, ISPEC, which sums the flux density within a box around the source for each plane in the cube. Error spectra were produced by extracting five off-source spectra and calculating the standard deviations among these five sky spectra for each spectral channel. The mean noise values per spectral channel for SMM J14009, SMM J16359 and SMM J02399 were 0.09, 0.17 and 0.13 mJy beam^{-1}, respectively.

Line fluxes were measured by integrating the emission spectra across the width of each ^{12}CO line and then checked via the equivalent integrated image. In determining both the observed and derived source properties, the three images of SMM J16359 were treated as individual sources and then the results were co-added to give magnification-weighted averages where physically appropriate.

3.2.2 Infrared observations

Throughout the chapter, I make reference to the infrared properties of the sources, including calculations of the SFR derived from rest-frame 8–1000 μm luminosities, $L_{\rm IR}$. Here, I present the measurements used to derive these quantities.

Using archival data from *Herschel* (Pilbratt et al., 2010), I measure $S_{250\mu m}$, $S_{350\mu m}$ and $S_{500\mu m}$, and collate SCUBA flux densities at 750-, 850- and 1350-μm. I then fit far-infrared templates from the SED library of Chary & Elbaz (2001, hereafter CE01) to the photometry in order to determine $L_{\rm IR}$ for each galaxy.

For SMM J02399 I include the mid-IR spectrum of Lutz et al. (2005), with data covering $\lambda_{\rm obs} \geq 750\mu$m taken from Ivison et al. (1998). In Fig. 3.4 we see the excellent agreement between the data and the best-fit SED template. The derived value of $L_{\rm IR} = (80.7 \pm 8.1) \times 10^{11}\,{\rm L}_{\odot}$ is 30 per cent lower than the value reported in Ivison et al. (1998).

For SMM J16359 I include published flux densities for the three images at 24- and 70-μm from Kneib et al. (2004). The three images are resolved by *Herschel* up to 350-μm but become blended at longer wavelengths. Where the three images are blended, I divide up the observed flux in proportion to the known magnification

factors. The magnification-weighted mean is $L_{\rm IR} = (6.4{\pm}1.0){\times}10^{11}\,{\rm L}_{\odot}$, consistent with the results of Finkelstein et al. (2011), who determined $L_{\rm IR} = 7.0 \times 10^{11}\,{\rm L}_{\odot}$ (for image B) using a similar SED-fitting method.

Similarly, for SMM J14009 I rely on the 24-μm measurement from Hempel et al. (2008) to supplement the archival *Herschel* and SCUBA data, and compute a lensing-corrected $L_{\rm IR} = (160 \pm 24) \times 10^{11}\,{\rm L}_{\odot}$.

The best-fit CE01 SEDs for each galaxy are shown with the corresponding photometry in Fig. 3.4.

3.2.3 Radio continuum

The VLA tuning strategies employed to observe ^{12}CO $J{=}1$–0 in for SMM J14009 and SMM J02399 enabled detections of the $\sim$ 115-GHz rest-frame (32-GHz observed) continuum emission from these galaxies. These data were reduced in parallel with and according to the same recipe as the ^{12}CO spectral-line data. There is no continuum data at this frequency for SMM J16359, owing to the lack of bandwidth and different tuning strategy used for this source. I measure continuum flux densities of $S_{32\,\rm GHz} = 57 \pm 25\,\mu$Jy for SMM J02399 and $S_{32\,\rm GHz} = 42 \pm 20\,\mu$Jy for SMM J14009. 1.4-GHz flux densities of $S_{1.4\,\rm GHz} = 526 \pm 50$ and $529 \pm 30\,\mu$Jy were determined in Ivison et al. (1998) and Ivison et al. (2000) for SMM J02399 and SMM J14009, respectively. The VLA science archive was queried for continuum data at 5- and 8-GHz as well, with flux densities reported in Table. 3.4. The radio continuum data are plotted with the IR SEDs in Fig. 3.4.

3.3 Results

3.3.1 ^{12}CO$J{=}1{-}0$ morphologies and spectra

The source properties are summarised in Table 2. All sources are detected in ^{12}CO $J = 1-0$ with a significance of 13σ for SMM J16359-B (the brightest of three images of this multiply-lensed source), 17σ for SMM J14009 and 7.5σ for SMM J02399 at the brightest pixel in each image. The flux-weighted ^{12}CO $J{=}1$–0 redshifts are derived by fitting a single Gaussian component to each ^{12}CO $J{=}1$–0 spectrum and are consistent with the reference ^{12}CO $J = 3-2$ redshifts to four significant figures.

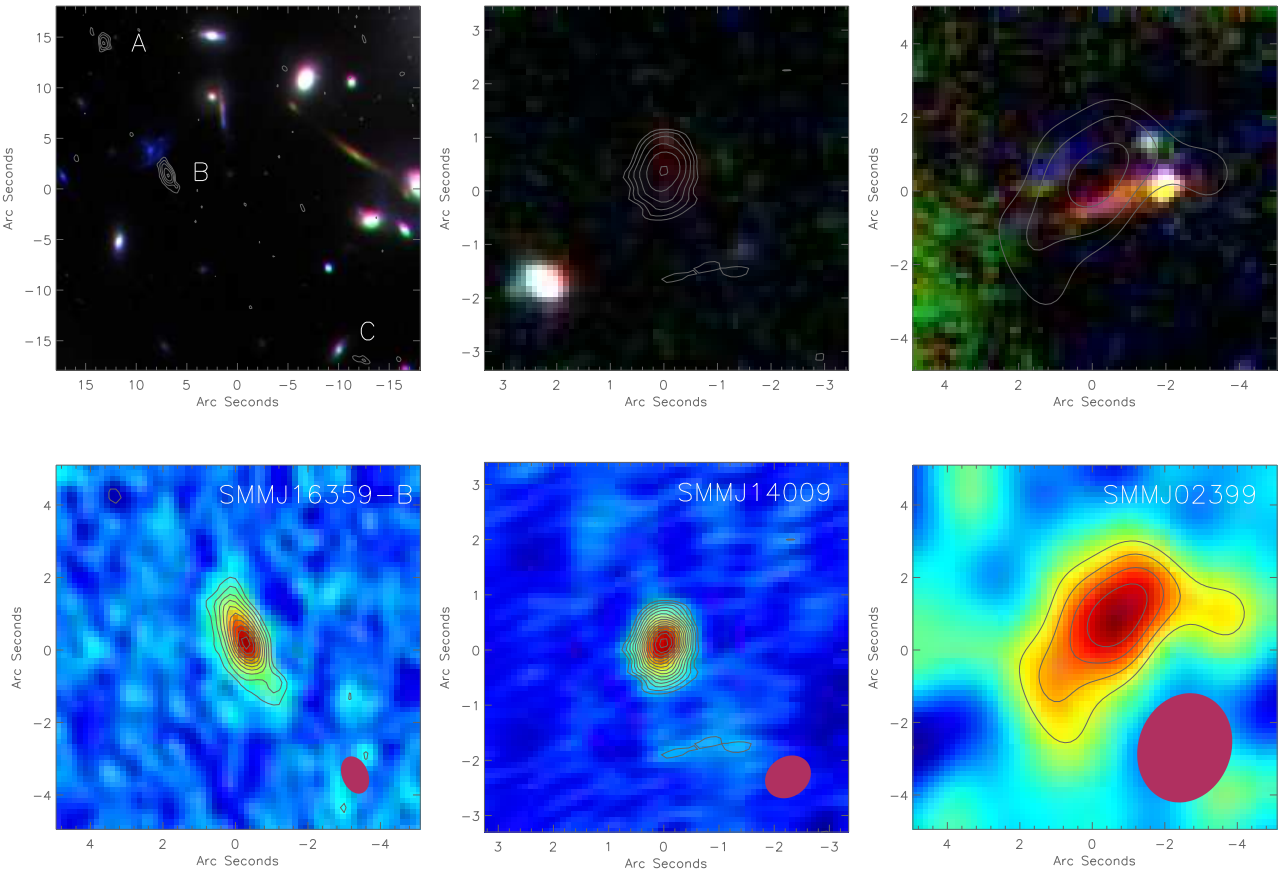

Figure 3.1: *Top row:* ^{12}CO $J=1-0$ contours spaced at -3, 3, 4.24, 6...$\times\sigma$ (and in steps of $\sqrt{2}\sigma$ thereafter) set on top of three-colour *HST* optical images of the foreground clusters. The relationship between the molecular gas in SMM J02399 and its optically-bright counterparts has been discussed in Ivison et al. (2010c). In the field of A 2218, I detect three distinct ^{12}CO $J=1$–0 images of SMM J16359, as did Kneib et al. (2005) in their mid-J ^{12}CO study. For SMM J14009 I see no evidence of any strong optical counterpart to the ^{12}CO emission. *Bottom row:* Integrated ^{12}CO $J=1-0$ maps of the three SMG targets, SMM J16359-B (10 arcsec/side), SMM J14009 (6.5 arcsec/side) and SMM J02399 (14 arcsec/side), set on top of colour representations of the same ^{12}CO data. Contours are displayed at -3,3,4,5...$\times\sigma$, and in each case, the VLA synthesised beam is represented by a maroon ellipse in the bottom-right corner.

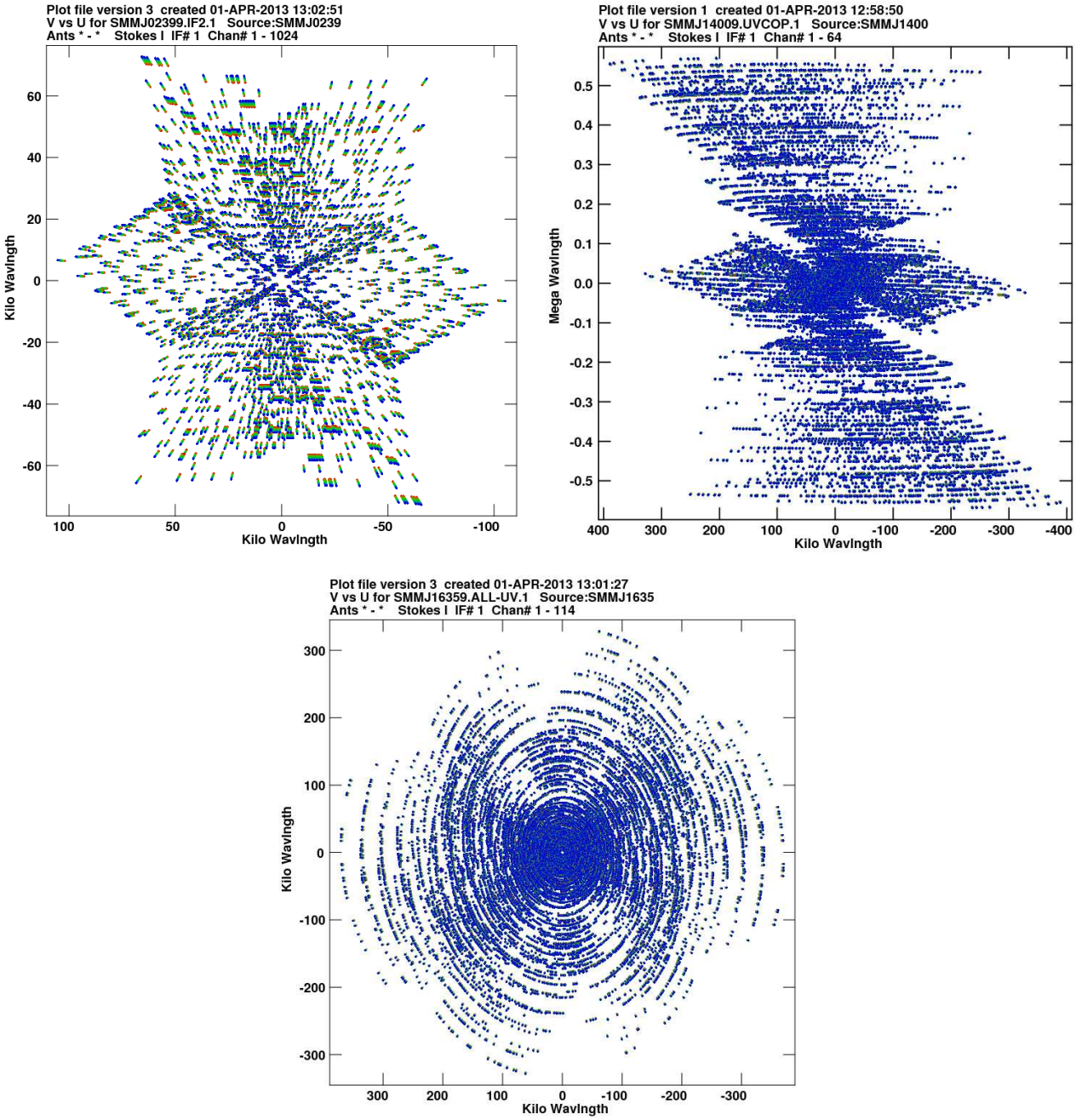

Figure 3.2: *uv* coverage of the VLA ^{12}CO $J = 1 - 0$ visibilities for SMM J02399, SMM J14009 and SMM J16359.

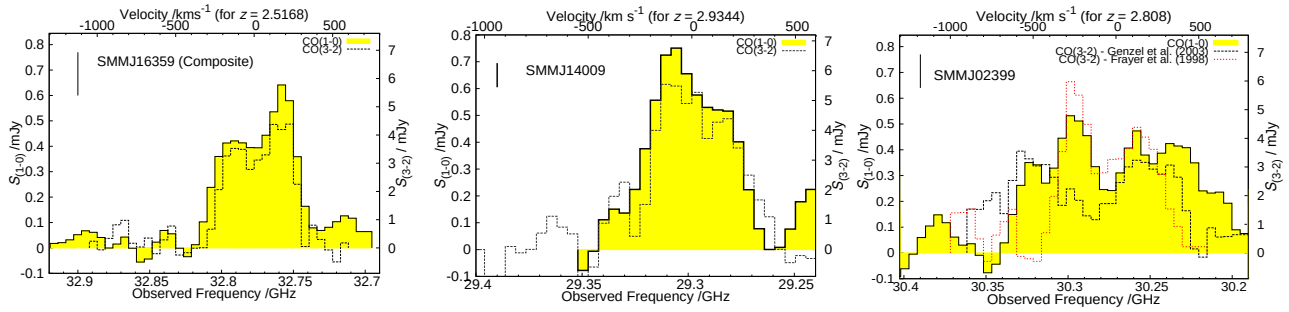

Figure 3.3: ^{12}CO $J = 1-0$ spectra (yellow histograms) and reference $J = 3-2$ spectra (dotted lines) for the three targets. The left-hand scale represents $J = 1-0$ flux density, and the right-hand side shows the corresponding $J = 3$–2 flux density, scaled by 9^{-1} so as to be on the same Rayleigh-Jeans $T_{\rm b}$ scale. The zero-LSR redshifts used to determine the relative velocities for each source are quoted in the figure, and typical error bars are shown in the top-left-hand corner of each plot. The spectrum shown for SMM J16359 is the magnification-weighted mean of the spectra of the three images of this source, SMM J16359-A, -B and -C as defined in Kneib et al. (2004).

Velocity-integrated maps and spectra are shown in Figs, 3.1 & 3.3. The spectrum shown for SMM J16359 is a magnification-weighted average of the spectra from each image of this source. The uncertainties in the spectral fits translate to velocity uncertainties that are typically of order $\Delta V = 10$–$15\,{\rm km\,s^{-1}}$, except in the case of SMM J02399 where the comparatively low signal-to-noise hampers our ability to constrain $z_{\rm CO}$ and results in $\Delta V \sim 50\,{\rm km\,s^{-1}}$. For each source we see broad lines with full width at zero intensity (FWZI) of ∼500–1,000 $\rm km\,s^{-1}$.

Comparing the line profiles and maps between $J = 1-0$ and $J = 3-2$ observations, we see firstly that the astrometry is consistent. For SMM J16359 and SMM J14009 we additionally see good agreement between the low-J and mid-J ^{12}CO line profiles. In the former, we see evidence of double-peaked $J = 1-0$ line profiles for each of the three images, separated by $\sim$300 $\rm km\,s^{-1}$, as did Kneib et al. (2005) in their study of the $J = 3-2$ emission. SMM J02399 displays a significant offset in velocity between the measured $J = 1-0$ emission and the $J = 3$–2 spectrum of Genzel et al. (2003) – $\sim$100 $\rm km\,s^{-1}$, roughly twice that which could be ascribed to uncertainties in the Gaussian fits. However, the $J = 1$–0 and $J = 3-2$-derived redshifts are consistent to four significant figures ($z = 2.808$). It is difficult to envisage any plausible physical origin for these offsets: in an effort

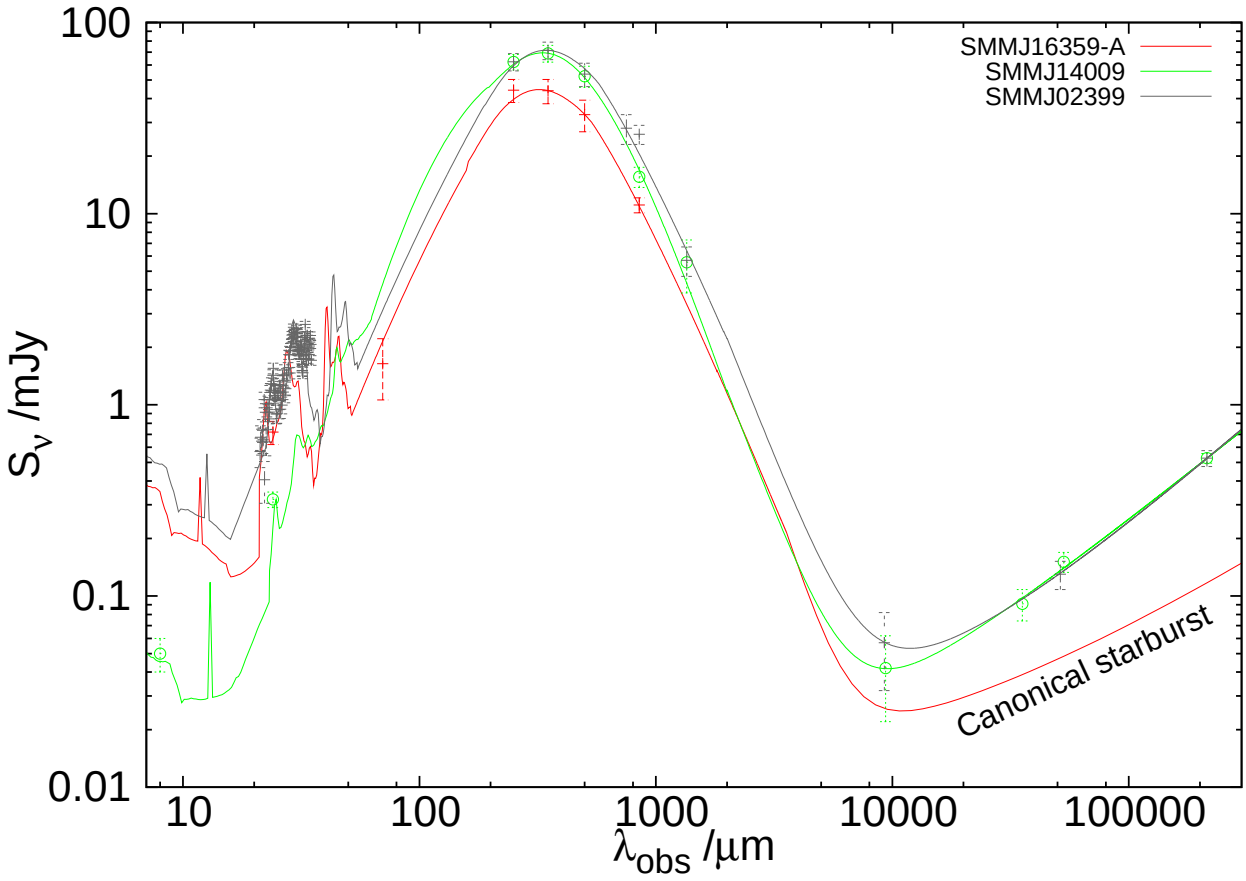

Figure 3.4: Observed-frame infrared SEDs for each of the sources, uncorrected for lensing, including data (*colour-coded: see legend*) and the corresponding best-fit CE01 SED (solid lines). I include only data up to $\lambda_{\rm obs} = 1350\,\mu$m in the fits. For clarity, I plot the SED of only one image of SMM J16359, and plot the best-fit CE01 template out to radio wavelengths, demonstrating the "canonical starburst" radio SED. For the other two galaxies, I truncate the CE01 SED at 2,000 μm and plot the modelled radio SEDs (§ 3.3.5), constrained by new measurements of the Ka-band continuum flux densities and previously published results at longer wavelengths. I interpret the steepness of the radio spectra in SMM J02399 and SMM J14009 as being consistent with the known AGN hosted by these galaxies.

to track down any instrumental contribution to the frequency offsets, continuous-wave tones were injected into the Ka-band receivers at frequencies close to those used for the science observations, but no offsets were observed between the input and observed tones (Emmanuel Momjian, private communication).

I find a weighted mean velocity width ratio of $\sigma_{(1-0)/(3-2)} = 1.3 \pm 0.1$ for the three images of SMM J16359, consistent with the findings of Ivison et al. (2011) for a sample of four unlensed SMGs. For the two more AGN-like galaxies in this sample, SMM J14009 and SMM J02399, I detect velocity width ratios consistent with unity ($\sigma_{(1-0)/(3-2)} = 1.06 \pm 0.08$ and 1.05 ± 0.26 respectively).

3.3.2 Line luminosities and derived total gas masses

Traditionally, attempts to determine the molecular gas mass of distant galaxies via ^{12}CO emission have been subject to two main sources of uncertainty: (1) where mid-J lines are observed, a brightness temperature ratio, $r_{(3-2)/(1-0)} = 1$ is typically assumed to convert the *measured* mid-J velocity-integrated luminosity to an *inferred* $J = 1-0$ luminosity, $L'_{\rm CO}$, and (2) the "X-factor", $\alpha_{\rm CO} = M({\rm H_2})/L'_{\rm CO(1-0)}$ (Downes & Solomon, 1998), which is used to convert the observed or inferred ^{12}CO $J = 1-0$ luminosity to a total molecular gas mass. As a number of recent papers have shown (e.g. Harris et al., 2010; Ivison et al., 2011, etc.), observed $r_{(3-2)/(1-0)}$ ratios in SMGs are typically well below unity. We can thus improve our gas mass estimates by observing the ^{12}CO line which traces the bulk of the molecular gas reservoir, but we must still worry about the order of magnitude range spanned by $\alpha_{\rm CO}$ depending on the assumed state of the underlying ISM: $\alpha_{\rm CO} \sim 5\,{\rm M_\odot}\,({\rm K\,km\,s^{-1}\,pc^2})^{-1}$ in optically-thick giant molecular clouds (GMCs) where the gas is reducible to ensembles of self-gravitating units, whereas $\alpha_{\rm CO} \sim 0.8\,{\rm M_\odot}\,({\rm K\,km\,s^{-1}\,pc^2})^{-1}$ in the more extreme environments of local ultra luminous infrared galaxies (ULIRGs), where the ISM forms a smooth, continuous medium. This latter value is typically adopted for SMGs.

The intrinsic ^{12}CO $J=1-0$ line luminosity is the observed line flux integrated across the surface area and velocity range of the line, divided by the magnification factor μ: $L'_{\rm CO} = \mu^{-1} \int_{\Delta V} \int_{A_s} S_\nu \, dA \, dV$ K km s^{-1} pc^2, or:

Table 3.2: Observed properties.

Target	$z_{\rm CO(1-0)}$	$I_{\rm CO(1-0)}$ (Jy km s^{-1})	$I_{\rm CO(3-2)}$ (Jy km s^{-1})	$r_{3-2/1-0}$	$\sigma_{\rm CO(1-0)}$ (km s^{-1})	$\sigma_{\rm CO(1-0)/CO(3-2)}$ (km s^{-1})	FWZI (km s^{-1})	R (kpc)
SMM J14009	2.9332 ± 0.0001	0.31 ± 0.02	2.70 ± 0.30	0.95 ± 0.12	175 ± 10	1.06 ± 0.08	850	1.2 ± 0.4
SMM J02399	2.8083 ± 0.0007	0.60 ± 0.12	3.10 ± 0.40	0.58 ± 0.14	350 ± 90	1.05 ± 0.26	1300	26 ± 4
SMM J16359-A	2.5174 ± 0.0002	0.22 ± 0.04	1.67 ± 0.13	0.83 ± 0.15	195 ± 15	1.10 ± 0.09	710	< 1
SMM J16359-B	2.5173 ± 0.0001	0.40 ± 0.04	2.50 ± 0.12	0.70 ± 0.22	190 ± 10	1.26 ± 0.07	780	0.6 ± 0.3
SMM J16359-C	2.5179 ± 0.0002	0.30 ± 0.09	1.58 ± 0.17	0.59 ± 0.20	305 ± 15	1.81 ± 0.09	670	4 ± 2

Table 3.3: Lensing-corrected properties

Target	$L'_{\rm CO(1-0)}$ ($\times 10^9$ K km s^{-1} pc^2)	$M_{\rm gas,\alpha}$ ($\times 10^9$ M$_\odot$)	$m_{\rm CQ/SF}$	$L^a_{\rm IR}$ ($\times 10^{11}$ L$_\odot$)	$M_{\rm gas,I11}$ ($\times 10^9$ M$_\odot$)	$M_{\rm dyn}$ ($\times 10^9$ M$_\odot$)
SMM J14009	83 ± 6	67 ± 4	0.09 ± 0.02	160 ± 16	35 ± 7	18 ± 4
SMM J02399	96.6 ± 1.9	77 ± 15	1.5 ± 0.5	81 ± 8	41 ± 14	1560 ± 550
SMM J16359-A	4.9 ± 0.8	3.9 ± 0.6	0.33 ± 0.09	7.1 ± 0.7	1.3 ± 0.4	< 19
SMM J16359-B	5.5 ± 0.6	4.4 ± 0.5	0.8 ± 0.3	6.2 ± 0.6	2.8 ± 1.3	11 ± 4
SMM J16359-C	10 ± 3	8 ± 2	1.4 ± 0.7	5.7 ± 0.6	1.5 ± 0.7	180 ± 70
A2218 #384	$3\sigma < 0.8$	$3\sigma < 0.6$	–	–	–	–

Note: [a]Calculations for $L_{\rm IR}$ discussed in §3.2.2. All luminosities have been corrected for the known magnification factors.

$$L'_{\mathrm{CO}(1-0)} = \frac{3.25\times10^7}{\mu}\left[\frac{D_{\mathrm{L}}^2(\mathrm{Mpc})}{1+z}\right]\left(\frac{\nu_{\mathrm{rest}}}{\mathrm{GHz}}\right)^{-2} \times\left[\frac{\int_{\Delta V} S_\nu d\nu}{\mathrm{Jy\,km\,s^{-1}\,pc^2}}\right]\mathrm{K\,km\,s^{-1}\,pc^2} \tag{3.1}$$

Then we define $M_{\mathrm{gas},\alpha} = \alpha_{\mathrm{CO}} L'_{\mathrm{CO}(1-0)}$, and use the ULIRG-like value of α_{CO} to determine gas masses of $(67\pm4)\times10^9\mathrm{M}_\odot$, $(77\pm15)\times10^9\mathrm{M}_\odot$ and $(4.4\pm0.5)\times10^9\mathrm{M}_\odot$ respectively, for SMM J14009, SMM J02399 and SMM J16359-B.

Combining these new ^{12}CO $J=1$–0 data with existing $J=3$–2 data from Kneib et al. (2005, SMM J16359), Weiß et al. (2009, SMM J14009) and Genzel et al. (2003, SMM J02399) allows me to derive a mean magnification-weighted T_{b} ratio of $r_{(3-2)/(1-0)} = 0.72\pm0.12$ for the three images of SMM J16359, $r_{(3-2)/(1-0)} = 0.95\pm0.25$ for SMM J14009 and $r_{(3-2)/(1-0)} = 0.58\pm0.14$ for SMM J02399: SMGs on average experience *sub-thermal* excitation. One can then compare the gas mass derived above ($M_{\mathrm{gas},\alpha}$) with a gas mass derived according to the prescription of Ivison et al. (2011), denoted $M_{\mathrm{gas,I11}}$, in which a lower limit for the mass of actively star-forming gas (M_{SF}) is computed on the assumption that SMGs form stars at an appreciable fraction of Eddington-Limited star-formation efficiency ($\mathrm{SFE}_{\mathrm{max}} = L_{\mathrm{IR}}/M_{\mathrm{SF}} \leq 500\,\mathrm{L}_\odot\,\mathrm{M}_\odot^{-1}$ where L_{IR} is the lensing-corrected infrared luminosity: Scoville, 2004). For such maximally-efficient star formation, a measurement of L_{IR} therefore corresponds to a determination of M_{SF}. Using canonical brightness temperature ratios for cold, quiescent ($r^{(\mathrm{CQ})}_{(3-2)/(1-0)} = 0.3$) and warm, star-forming ($r^{(\mathrm{SF})}_{(3-2)/(1-0)} = 1.0$) gas, their relative fractions in a sub-thermally-excited reservoir can be computed as

$$m_{\mathrm{CQ/SF}} = \frac{r^{(\mathrm{SF})}_{(3-2)/(1-0)} - r_{(3-2)/(1-0)}}{r_{(3-2)/(1-0)} - r^{(\mathrm{CQ})}_{(3-2)/(1-0)}} \tag{3.2}$$

and the total molecular gas mass is thus

$$M_{\mathrm{gas}} = M_{\mathrm{SF}}(1 + m_{\mathrm{CQ/SF}}) \tag{3.3}$$

Computing $M_{\rm gas}$ in this way provides an independent check on the total gas mass, based on different assumptions from those that underpin the $\alpha_{\rm CO}$ method. The magnification-weighted mean value of $M_{\rm gas,I11}$ for SMM J16359 is $(2.1\pm0.6)\times 10^9\,{\rm M}_\odot$, and for SMM J02399 I measure $(41.0\pm14.4)\times10^9\,{\rm M}_\odot$ of gas using this method. For SMM J14009 I calculate $M_{\rm gas,I11}=(34.9\pm7.3)\times10^9\,{\rm M}_\odot$. All three values of $M_{\rm gas,I11}$ are $\sim2\times$ lower than the equivalent values calculated via $\alpha_{\rm CO}$, which would imply $\alpha_{\rm CO}\sim0.4$. I remind the reader, however, that $M_{\rm gas,I11}$ is calculated on the assumption that SMGs have maximal SFE: if the SFE is *less* than $500\,{\rm L}_\odot\,{\rm M}_\odot^{-1}$, then a higher mass of star-forming gas is required for a given $L_{\rm IR}$, raising the total gas mass in the system accordingly.

One may then compare these gas masses to the dynamical mass, for which a multitude of different estimators are present in the literature. In Walker et al. (2009), the dynamical mass enclosed within the stellar half-light radius $r_{\rm half}$ of a spherically-symmetric, pressure-supported system is expressed as

$$M(r)=\frac{5r_{\rm half}\sigma^2\left(\frac{r}{r_{\rm half}}\right)^3}{G\left(1+r^2/r_{\rm half}^2\right)} \tag{3.4}$$

for a Plummer stellar density profile, where σ is the observed velocity dispersion.

The *HST* I_{775}-band half light radius of the starburst in SMM J02399 is $r_{\rm half}=3.0\pm0.3\,{\rm kpc}$ (Swinbank et al., 2010a), suggesting $M_{\rm dyn}(<r_{\rm half})=(2.2\pm0.8)\times10^{11}\,{\rm M}_\odot$. SMM J14009 lacks any obvious optical counterpart (Weiß et al., 2009), precluding a determination of $r_{\rm half}$, while concerns about the gravitational lens model of A 2218 dissuaded Aguirre et al. (2013) from measuring $r_{\rm half}$ for SMM J16359 in their *HST* NICMOS survey of optically-bright SMGs. If we instead adopt a typical SMG half light radius of $r_{\rm half}=3.4\pm0.3\,{\rm kpc}$ (e.g. Swinbank et al., 2010a; Aguirre et al., 2013) for these two SMGs, then the dynamical masses implied by the Walker et al. (2009) formalism are $M_{\rm dyn}=(7.1\pm0.8)\times10^{10}\,{\rm M}_\odot$ and $(6.1\pm0.7)\times10^{10}\,{\rm M}_\odot$, respectively.

For the sake of consistency with the literature, I also consider the isotropic virial estimator ($M_{\rm dyn}=2.1\,R\,\sigma^2_{\rm CO(1-0)}/G$: Spitzer, 1987; Tacconi et al., 2008; Ivison et al., 2011), where R is the measured radius of the molecular gas reservoir, and is determined by fitting a two-dimensional Gaussian to each integrated

^{12}CO $J = 1-0$ map and dividing the semi-major axis by the amplification. The corresponding values of $\sigma_{\rm CO(1-0)}$ are measured from the ^{12}CO $J = 1-0$ spectra (and are recorded in Table 3.2). Using this method, I measure dynamical masses of $(1.8 \pm 0.5) \times 10^{10}\,{\rm M}_{\odot}$, $(1.1 \pm 0.4) \times 10^{10}\,{\rm M}_{\odot}$ and $(1.6 \pm 0.6) \times 10^{12}\,{\rm M}_{\odot}$ for SMM J14009, SMM J16359-B and SMM J02399, where in each case the uncertainties are the result of combining formal errors on R and $\sigma_{\rm CO(1-0)}$, and do not include any uncertainties arising due to the virial mass assumption itself.

SMM J14009 and SMM J16359 both host cold gas reservoirs which are compact by SMG standards ($R < 1\,$kpc), but not unprecedentedly so (e.g. Carilli et al., 2002; Tacconi et al., 2008). By contrast, the gas in SMM J02399 was reported as having a lensing-corrected extent of $\sim$25 kpc in Ivison et al. (2010b) in their C-configuration observations, corroborating the equally large extent of $(26 \pm 4)\,$kpc reported in Table 3.2, derived from these new, independent D-configuration observations. The implied upper-limits on $\alpha_{\rm CO}$ using the Tacconi et al. (2008) dynamical masses are $\alpha_{\rm CO} < 0.3$, $\alpha_{\rm CO} < 2.8$ and $\alpha_{\rm CO} < 24$, for SMM J14009, SMM J16359 and SMM J02399 respectively. Using the Walker et al. (2009) dynamical masses, these values are $\alpha_{\rm CO} < 1.2$, $\alpha_{\rm CO} < 16$ and $\alpha_{\rm CO} < 3.3$, respectively. The large spread in these dynamical mass estimates reflects the differing methodologies used to measure them, specifically: (i) the radius at which the dynamical mass estimate is made (i.e. the stellar half-light radius versus the radius of the molecular gas reservoir); and (ii) a small difference in the constant of proportionality ($5/2G$ in the Walker et al., 2009 expression, as opposed to $2.1/G$ in Tacconi et al., 2008).

3.3.3 Gas excitation

Having worked with canonical brightness temperature ratios to estimate $M_{\rm gas}$, free from any assumptions about $\alpha_{\rm CO}$, I now compare the ^{12}CO $J=1-0$ spectra and the literature $J = 3-2$ spectra in order to determine the true excitation conditions of the gas in this sample of galaxies.

The steepness of the observed radio continuum spectrum of SMM J02399 (§3.2.3) is consistent with the claim that this source harbours a powerful AGN. Such an AGN might be expected to heat the surrounding gas via bombardment with X-rays (Meijerink et al., 2006) or through shock-heating as the powerful radio jet drives into the surrounding molecular gas (Papadopoulos et al., 2012; Ivison

et al., 2012), yet the $T_{\rm b}$ ratio detected for this source $r_{(3-2)/(1-0)} = 0.58 \pm 0.14$ is entirely consistent with that of less AGN-like SMGs. As Ivison et al. (2010b) observe, however, SMM J02399 appears to consist of three or more interacting galaxies embedded within a larger reservoir of cold molecular gas. In particular, the massive, obscured starburst which gives rise to the extreme $L_{\rm IR}$ of this source is spatially offset from the broad-absorption-line quasar.

The improved sampling of the radio SED of SMM J14009 allows me to determine that this source also likely has a steep radio continuum spectrum (§3.2.3), corroborating its classification as an AGN. Additionally, SMM J14009 demonstrates a high $T_{\rm b}$ ratio, $r_{(3-2)/(1-0)} = 0.95 \pm 0.12$, which indicates the presence of a warm gas phase, given the excitation requirements of the ^{12}CO $J=3-2$ transition, $n_{\rm crit} \sim 10^4\,{\rm cm}^{-3}$, $E_{\rm u}/k_{\rm B} \sim 33\,{\rm K}$.

For SMM J16359, the magnification-weighted mean $T_{\rm b}$ ratio, $r_{(3-2)/(1-0)} = 0.72 \pm 0.12$, is entirely consistent with that of the non-AGN harbouring SMG population (Harris et al., 2010; Ivison et al., 2011).

In addition to calculating source-averaged $T_{\rm b}$ ratios, the new interferometric $J = 1-0$ data provide the spatial and spectral resolution to assess $r_{(3-2)/(1-0)}$ as functions of position and velocity. In Fig. 3.5 we see the variation in gas excitation across the observed line profiles for the three sources. I consider the results to be robust only within the central $\pm 400\,{\rm km\,s}^{-1}$ of each of the line profiles due to deteriorating signal/noise at the edges of the line profiles; nevertheless, in SMM J16359 we see clear structure in the plot of $r_{(3-2)/(1-0)}$ versus velocity, with $r_{(3-2)/(1-0)} \sim 1$ for regions in the centre of the velocity-space, rolling off to sub-thermal values for the high-velocity wings of the line. These variations in the velocity fields of each galaxy may point to spatial variations in $r_{(3-2)/(1-0)}$, and are consistent with the observed values of $\sigma_{(3-2)/(1-0)}$.

I attempt to investigate the velocity structure of these galaxies by constructing position-velocity (PV) diagrams for each source, extracting a slice through the (right-ascension, declination, velocity) data cube along the major axis of the galaxy. The resultant PV diagrams are shown in Fig. 3.6; the PV diagram for SMM J16359-B shows hints of ordered rotation, however the low signal-to-noise in all cubes precludes detailed modelling of their emission.

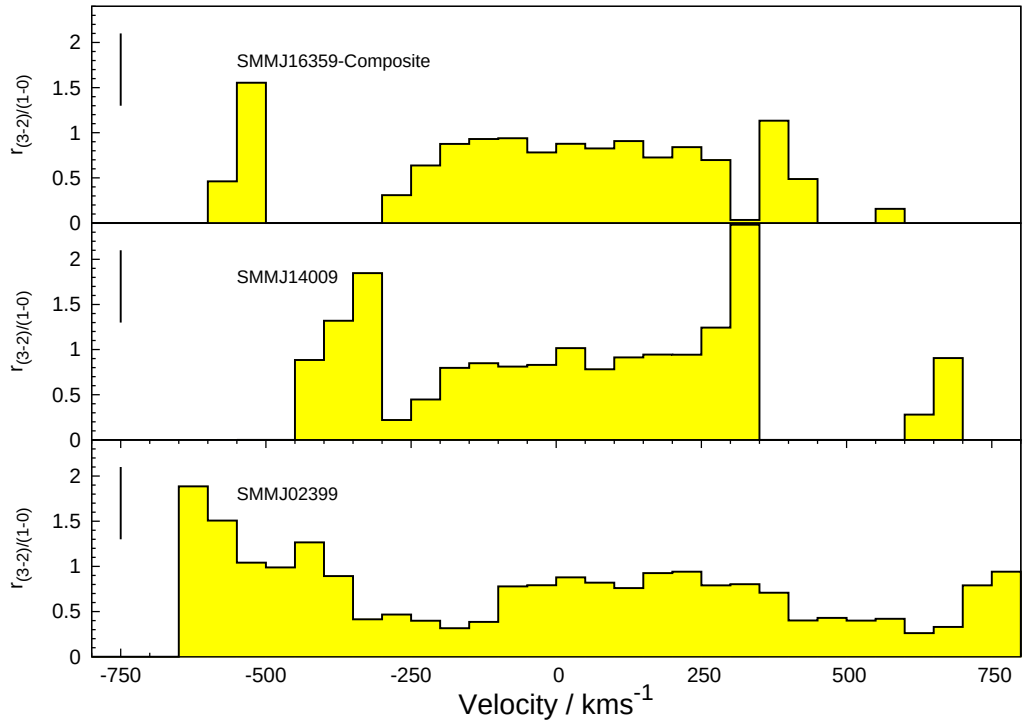

Figure 3.5: *Top – bottom:* Plots of T_b ratio as a function of velocity for the composite SMM J16359 spectrum, SMM J14009 and SMM J02399. Due to poor signal/noise at the extremities of the line profiles, I only consider data within the central $\pm 400\,\mathrm{km\,s^{-1}}$ to be robust enough to draw any conclusions from. The composite spectrum for SMM J16359 is computed by taking the magnification-weighted mean of the individual spectra from images A, B and C of this triply imaged source. The observed velocity offset between ^{12}CO $J = 1-0$ and $J = 3-2$ spectra in SMM J02399 manifests itself as a super-thermal T_b ratios in the envelope of the velocity profile. Typical uncertainties are denoted by the error bar in the top-left of each plot.

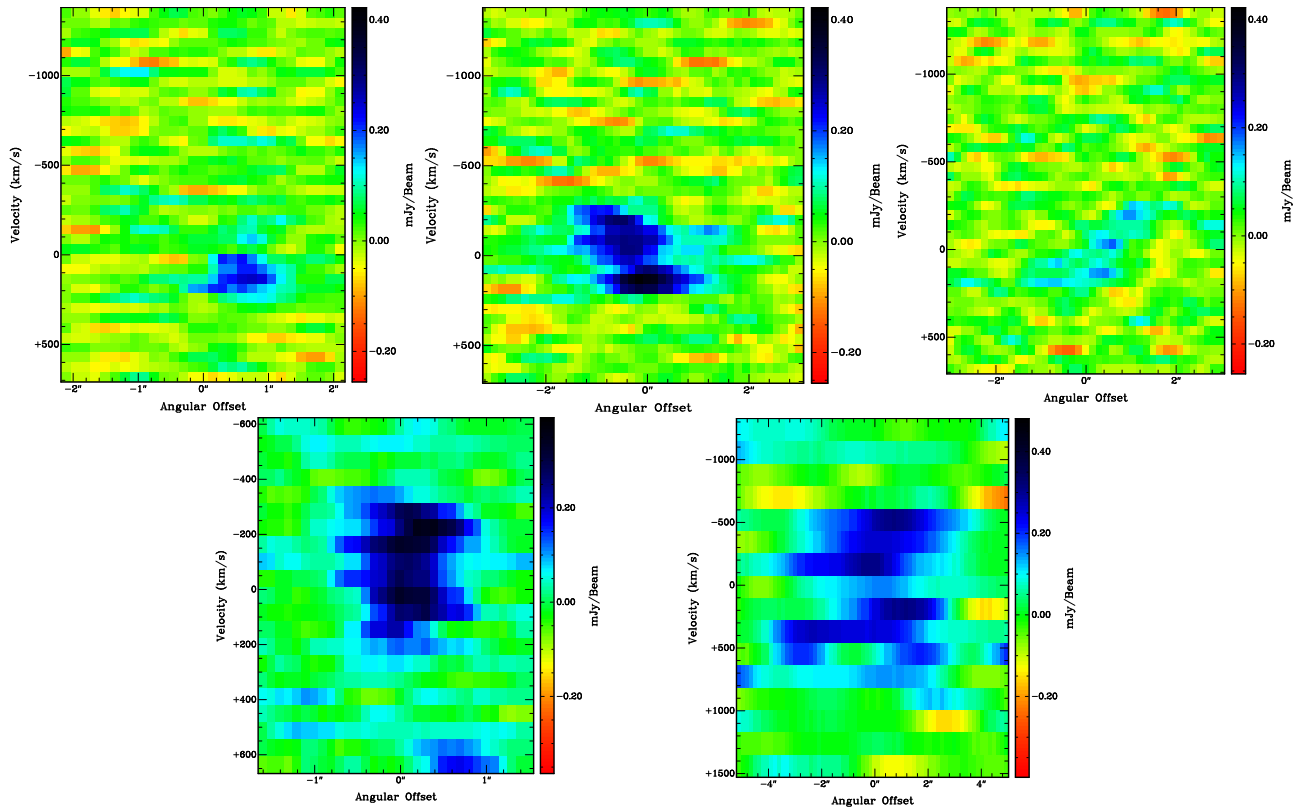

Figure 3.6: *Clockwise from top left:* Position-velocity diagrams for SMM J16359-A, SMM J16359-B, SMM J16359-C, SMM J02399 and SMM J14009.

3.3.4 Infrared-derived star-formation rates

Using the infrared luminosities reported in Table 3.3 with the truncation from Genzel et al. (2003) of the Kennicutt (1998, hereafter K98) conversion factor for a 1–100 $M_\odot$ Salpeter (1955) initial mass function (IMF) to compute SFR_{IR}, we have that:

$$\frac{SFR_{IR}}{1\ M_\odot yr^{-1}} = \frac{L_{IR}}{1.2 \times 10^{10}\,L_\odot} \tag{3.5}$$

In the case of SMM J02399, L_{IR} has been previously thought to arise roughly equally from the AGN and starburst components (e.g. Valiante et al., 2007). Adopting this AGN fraction for both SMM J02399 and SMM J14009, Equation 3.5 yields $SFR_{IR} = 340 \pm 40$ and $670 \pm 70\,M_\odot\,yr^{-1}$, respectively, where the uncertainties are purely statistical (due to L_{IR}), and thus do not include the uncertainty in the K98 conversion factor, nor in the partitioning of L_{IR} in to AGN and star-formation related components.

3.3.5 An independent probe of the SFR via optically-thin free-free emission

The SED longward of the FIR dust bump in galaxies is characterised by three main components: (i) the Rayleigh-Jeans tail of the infrared/sub-mm dust spectrum; (ii) thermalised free-free emission arising from ionised H II regions, which traces the massive/young stars ($> 5\ M_\odot$) capable of photo-ionising; and (iii) synchrotron radiation arising from the electrons accelerated by supernova remnants (Condon, 1992, hereafter C92). Sometimes (iv) synchrotron radiation arising from plasma accelerated by an active AGN may also contribute.

The new high-frequency radio continuum data available for two of the targets in this sample provide the means with which to obtain an independent estimate of the SFR that is free from assumptions about the partitioning of L_{IR} in to AGN and star-formation components.

I determine SFR_{radio} via Equation 3.6, where L_{ff} is the optically-thin free-free luminosity density at frequency ν, defined such that $L = 4\pi d^2 S_{ff}$ for lensing-corrected flux density, S_{ff}. Free-free emission arises in HII regions around short-

Table 3.4: Observed radio properties

Target name	$S_{1.4\,\mathrm{GHz}}$ (μJy)	$S_{5\,\mathrm{GHz}}$ (μJy)	$S_{8\,\mathrm{GHz}}$ (μJy)	$S_{32\,\mathrm{GHz}}$ (μJy)	α
SMM J14009	$529^a \pm 30$	151 ± 17	91 ± 18	42 ± 20	-0.96 ± 0.06
SMM J02399	$526^b \pm 50$	130 ± 22	N/A	57 ± 25	-0.98 ± 0.14

Notes: [a]Ivison et al. (2000); [b]Ivison et al. (1998).

lived, massive stars, and is hence directly related to the SFR (Condon, 1992). The free-free luminosity density is derived by collating the radio continuum data summarised in Table 3.4, and fitting the observed SED for contributions arising from dust (an extrapolation of the Rayleigh-Jeans side of the best-fitting CE01 infrared template), free-free ($S_{\mathrm{ff}} \propto \nu^{-0.1}$: C92) and synchrotron emission ($S_{\mathrm{sync}} \propto \nu^{-\alpha_{\mathrm{sync}}}$). The free parameters in the fit are the flux-scaling of the synchrotron and free-free emission, and also the spectral index, α_{sync}, of the synchrotron component.

$$\left(\frac{L_{\mathrm{ff}}}{\mathrm{W\,Hz^{-1}}}\right) \sim 5.5 \times 10^{20} \left(\frac{\nu}{\mathrm{GHz}}\right)^{-0.1} \left[\frac{\mathrm{SFR}(M \geq 5\,\mathrm{M_\odot})}{\mathrm{M_\odot yr^{-1}}}\right] \tag{3.6}$$

Using the 1.4-, 5- and 8-GHz data available for SMM J14009 and SMM J02399, I measure spectral indices $\alpha = -0.96 \pm 0.06$ and $\alpha = -0.98 \pm 0.14$, respectively (where $S_\nu \propto \nu^\alpha$), a little steeper than the mean value of -0.75 ± 0.06 measured by Ibar et al. (2010) between 610 MHz and 1.4 GHz for 44 radio-detected SMGs in the Lockman Hole, and significantly steeper than the CE01 template that best fits each galaxy's mid-IR-to-submm SED. The error-weighted chi-squared, χ^2 for these fits are 3.08 & 4.55, respectively, significantly better than can be achieved by fitting only dust and synchrotron emission with a fixed $\alpha = -0.8$ and only one degree of freedom (χ^2=430 & 281, respectively). These results highlight the importance of including in the analysis of starburst radio spectra a thermal component which traces *instantaneous* star formation, as opposed to fitting only a synchrotron power law (which traces supernova winds and is expected to lag behind the peak of the starburst activity: Bressan et al., 2002).

The contributions to $S_{32\,\mathrm{GHz}}$ arising due to dust, synchrotron and free-free emission are tabulated in Table 5. I determine $\mathrm{SFR}(M \geq 5\,\mathrm{M_\odot}) = 290 \pm 85\ \mathrm{M_\odot\,yr^{-1}}$ for SMM J14009 and $200 \pm 20\ \mathrm{M_\odot\,yr^{-1}}$ for SMM J02399,

Table 3.5: Radio source derived properties

Target name	$S_{\rm Ka,sync}$ (μJy)	$S_{\rm Ka,dust}$ (μJy)	$S_{\rm Ka,ff}$ (μJy)	$\rm SFR^{\it a}_{radio}$ $\rm M_\odot\,yr^{-1}$	$\rm SFR^{\it a,b}_{IR}$ $\rm M_\odot\,yr^{-1}$
SMM J14009	22 ± 2	8 ± 1	12 ± 5	630 ± 190	670 ± 70
SMM J02399	16 ± 4	18 ± 1	24 ± 6	430 ± 50	340 ± 40

Notes: [a]SFRs calculated for 1-100 $\rm M_\odot$ Salpeter IMF; [b]$\rm SFR_{IR}$ calculated on the assumption that the AGN and star formation contribute equally to $L_{\rm IR}$.

and extrapolate down to 1 $\rm M_\odot$ using a Salpeter (1955) IMF. I find 1–100 $\rm M_\odot$ $\rm SFR_{radio} = 630 \pm 190\ M_\odot\,yr^{-1}$ and $430 \pm 50\ \rm M_\odot\,yr^{-1}$ for SMM J14009 and SMM J02399, respectively. In common with the preceding section, these uncertainties are statistical, and do not reflect the uncertainty in the C92 conversion factor.

3.3.6 The Lyman-break galaxy, Abell 2218 #384

Returning to the observations of SMM J16359, I searched for ^{12}CO $J = 1-0$ in the $z = 2.515$ Lyman-break galaxy (LBG) Abell 2218 #384 at (R.A. 16:35:49.4, Dec. 66:13:07 J2000; Ebbels et al., 1996). The coordinates of this LBG lie within the primary beam of the VLA, centred on SMM J16359-B. I did not detect this source, but set an upper limit to its line flux using $S \leq 3\sigma_n\sqrt{\Delta v \Delta w}$ (Seaquist et al., 1995), where Δv is the velocity resolution of the spectral data cube, $\Delta w \sim 250\,\rm km\,s^{-1}$ is a typical LBG line width (e.g. Greve & Sommer-Larsen, 2008) and the noise in the primary beam-corrected VLA spectrum is σ_n/channel. Deboosting this by $\sim 16\times$ to account for gravitational lensing by the cluster (Ebbels et al., 1996), we thus have upper limits on the ^{12}CO $J = 1-0$ luminosity of $< 8 \times 10^8\,\rm K\,km\,s^{-1}\,pc^2$ and on the gas mass of $< 6 \times 10^8$ $\rm M_\odot$, respectively, where $\alpha_{\rm CO} = 0.8$ has been assumed.

This gas mass limit is comparable to gas masses detected in two similarly high-redshift LBGs by Riechers et al. (2010), who determined $M_{\rm gas} = (9.3 \pm 1.6) \times 10^8\,\rm M_\odot$ and $M_{\rm gas} = (4.6 \pm 1.1) \times 10^8\,\rm M_\odot$ for the same $\alpha_{\rm CO}$, in the Cosmic Eye (at $z = 3.074$) and MS 1512-cB58 (at $z = 2.727$).

3.4 Discussion and conclusions

3.4.1 The physical conditions of the molecular gas

I have presented high-resolution VLA imaging of ^{12}CO $J=1-0$ in three bright, lensed SMGs. Two of these sources harbour known AGN – SMM J14009 and SMM J02399 – and are more luminous ($L_{\rm IR} \sim 10^{13}\,{\rm L}_{\odot}$) than the unlensed sample of Ivison et al. (2011), while the other source – the triply imaged SMM J16359 – is an order of magnitude less luminous ($L_{\rm IR} \sim 6 \times 10^{11}\,{\rm L}_{\odot}$, observed as being equally bright due to the high magnification afforded by its lensing cluster, Abell 2218), and does not appear to be dominated by AGN emission.

Comparing integrated maps of ^{12}CO $J=1-0$ and $J=3-2$ emission, I compute mean brightness temperature ratios of less than unity and velocity width ratios $\sigma_{(3-2)/(1-0)} \geq 1$, both results consistent with the findings of Ivison et al. (2011): SMGs on average experience sub-thermal excitation and exhibit broad ^{12}CO $J=1-0$ line widths.

I derive $L_{\rm IR}$ for the galaxies by collating literature data, and then choosing from the SED library of Chary & Elbaz (2001) the best-fitting template, which I integrate between rest-frame 8–1,000 μm. Next, I computed molecular gas masses via two methods: first by converting $L'_{\rm CO}$ to $M_{\rm gas}$ via $\alpha_{\rm CO} = M({\rm H_2})/L'_{\rm CO(1-0)}$ and then, as an independent check, using an approach that assumes SMGs form stars with Eddington-limited SFE, which gives a lower-limit to the molecular gas mass. For each of the SMGs, the latter method yields a gas mass $\sim 2\times$ lower than that derived via $\alpha_{\rm CO}$.

3.4.2 Independent estimates of the SFR, and the role played by AGN

I compare SFRs derived via two independent diagnostics: (i) ${\rm SFR_{IR}}$, as computed via $L_{\rm IR}$ (K98) and (ii) ${\rm SFR_{radio}}$, computed from $L_{\rm ff}$, the optically-thin free-free luminosity density (C92) (Table 5). Both of these diagnostics are relatively unaffected by interstellar extinction, however the former method is liable to overestimate the SFR if a significant fraction of $L_{\rm IR}$ arises due to heating of dust by an AGN (Murphy et al., 2011). In contrast, the decomposition of the radio SED into dust, synchrotron and free-free contributions provides us with an SFR

diagnostic that is directly related to the photo-ionisation rate of young, massive stars, and is relatively unaffected by AGN.

To derive $\mathrm{SFR_{IR}}$ in § 3.3.4, it was necessary to assume a partitioning of L_{IR} in to star formation and AGN contributions (e.g. Frayer et al., 1998; Greve et al., 2005; Valiante et al., 2007). Here, I use the new measurements of free-free emission to test this assumption. Using Equation 3.5 *without* an AGN correction, SMM J02399's $\mathrm{SFR_{IR,upper}}$ is $670 \pm 70\,\mathrm{M_\odot\,yr^{-1}}$. This is 35 ± 10 per cent higher than $\mathrm{SFR_{radio}}$ for a 1–100-$\mathrm{M_\odot}$ Salpeter IMF, implying a ∼35 per cent contribution to L_{IR} from its hidden AGN. Similarly for SMM J14009, $\mathrm{SFR_{IR,upper}} = 1,340 \pm 140\,\mathrm{M_\odot\,yr^{-1}}$, indicating that some 55 ± 15 per cent of L_{IR} arises due to the AGN.

Recognising that the spatial extent traced by ^{12}CO $J = 1-0$ for each of these galaxies is almost certainly larger than the region in which star formation is actively taking place, we can use these new free-free-derived SFRs to place lower-limits on the global star-formation rate surface density, $\Sigma_{\mathrm{SFR}} = 0.7 \pm 0.1\,\mathrm{M_\odot\,yr^{-1}\,kpc^{-2}}$ for SMM J02399 and $\Sigma_{\mathrm{SFR}} = 450 \pm 200\,\mathrm{M_\odot\,yr^{-1}\,kpc^{-2}}$ for SMM J14009, the former value again attributable to the colossal extent of the ^{12}CO $J = 1-0$ reservoir in SMM J02399. We note that the peak Σ_{SFR} will be significantly higher than these galaxy-averaged values.

At present, these measurements of $\mathrm{SFR_{radio}}$ – and hence estimates of the AGN fraction and Σ_{SFR} – are only as good as the extrapolation of the best-fit SED to the IR/submm data, via which I determine the dust contribution to the $\nu_{\mathrm{rest}} \sim 115$-GHz flux density, itself a relatively low signal-to-noise measurement. However, these uncertainties can be reduced significantly via better sampling of the SED beyond the wavelengths probed by *Herschel*. When complete, the VLA will offer 8 GHz of simultaneous bandwidth across 64 independently tunable sub-band pairs. Together with the Atacama Large Millimeter Array, it will be possible to measure the 350 μm–20 cm SEDs of high-z galaxies with an order of magnitude better sensitivity than currently possible, thus facilitating the search for hidden AGN via the radio spectra of their hosts.

Chapter 4

The Cosmic Eyelash – a "Rosetta Stone" for high-z galaxies

4.1 Introduction

In spite of the intrinsically high luminosities of SMGs, many remain challenging targets for observational studies, due both to photon starvation in the 1 mm atmospheric window – even the brightest SMGs have 850-μm flux densities of only ~ 10 mJy (Ivison et al., 2010c) – and to the typically low angular resolution of the single-dish submillimetre maps in which these sources are first detected. These effects conspire to suppress many examples of this important class of star-forming galaxy below the confusion noise. To alleviate these issues, submillimetre surveys have been devised which exploit the panchromatic flux-boosting effects of gravitational lensing, either by individual line-of-sight foreground galaxies (e.g. Rowan-Robinson et al., 1991; Negrello et al., 2010) or by deliberate exploitation of massive foreground clusters (Smail et al., 1997; Kneib, 2010).

Among the most striking star forming galaxies detected in this manner is "The Cosmic Eyelash" (SMM J21352–0102; hereafter SMM J21352, at J2000 RA 21 : 35 : 11.6, Dec −01 : 02 : 52), first reported by Swinbank et al. (2010b) following a survey of the $z = 0.325$ MACS J2135-01 cluster with the Large Apex Bolometer Camera (LABOCA – Siringo et al., 2009) on the 12-m Atacama Pathfinder EXperiment (APEX) telescope. The high observed flux density of SMM J21352 – $S_{870\mu m} = 106$ mJy – is a result of the $\sim 32.5\times$ magnification provided by the foreground cluster, and corresponds to a de-lensed flux density that is close to

the confusion limit of submillimetre surveys. Its redshift, $z = 2.3259$, derived through blind detection of ^{12}CO $J = 1-0$ with the Zpectrometer instrument on the Robert C. Byrd Green Bank Telescope (GBT) is close to the median redshift of $z \sim 2.5$ of the SMG population (Chapman et al., 2005), suggesting that SMM J21352 may be an intrinsically "typical" SMG, whose lensing properties enhance both the signal-to-noise and angular resolution to the degree necessary to study the detailed interactions between stars and the interstellar medium (ISM) on the scales of individual star-forming regions (giant molecular clouds; GMCs) with the latest radio and millimetre interferometers. This makes SMM J21352 a potential "Rosetta Stone" for the study of high-redshift, dust-enshrouded star-forming galaxies.

Following the detection of SMM J21352 with LABOCA, Swinbank et al. (2010b) conducted a follow-up program of observations with the Submillimeter Array (SMA) at 870-μm, where the 0.3" synthesised beam in the Very Extended (VEX) configuration resolved the emission in to eight distinct clumps over a 4" region, representing four unique dusty clumps of ~ 100 pc size each (in the source plane), mirrored about the critical curve, making them potential analogues at high redshift of the giant molecular clouds (GMCs) in which the bulk of star formation occurs in nearby disk galaxies. These clumps were reported to contain the majority ($\sim 82\%$) of the flux seen in the single-dish LABOCA map.

In this chapter, I present high-resolution interferometric ^{12}CO $J=1$–0 imagery of SMM J21352 obtained with the upgraded Karl G. Jansky Very Large Array (VLA). The resolution of these new data closely match those of the existing SMA map, providing us with the opportunity to investigate the interplay between star formation and molecular gas consumption on GMC scales for the first time in a $z > 2$ galaxy. I also include new C-band, 4–8 GHz radio continuum observations of SMM J21352 obtained with the VLA, within the light of which I re-examine the SMA map, and test both the far-infrared/radio correlation (FIRRC) and star-formation (Schmidt-Kennicutt; SK) law on sub-galactic scales in this star-bursting galaxy.

Throughout the chapter I again use a cosmology with $H_0 = 71\,\mathrm{km\,s^{-1}\,Mpc^{-1}}$, $\Omega_\mathrm{m} = 0.27$ and $\Omega_\Lambda = 0.73$, which gives an angular scale of $8.32/32.5 = 0.26\,\mathrm{kpc\,arcsec^{-1}}$. All flux densities quoted are observed, and all luminosities – unless otherwise stated – are corrected for the 32.5$\times$ amplification.

4.2 Observations and Data Reduction

4.2.1 VLA ^{12}CO $J=1-0$ observations

Observations of redshifted ^{12}CO $J=1$–0 emission in SMM J21352 were carried out using the VLA's new Ka-band receivers in 2–4 hr blocks (totalling 25 h of usable on-source data) in excellent weather conditions between 2010 September – 2011 May. Data were acquired in the DnC (Project ID AI139), CnB (10B-195) and BnA (10C-141) array configurations. During this Open Shared Risk Observing (OSRO) period, the Wideband Interferometric Digital ARchitecture (WIDAR) correlator provided 64×2 MHz dual-polarisation channels in each of two sub-band pairs, corresponding to a velocity resolution of $\sim 15\,\mathrm{km\,s^{-1}}$ channel^{-1} before smoothing.

Antenna pointings were checked hourly using the C-band receivers, and immediately prior to scans of the primary flux calibrator, 3C48. Amplitude and phase corrections as well as the bandpass were determined via short scans of the bright, nearby calibration source J2136+0041 in between each 5 min integration on SMM J21352.

The *uv* coverage of these data are presented in Figure 4.1.

The data were flagged, calibrated and imaged using the standard *AIPS* procedures outlined in Chapter 2, though the data were downloaded in native SMBDF format and loaded into *AIPS* using BDF2AIPS rather than as UVFITS files using FITLD, in order to eliminate any server-side data compression artefacts. Known issues in the setting of delays at the VLA were compensated for in each track using FRING, and 1 min of data towards the end of a good scan of 3C48.

For the DnC observations, the two sub-bands were tuned to 34.62 GHz and 34.73 GHz, such that the redshifted ^{12}CO $J=1-0$ line ($\nu_{\rm rest} = 115.27120256$ GHz – Morton & Noreau, 1994) ought to have been centred in channel 50 of the lower sub-band (AC), with the upper sub-band (BD) tuned to overlap by 10-channels to mitigate the effects of noise in the end channels of each sub-band. The resulting 118 channels provide $2050\,\mathrm{km\,s^{-1}}$ of usable velocity coverage. In fact, spectra from these DnC-only data hinted at a slight redshift discrepancy with respect to the reference GBT redshift, and hence the array tunings for the subsequent CnB and BnA observations were shifted downward in frequency by 40 MHz to accommodate the full width of the line. Thus, the usable spectral coverage

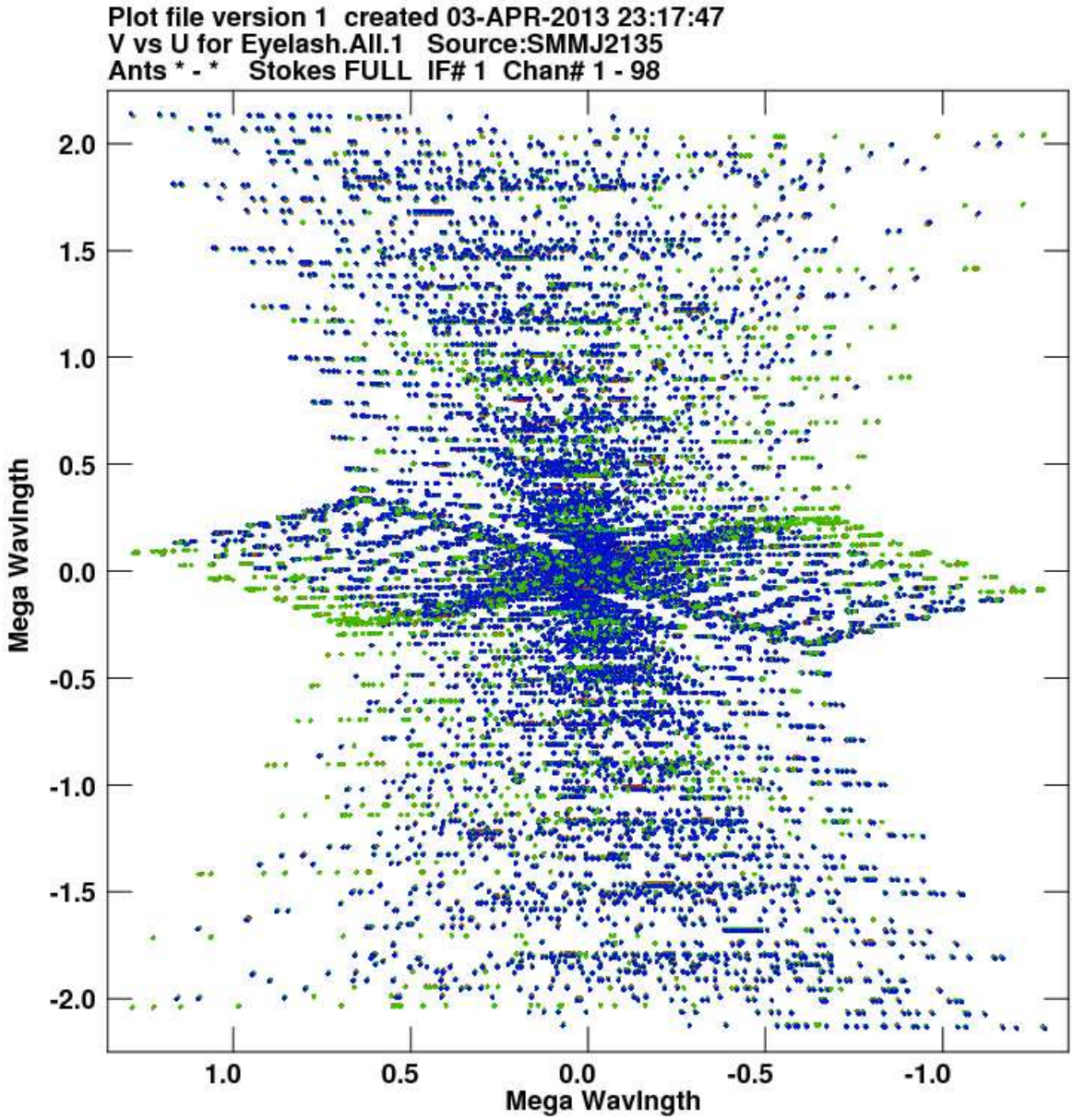

Figure 4.1: *uv* coverage of the visibilities for SMM J21352.

common to all three array configuration is 98 channels, covering 1690 km s^{-1}.

Data for the three array configurations were concatenated together with DBCON, with the REWEIGHT parameter set to provide the optimal 1:4 weighting ratio between adjacent configurations, and so maximise the likelihood of the final data set producing a Gaussian synthesised beam when imaged (Frazer Owen, *private communication*).

A "first order" data cube was quickly made using IMAGR in a non-interactive manner for a square CLEAN box placed around the source, in order to obtain an estimate of the channel width of the ^{12}CO $J = 1-0$ line. An integrated map over these channels was then made, using an interactive CLEAN over a $\sim$ 3-arcmin diameter field with natural weighting (ROBUST 5). I began by placing small, circular clean boxes around only the brightest visible knots of emission and added additional boxes after each major CLEAN cycle, until the network of small clean boxes overlapped across the full extent of the source and all emission lying significantly above the noise had been cleaned. At this point the corresponding clean components were convolved with the synthesised beam to produce the final integrated image. By adopting such cautious interactive cleaning, I hope to have minimised the likelihood of spurious sidelobe structure being interpreted as emission, cleaned and restored to the final map, where it would lead morphological analysis astray.

The data were then binned in to 6 MHz/50 km s^{-1} channels and a science-quality data cube was created. I apply Gaussian *uv* tapers from 50–1000 kλ in steps of 50 kλ to search for any flux which may have been resolved out on long baselines. I find no evidence of significant missing flux – the un-tapered map contains 2.07 ± 0.01 mJy, 95% of the single-dish GBT flux (Danielson et al., 2011) – and thus use this un-tapered map (Figure. 4.4) with synthesised beam 0.28×0.22 arcsec at position angle PA= -50° for all subsequent analysis.

4.2.2 VLA C-band continuum observations

SMM J21352 was observed in the extended A-configuration, in C-band (4–8 GHz) at the VLA during 2011 July 6^{th}–7^{th}, in moderate weather conditions. These observations took place towards the end of the (E)VLA hardware upgrade phase, by which time all 27 antennae had been fitted with functioning C-band receivers, and the WIDAR correlator was tuned to provide 16 sub-bands of 64×2 MHz

Table 4.1: The effect of tapering the SMM J21352 ^{12}CO $J=1-0$ *uv* data

Taper (kλ)	Synthesised beam (arcsec)	Peak flux (mJy)	Noise (μJy/beam)	Total flux (BLSUM; mJy)
50	3.17×2.48 at PA= 2.07°	1.171	52	1.9879
100	1.80×1.38 at PA= −1.39°	0.778	32	2.1012
150	1.23×0.98 at PA= −4.96°	0.574	26	2.0537
200	0.95×0.78 at PA= −8.75°	0.453	23	1.9524
250	0.78×0.65 at PA= −12.42°	0.372	21	2.1683
300	0.67×0.57 at PA= −16.06°	0.311	20	2.1701
350	0.59×0.51 at PA= −19.60°	0.267	19	2.2000
400	0.54×0.47 at PA= −22.89°	0.234	19	2.0956
450	0.49×0.43 at PA= −27.10°	0.210	18	1.9325
500	0.46×0.40 at PA= −29.76°	0.189	18	2.0838
550	0.44×0.38 at PA= −32.89°	0.174	17	2.1771
600	0.42×0.36 at PA= −34.32°	0.164	17	2.2986
650	0.40×0.34 at PA= −37.50°	0.156	17	1.9854
700	0.39×0.33 at PA= −38.02°	0.149	16	2.0623
800	0.37×0.30 at PA= −41.45°	0.139	16	2.3285
900	0.35×0.30 at PA= −40.89°	0.132	16	2.1403
1000	0.34×0.28 at PA= −44.75°	0.127	16	2.2359
Un-tapered	0.28×0.21 at PA=−49.11°	0.100	14	2.2512

Synthesised beams resulting from applying Gaussian *uv* tapers, with the corresponding map peak flux, noise and integrated flux. Since there is no compelling evidence of "missing flux" on longer baselines, I use the untapered data for all subsequent analysis.

channels each, yielding a total instantaneous bandwidth of 2 GHz. By splitting the observing time between observations at 4–6 and 6–8 GHz, a moderately large spectral region of the radio continuum emission in SMM J21352 could be studied.

From a total time allocation of 10 h, 8 h of usable on-source data were obtained, with flux calibration being set via scans of 3C48 at the end of each track, and antenna pointing, amplitude and phase tracking and bandpass correction being determined via frequent, short scans of the nearby calibrator J2136+0041.

These data were reduced and imaged in CASA by Frazer Owen, who kindly made the total intensity map (with synthesised beam 0.34×0.29-arcsec at PA= 180° and an rms sensitivity of $1.45\,\mu\mathrm{Jy\,beam^{-1}}$) and spectral index map available to me.

4.2.3 IRAM PdBI mid-J ^{12}CO observations

I use data obtained with the six-element IRAM Plateau de Bure Interferometer (PdBI) to observe the mid-J ^{12}CO emission. Using 4 and 2 hr on-source exposures in D-configuration, taken in Directors Discretionary Time (DDT) during 2009 May, maps were created of ^{12}CO $J = 3-2$ and $J = 4-3$ emission respectively, reaching S/N$\sim$ 300 across $900\,\mathrm{km\,s^{-1}}$ in each map. The total line fluxes are $(13.20 \pm 0.10)\,\mathrm{Jy\,km\,s^{-1}}$ and $(17.3 \pm .1.2)\,\mathrm{Jy\,km\,s^{-1}}$ for $J = 3-2$ and $J = 4-3$ respectively, and the corresponding synthesised beams are 2.11×1.59-arcsec at PA= 37° and 1.08×0.50-arcsec at PA= 23°. These maps were first presented in Danielson et al. (2011), where details of the data reduction, and the source-averaged spectra are also presented.

^{12}CO $J=6-5$ emission was observed in A configuration during 2010 January (see Swinbank et al., 2011; Danielson et al., 2011). The six hours of usable on-source integration time in this configuration yield a synthesised beam of 0.67×0.43 arcsec, at PA= 24.5° and a velocity-integrated flux of $(21.5 \pm 1.1)\,\mathrm{Jy\,km\,s^{-1}}$.

4.2.4 Submillimeter array observations

A program to map the rest-frame far-infrared continuum emission from SMM J21352 was carried out at the Submillimeter Array (SMA) in 2009 May – September (Swinbank et al., 2010b, in which a description of the data reduction is presented). With the lower sub-band tuned to 870-μm, a total of 5.5 h of on-source data were

obtained in the sub-compact (SC) configuration, with 12 h in compact (C), 2 h in extended (Ext) and 6 h in the very extended (VEX) configuration.

In order to maximise the resolution of their continuum map, Swinbank et al. (2010b) used only the 6 h of VEX-configuration *uv* data, in which the 0.3-arcsec synthesised beam appears to reveal eight image-plane clumps (four source-plane clumps, each mirrored about the critical curve). The upper sub-band was tuned to search for redshifted ^{12}CO $J=10-9$ emission – this line was not detected, but a formal 3σ upper-limit of $\leq 0.2\,\mathrm{Jy\,km\,s^{-1}}$ was determined.

The calibrated *uv* data from this program of observations were kindly made available to me (S. Longmore, *private communication*), from which I made a new continuum map incorporating all the data – suitably weighted to maximise resolution while including a reasonable number of short baselines. The synthesised beam of this updated map is 0.59×0.45-arcsec at PA$= 50^{\circ}$ – a little coarser than the VEX-only map, but with less sidelobe structure in the dirty image, and with an rms sensitivity of 1.58 mJy/beam. The motivation for revisiting these *uv* data and the morphological implications of the new map are further discussed in Section 4.3.1.

4.3 Analysis and results

4.3.1 Source morphology and spectrum

^{12}CO $J=1-0$

The multi-J source-averaged ^{12}CO properties are summarised in Table 4.2. SMM J21352 is detected in ^{12}CO $J=1-0$ with a peak flux in the velocity-integrated image of 8σ, where $\sigma = 14\,\mu$Jy, at a flux-weighted redshift of 2.3268 ± 0.0001. The uncertainty in this redshift corresponds to velocity uncertainties of the order ΔV$\sim 10\mathrm{km\,s^{-1}}$. In the spectrum extracted from the data cube, we see a broad line of FWZI $= 920\mathrm{km\,s^{-1}}$, and good agreement with that of the ^{12}CO $J=3-2$ line.

I extracted a spectrum from the ^{12}CO $J=1$–0 data cube using the $\mathcal{AIPS}$ task BLSUM, which sums the flux density at each plane in the cube within a polygonal area, and produced an error spectrum using RSPEC, for a suitably large off-source portion of the image. The typical noise in each spectral channel is $51\,\mu\mathrm{Jy\,beam^{-1}}$.

Comparing the ^{12}CO maps (Figure 4.4) and the $J = 1-0$ and $J = 3-2$ spectra (Figure 4.5), we find good agreement in both the astrometry (within the uncertainties of the large PdBI beam) and the overall line shape. The peak $J=1-0$ flux density of ~ 7 mJy is slightly higher than the peak flux density in the reference GBT spectrum, yet the velocity integrated flux is within 5% of the total single-dish flux seen by Danielson et al. (2011). I attribute the differences in line shapes between the GBT and VLA $J=1-0$ line profiles to the superior velocity resolution of the VLA data cube (6 MHz/channel for the averaging I have applied, *cf.* ∼20 MHz for GBT; Harris et al., 2010), and note that the new $J=1-0$ spectrum is in better agreement with the shape of the PdBI spectra. The overall velocity line-width ratio derived by fitting a single Gaussian to the $J=1-0$ and $J=3-2$ spectra is $\sigma_{(1-0)/(3-2)} = 0.88 \pm 0.02$, which is significantly lower than values reported previously for SMGs (e.g. Ivison et al., 2011; Riechers et al., 2011a; Thomson et al., 2012), but is probably biased low by the "peakiness' of the $J=1-0$ spectrum, to which a single Gaussian fit is inappropriate (Figure 4.5).

In fact, Danielson et al. (2011) find that the PdBI spectra are better-fit by a trio of Gaussian components, whose superposition we observe in the source-averaged spectrum. We see a similarly complicated line profile in the latest VLA $J=1-0$ spectrum (Figure 4.5), and I fit three Gaussians – representing a possible interacting system – over the FWZI= 920km s^{-1} of the line. The best fitting combination of Gaussians has $\chi^2 = 2.23$ for the nine degrees of freedom (three centroids, maxima and full-width at half maximums; listed in Table 4.3). We see no evidence in this integrated spectrum that the bluest of these components is double-horned (*cf.* Danielson et al., 2011), but cannot definitively rule out this possibility due to the conservative frequency binning adopted in an effort to maximise signal-to-noise.

Far-infrared morphology

Comparison of the legacy VEX SMA map from Swinbank et al. (2010b) to the latest VLA ^{12}CO $J=1-0$ and C-band continuum maps (Fig. 4.3) reveals an offset between the strongest areas of infrared and radio emission in SMM J21352, and an apparent anti-correlation between the sites of strongest gas and dust emission. Given the omnipresence of the observed far infrared/radio correlation in star-

forming systems across several orders of magnitude in luminosity (e.g. Ivison et al., 2010a), I treat this result with considerable skepticism. To investigate this further, the calibrated *uv* data for the SMA observations of SMM J21352 were made available to me (S. Longmore, *private communication*). I imported these data in to $\mathcal{AIPS}$ so that they may be re-imaged in a manner consistent with the ^{12}CO $J=1-0$ and VLA C-band continuum imaging.

Imaging only the VEX data, placing CLEAN boxes around the central sliver of emission and running IMAGR in a typical non-interactive manner, I recover structure that is similar to that seen in the canonical map of Swinbank et al. (2010b). However, inspection of both the synthesised beam profile and the dirty image reveal two striking limitations to the data, the treatment of which necessitate caution in our subsequent interpretation of the maps: (i) the synthesised beam is non-Gaussian and has considerable sidelobes, and (ii) the signal-to-noise of the map is poor, with high phase noise (Fig. 4.2). Together, these effects conspire to complicate the mathematical de-convolution of the "true" intensity distribution I_ν and the dirty beam B (Equation 2.6). This in turn implies that some of the structure seen in the original map may well be spurious, the result of random noise peaks and interferometer sidelobe emission having been cleaned, stored, and restored to the final map due to the chosen CLEAN boxes and lack of short interferometer baselines.

With the benefit of additional visibilities from the SC, C and Ext configurations, I now have the opportunity to include more short-baseline visibilities, boosting the signal/noise of the data and lowering the level of the dirty beam sidelobes (albeit at the expense of some resolving power, as we are in effect lowering the weighting of the long VEX baselines), and so re-examine the apparently clumpy structure of SMM J21352.

I do this by creating three versions of the multi-configuration concatenated SMA *uv* data using DBCON, and applying three distinct data weighting schemes (controlled by REWEIGHT):

1. All data concatenated with no "tweaking" of the weights between long/short baselines (REWEIGHT 1 1). Due to the number of hours of data obtained in each configuration, this dataset is weighted slightly towards short baselines.

2. Data concatenated with REWEIGHT tweaked to up-weight short baselines, in such a manner as to minimise the sidelobe level, at the expense of resolution.

3. Data concatenated with REWEIGHT tweaked to up-weight long baselines (but still with the inclusion of previously omitted short baselines) in such a manner as to maximise the resolution at the expense of increased sidelobe structure.

From each of these concatenated *uv* datasets, I create maps with hybrid weighting (ROBUST = 1.5), and apply a series of Gaussian *uv* tapers from 100–1000 kλ in steps of 100 kλ, to search for missing flux on longer baselines.

I find that weighting scheme 3 (all data added together, with the long baselines up-weighted) provides the best compromise between achieving the good resolution and signal to noise, and having the least incongruous sidelobes. This optimal weighting produces a synthesised beam of 0.59 × 0.45-arcsec at PA= 50° (*cf.* 0.38×0.26-arcsec at PA= 43° in the VEX only map), and the map has a noise level of 1.4 mJy beam^{-1}. The integrated 870-μm flux density $S_{870-\mu\mathrm{m}} = 91 \pm 5$ mJy, recovering 85% of that seen in the single-dish LABOCA map Swinbank et al. (2010b). A comparison between the VEX-only map and the new, optimally-weighted map is presented in Figures 4.2 and 4.3.

4.3.2 Line luminosity and total gas mass

Molecular gas mass estimates in distant galaxies are frequently undermined by two main sources of uncertainty: (i) where only mid-J ^{12}CO lines have been observed, reliance on an assumed underlying T_b distribution to convert the observed ^{12}CO line intensity to that of ^{12}CO $J = 1-0$– on which α_CO is calibrated – introduces uncertainties of a factor $\sim 2\times$, and (ii) uncertainties in the α_CO luminosity-to-gas-mass conversion factor itself, which varies by up to an order of magnitude between the optically-thick, dense, bound environments of Milky Way GMCs (where $\alpha_\mathrm{CO} = 5$ M$_\odot$ (K km s^{-1} pc^2)$^{-1}$) and the more extended, dynamically turbulent and morphologically smooth ISM of ULIRGs (where $\alpha_\mathrm{CO} = 0.8$ M$_\odot$ (K km s^{-1} pc^2)$^{-1}$ is typically adopted). While our new ^{12}CO J=1–0 maps allow us to bypass the first source of uncertainty, uncertainties due to α_CO itself remain.

Line fluxes are determined by integrating across the FWZI of each line, and checked via the equivalent integrated image. I measure a ^{12}CO $J = 1-0$ flux density of 2.25 ± 0.23 mJy across 920 km s^{-1} , recovering $\sim 95\%$ of the single-dish

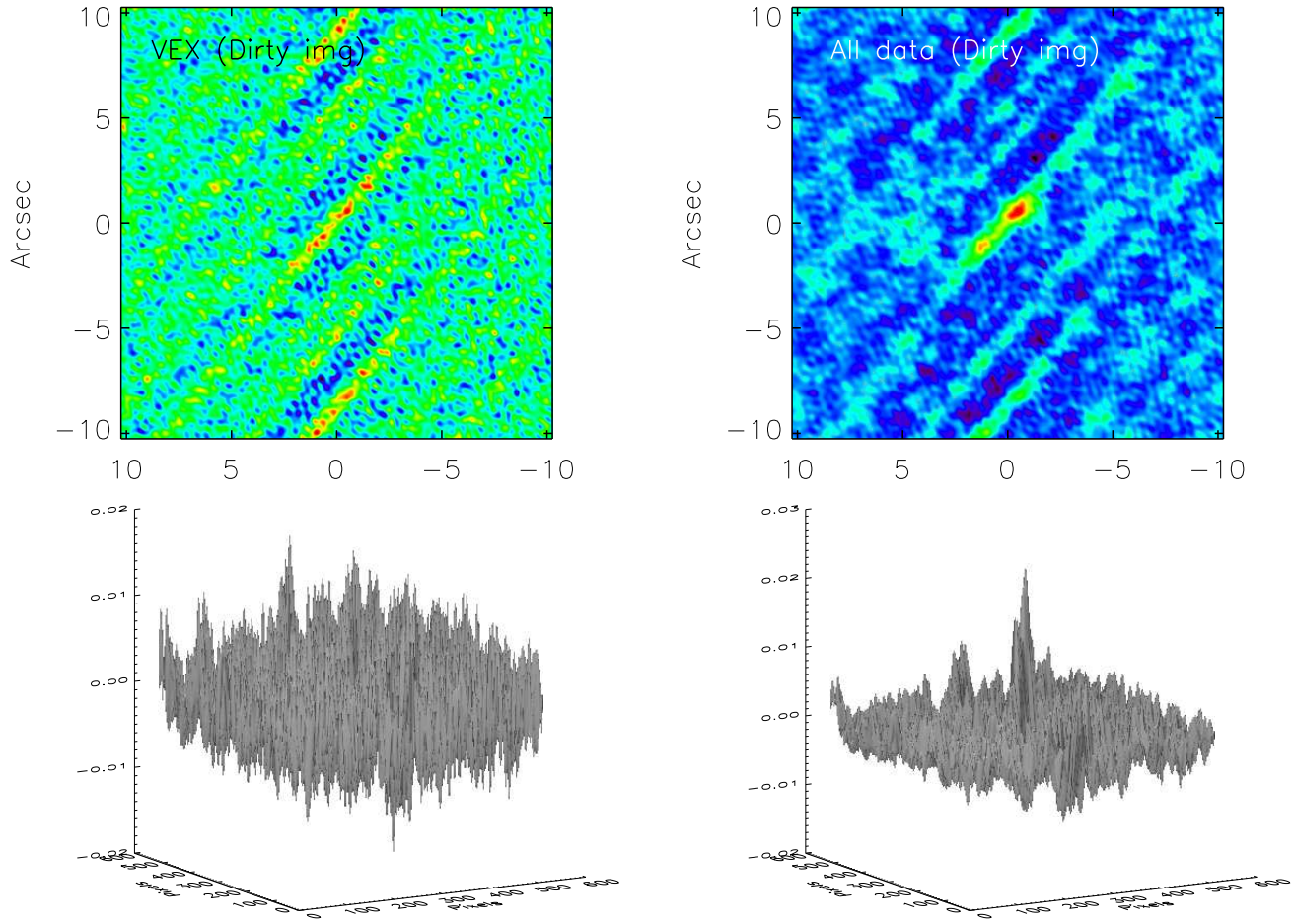

Figure 4.2: SMA 870-μm dirty images. *Top-left:* SMA heat map of the VEX-only dirty image. *Top right:* dirty image from all SMA 870-μm visibilities, optimally weighted to lower sidelobe structure while retaining as much resolution as possible. *Bottom-left:* Surface plot of the VEX-only dirty image, highlighting the low signal-to-noise of these data prior to cleaning and the corresponding likelihood of picking up spurious peaks as sources of real emission. *Bottom-right:* Surface plot of the dirty image made using all data. By including data from the more compact configurations, I broaden the synthesised beam, losing outright resolution. However in doing so, we gain confidence that the emission we clean and pass to the final clean map is real.

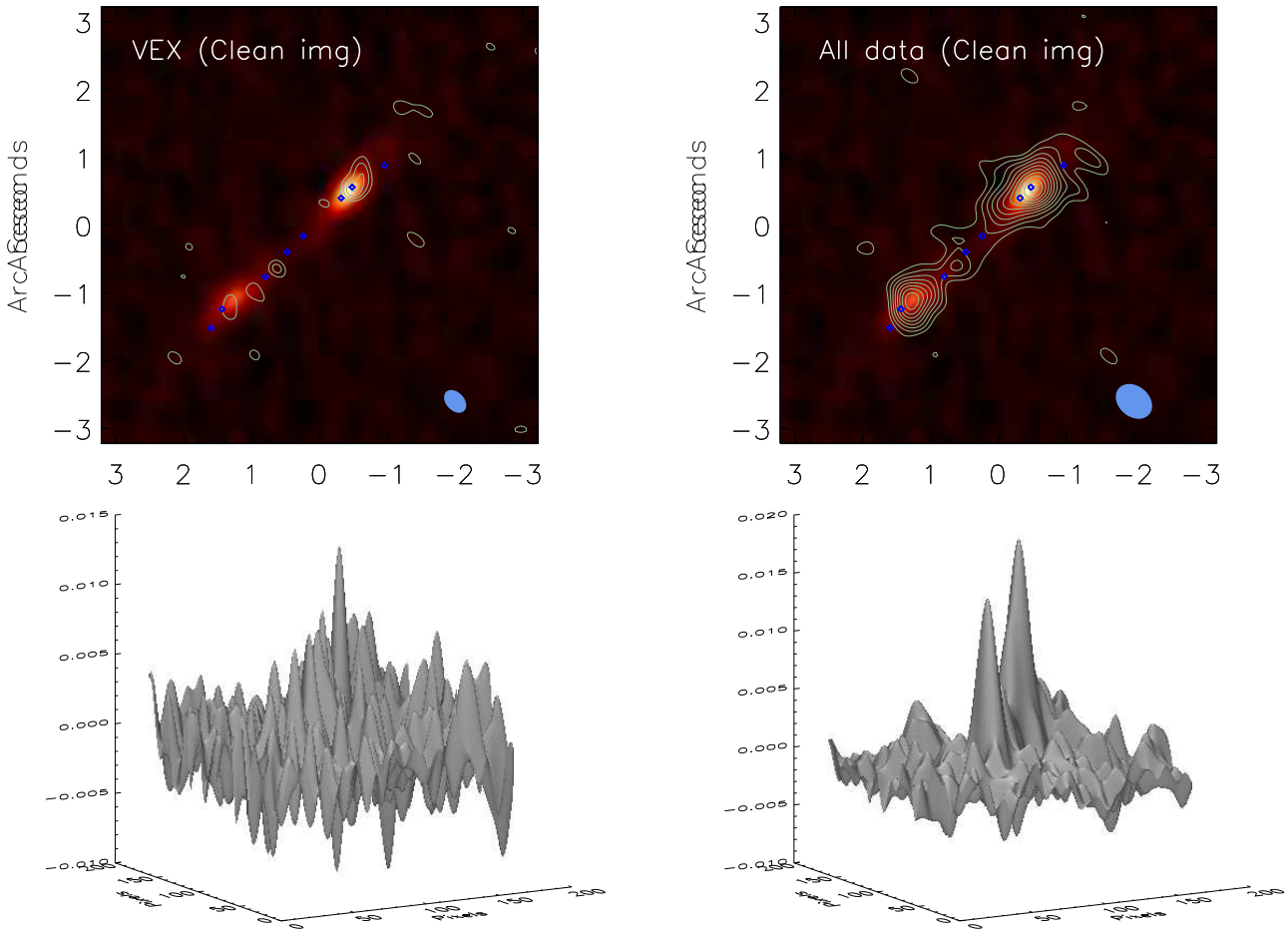

Figure 4.3: SMA 870-μm clean images set on top of heat maps of the new VLA 4–8 GHz continuum data, and with the coordinates of the gas clumps identified in ^{12}CO $J = 1-0$ shown (Section 4.3.3) *Top-left:* Contours from the VEX-only SMA data. The synthesised beam for this map (0.38×0.26-arcsec at PA= 43°) is very close to that of the new 4–8 GHz radio image (0.34×0.29-arcsec at PA= 180°), yet we see clumpy structure in the far-infrared map for which there is no corresponding structure in the radio, and an apparent anti-correlation between gas and dust, as traced via ^{12}CO $J=1-0$. *Top right:* Map made with all SMA 870-μm visibilities, combined and optimally weighted to minimise sidelobes while still achieving good angular resolution (0.59×0.45-arcsec at PA= 50°). This map is congruent with the high-resolution radio map, and contains the ^{12}CO $J=1-0$ clumps within the far infrared-bright regions of the map. Contours are at -3, 3, 4, 5, 6...$\times\sigma$, where $\sigma = 1.58$ mJy beam^{-1}. *Bottom-left:* Surface plot of the noisy VEX-only clean image. *Bottom-right:* Surface plot of the clean image made using all data, demonstrating the gains to be made in terms of signal-to-noise by including additional short baselines.

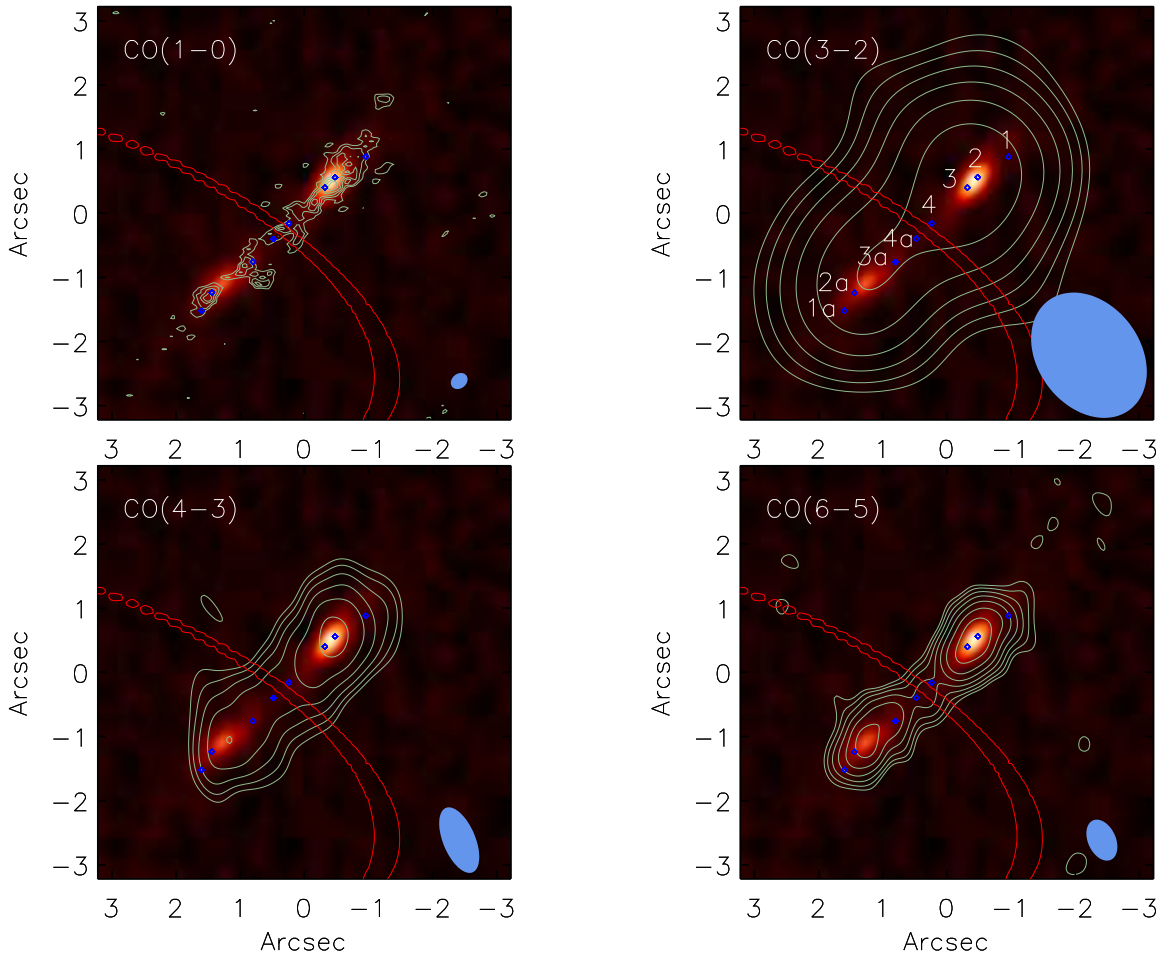

Figure 4.4: Velocity-integrated maps of the four observed ^{12}CO transitions in SMM J21352, on which are marked (in blue) the positions of the kinematically and spatially distinct clumps identified from the ^{12}CO $J=1$–0 data cube (Section 4.3.3). Each of the clumps to the North-West of the critical line has a fainter counterpart to the South-East. *Top-left:* VLA ^{12}CO $J=1-0$ contours, spaced at -3, 3, 4, 5...$\times\sigma$ for $\sigma = 14\,\mu$Jy beam^{-1}. *Top-right:* IRAM PdBI ^{12}CO $J=3-2$ contours, at -3, 3, $\sqrt{2}\times 3\times\sigma$ (and in steps of $\sqrt{2}\times\sigma$ thereafter) for $\sigma = 0.24$ mJy beam^{-1}. *Bottom-left* and *Bottom-right*: IRAM PdBI contour maps of ^{12}CO $J=4-3$ and $J=6-5$ emission, with contours spaced at $\sqrt{2}\times\sigma$ intervals starting at 3σ, where $\sigma = 0.20$ mJy beam^{-1} and $\sigma = 0.29$ mJy beam^{-1}, respectively. In all cases, the underlying heat map is the new VLA 4–8 GHz continuum map, the red curve represents the critical line from the lensing model (Swinbank et al., 2011) and the beam shown in the bottom-right of each sub-plot is that corresponding to the relevant ^{12}CO emission. The naming convention of the clumps is shown only on the $J=3-2$ sub-figure for clarity.

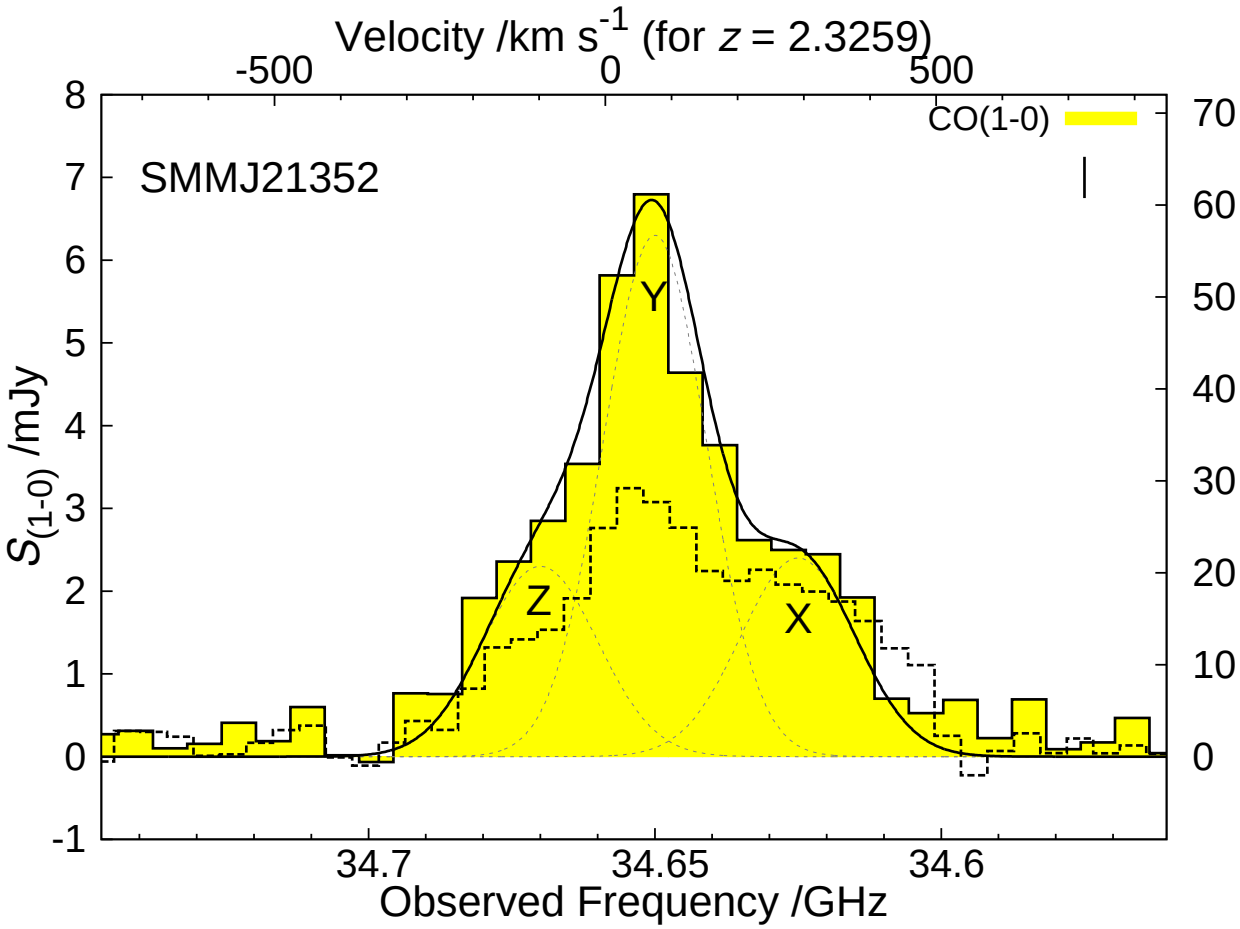

Figure 4.5: SMM J21352 ^{12}CO $J = 1-0$ and $J = 3-2$ spectra. The latter is scaled vertically by a factor 9^{-1} so as to lie on the same T_b scale. The velocity scale is quoted with respect to the GBT redshift, and a typical 50 μJy error bar is shown in the top-right of the plot. The shapes of the two line profiles are in mutual agreement. The new $J = 1-0$ line profile contains 95% of the flux of the GBT Zpectrometer measurement (Danielson et al., 2011) but has a markedly different line profile, which I attribute to the superior velocity resolution of the VLA's new Ka-band receivers relative to the coarser bins of Zpectrometer. We see evidence that the ^{12}CO $J=1$–0 spectrum contains emission from three kinematic components, which I model via a trio of Gaussians X, Y and Z, over-plotted with a faint grey dotted line. This analysis agrees with the kinematic analysis of Danielson et al. (2011), though I see no evidence in this integrated spectrum that the bluest of these components is double-peaked.

GBT flux measurement. Combining this result with the $J=3-2$ PdBI spectrum, the brightness temperature ratio is $r_{(3-2)/(1-0)} = 0.71 \pm 0.07$, in line with the typical brightness temperature ratios of SMGs $r_{(3-2)/(1-0)} < 1$, which once again points to the presence of an additional, low-excitation gas component, undetected and undetectable by mid-J-only ^{12}CO studies.

The intrinsic (i.e. de-lensed) ^{12}CO $J=1-0$ line luminosity is given by

$$L'_{\mathrm{CO}(1-0)} = \frac{3.25\times10^{7}}{\mu}\left[\frac{D_{\mathrm{L}}^{2}(\mathrm{Mpc})}{1+z}\right]\left(\frac{\nu_{\mathrm{rest}}}{\mathrm{GHz}}\right)^{-2} \times\left[\frac{\int_{\Delta V} S_{\nu}d\nu}{\mathrm{Jy\,km\,s^{-1}\,pc^{2}}}\right]\mathrm{K\,km\,s^{-1}\,pc^{2}} \tag{4.1}$$

where μ is the average magnification of the source, D_{L} is the luminosity distance (Mpc), ν_{rest} is the rest-frame central frequency of the line ($= 115.27120256\,\mathrm{GHz}$) and $\int_{\Delta V} S_{\nu}d\nu$ is the velocity-integrated line intensity.

I begin my interpretation of the latest ^{12}CO $J=1-0$ data by deriving upper and lower plausible limits to the total gas mass in SMM J21352, invoking two diametrically opposed assumptions:

1. That the gas is optically thin, and of Solar metallicity ($[\mathrm{CO/H_2}]\sim 10^{-4}$), such that

$$\frac{M(\mathrm{H_2})}{L'_{\mathrm{CO}(1-0)}} \sim 0.08\left[\frac{g_1}{Z}e^{-T_0/T_{\mathrm{k}}}\left(\frac{J(T_{\mathrm{k}})-J(T_{\mathrm{CMB}})}{J(T_{\mathrm{k}})}\right)\right]^{-1} \times\left(\frac{[\mathrm{CO/H_2}]}{10^{-4}}\right)^{-1}\frac{\mathrm{M_{\odot}}}{\mathrm{K\,km\,s^{-1}\,pc^{-2}}} \tag{4.2}$$

   with $T_0 \sim 5.5\,\mathrm{K}$ being the minimum temperature necessary to move ^{12}CO to its first rotational excited state, $J(T) = T_0(e^{T_0/T}-1)^{-1}$, $T_{\mathrm{CMB}} \sim 9.08\,\mathrm{K}$ (the CMB temperature at $z = 2.3259$), $g_1 = 3$ is the degeneracy of the first rotational excited state and $Z \sim 2(T_{\mathrm{k}}/T_0)$ is the partition function. For a kinetic temperature $T_{\mathrm{k\,min}} = 40\,\mathrm{K}$, an appropriate lower-limit for star-forming gas, this corresponds to a lower-limit on α_{CO} of 0.54.

For an intrinsic (i.e. de-lensed) $L'_{\rm CO(1-0)} = (1.34 \pm 0.13) \times 10^{10}\,{\rm K\,km\,s^{-1}\,pc^2}$, this corresponds to a firm lower-limit to the molecular gas mass of $M_{\rm gas,min} > 9.1 \times 10^9\,{\rm M_\odot}$.

2. That the mass budget of SMM J21352 is dominated by gas, with negligible contributions from stars or dark matter, in which case the dynamical mass provides an upper limit to the gas mass. If the ^{12}CO $J = 1-0$ emission traces an isotropic, virialised sphere, then the dynamical mass $M_{\rm dyn} = 5R\sigma^2_{\rm CO(1-0)}/G$ (Tacconi et al., 2008). If the gas traces a region $\sim 2\,$kpc in radius (Swinbank et al., 2011), then this implies an average $\alpha_{\rm CO} < 4$ and $M_{\rm gas} < 6.8 \times 10^{10}\,{\rm M_\odot}$. For a rotating disk model, both $\sigma_{\rm CO(1-0)}$ and R need to be corrected for the inclination angle, $\sin i$. By performing simulations in which the dynamics of multiple disk galaxies are modelled over a range of inclination angles, Neri et al. (2003) find that this lowers the dynamical mass for a given R and $\sigma_{\rm CO(1-0)}$ to $\sim 2.1R\sigma^2_{\rm CO(1-0)}/G$, hence $\alpha_{\rm CO} < 1.7$ and $M_{\rm gas} < 2.9 \times 10^{10}\,{\rm M_\odot}$.

4.3.3 Spatially resolved properties

The combined effects of the 0.3-arcsecond beam of the latest VLA A-configuration ^{12}CO $J=1-0$ map and the 32.5× magnification experienced by SMM J21352 put us in the tantalising position of being able to – for the first time – spatially resolve ISM emission in a $z \sim 2.5$ star-forming galaxy down to $\sim 130\,$pc scales, comparable to the sizes of giant molecular clouds, the sites of active star formation in the local Universe. It is with this ultimate aim in mind that I attempt to identify sub-structures in the $J = 1-0$ data cube, which I identify via two independent methods. Only those sub-structures detected via both methods are taken as "real" in the subsequent analysis. First, I use the $\mathcal{AIPS}$ task SERCH, which employs the "matched filter analysis" technique outlined by Uson et al. (1991), and examines a data cube, attempting to fit Gaussian line profiles of user-specified channel width to each pixel in the image plane. Employing a 4σ cut and searching for lines between 50–950km s^{-1} (in steps of 200km s^{-1}), I identify four bright clumps above the critical curve (numbered 1–4 from top-right to bottom-left), and select their four most likely counterparts on the fainter mirror image on the opposite side of the critical curve.

Table 4.2: SMM J21352 observed molecular line properties

^{12}CO transition	$\nu^a_{\rm rest}$ (GHz)	$I^b_{\rm CO}$ (Jy km s^{-1})	$L'^c_{\rm CO}$ ($\times 10^9$ K km s^{-1} pc^2)	σ (km s^{-1})	FWZI (km s^{-1})	$z_{\rm CO}$
$J=1-0$	115.27120256	2.07 ± 0.01	16.8 ± 0.2	170 ± 1	920	2.3267 ± 0.0001
$J=3-2$	345.79599131	13.20 ± 0.10	11.8 ± 0.1	190 ± 5	880	2.3273 ± 0.0001
$J=4-3$	461.04076975	17.3 ± 1.2	8.7 ± 0.6	200 ± 5	920	2.3272 ± 0.0001
$J=6-5$	806.6518028	21.5 ± 1.1	6.0 ± 0.3	200 ± 5	900	2.3274 ± 0.0001

Notes: [a]Morton & Noreau (1994); [b]Observed; [c]Lensing corrected.

Table 4.3: SMM J21352 kinematic parameters

Component	Peak (mJy)	v ($\mathrm{km\,s^{-1}}$)	σ ($\mathrm{km\,s^{-1}}$)
X	2.4	$+291 \pm 31$	85 ± 27
Y	6.3	$+75 \pm 29$	23 ± 25
Z	2.3	-98 ± 32	87 ± 28

Notes: Best-fitting coefficients for the triple-Gaussian fit to the observed ^{12}CO $J=1-0$ line, with $\chi^2 = 2.23$. Velocities are quoted with respect to the reference redshift of $z = 2.3259$, and uncertainties in the velocities are calculated by adding the statistical errors of the fit and the half-channel width in quadrature.

The robustness of these clumps is verified by performing a blind search for clumps using the IDL clump-finding algorithm of Williams et al. (1994)[1], which contours the data cube at 3σ (where σ is the typical rms per spectral channel, $\sim 50\,\mu\mathrm{Jy\,beam^{-1}}$) to identify peaks, and then attempts to follow the surrounding emission through adjacent telescope beams until its extended structure attenuates below the noise threshold or blends with neighbouring clumps. There are no prior kinematic constraints imposed on the clumps, though the FWHM is computed as the algorithm examines the cube. This algorithm reports 18 possible clumps in total, the brightest four of which agree positionally to within $\pm 0.6\times$ the synthesised beam in RA and Dec with the four Northern clumps identified via SERCH, and we find four likely counterparts on the other side of the critical curve, within the same positional uncertainty.

The ^{12}CO line intensities I_{CO} of each of the clumps are determined by summing the flux contained within a number of pixels equivalent to the beam area centred on the clump, and multiplying by the FWZI of the respective $J=1-0$ line profile (Figure 4.6). The corresponding luminosities are then determined via Equation 4.1 in the usual manner.

Though I do find clumps in the gas equal in number to those found in the dust via the SMA VEX map of Swinbank et al. (2010b), the positioning of the clumps within the two maps differ by more than one full telescope beam indicating either a real anti-correlation between the distributions of gas and dust in SMM J21352, or alternatively providing further evidence of the need to re-examine the SMA visibilities.

I hereafter treat the locations of the gas over-densities as identified above as

[1] http://www.ifa.hawaii.edu/users/jpw/clumpfind.shtml

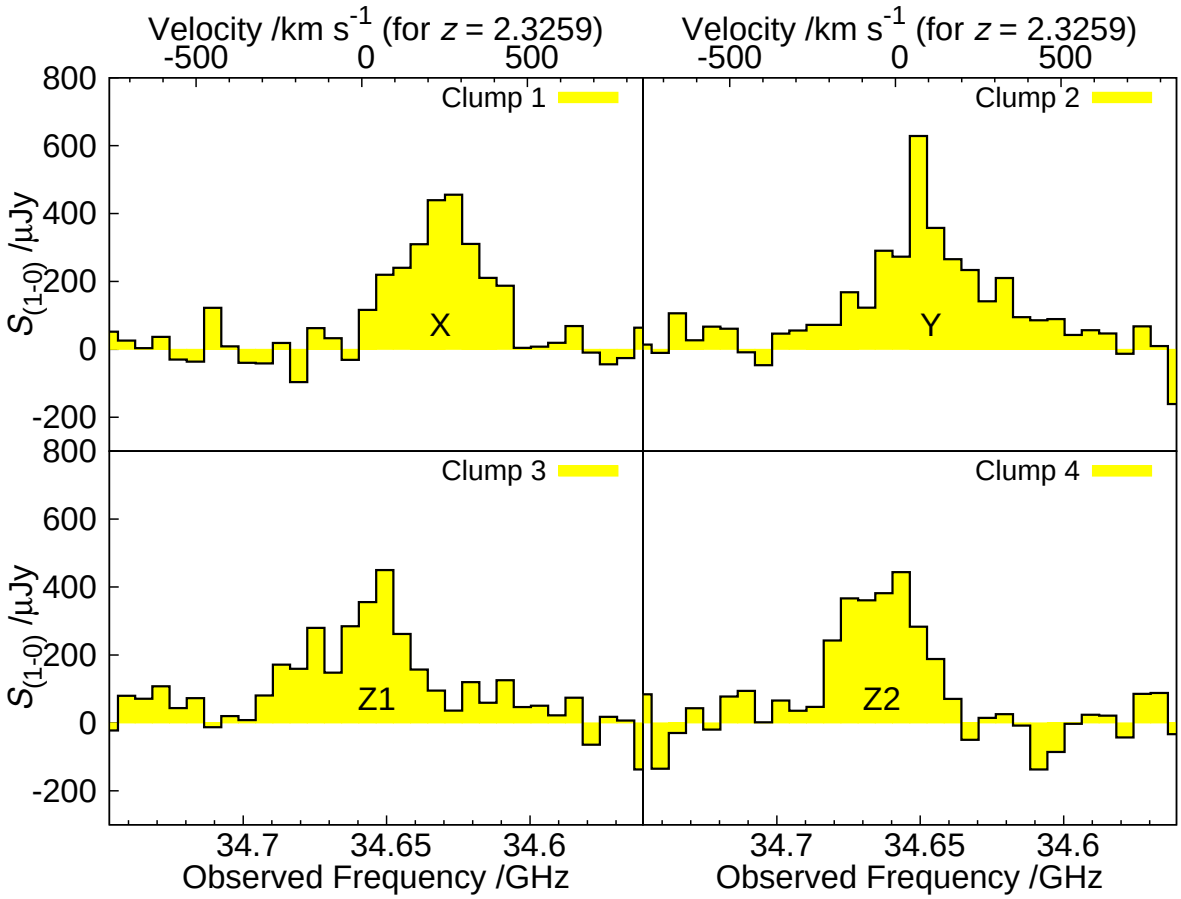

Figure 4.6: ^{12}CO $J = 1-0$ spectra for each of the four clumps identified via the method presented in Section 4.3.3. The velocity offsets seen between the four clumps enable them to be identified as clumps X, Y and $Z1$ and $Z2$ respectively, under the nomenclature of Figure 4.5 and Danielson et al. (2011).

canonical, and treat them as likely GMC analogues which are marginally resolved by the VLA synthesised beam, and as sites within which to study the spatially-resolved ^{12}CO spectral line energy distributions (SLEDs), the star-formation law and far-infrared/radio correlation (FIRRC) at these locations.

Molecular gas properties on ~ 100 pc scales

I begin my analysis of the clump-scale ISM properties by assuming that each clump is a marginally resolved object that fills the VLA synthesised beam, and extracting spectra from the ^{12}CO $J = 1-0$ data cube at each of positions 1–4. The resulting four clump spectra, shown in Figure 4.6, show velocity offsets

with respect to the systematic velocity of SMM J21352. These offsets consist of one clump with a systematically positive velocity (which I identify with the kinematically-resolved component X of Danielson et al., 2011); one clump with a pseudo-Gaussian velocity profile with narrow FWHM and broad FWZI (which matches component Y in the same paper); and two clumps with systematically negative velocities (corresponding to clumps $Z1$ and $Z2$). The correspondence between these two sets of clumps is all the more startling due to the radically different methodologies used to identify them; in Danielson et al. (2011) the clumps are identified purely from the shape of the source-integrated GBT and PdBI spectra, which requires four Gaussian components to achieve an acceptable fit, whereas in the present work the clumps are identified via a pair of independent algorithms which comb the new three-dimensional ^{12}CO $J=1-0$ data cube for emission peaks above a specified S/N cut. Note that whereas emission from clumps $Z1$ and $Z2$ could not be distinguished in the VLA source-averaged ^{12}CO $J=1-0$ spectrum (Figure 4.5), the spatial resolution of these new data enable them to be trivially distinguished in the image plane.

The physical conditions of the gas within these clumps is probed by first determining the observed ^{12}CO SLED of each clump, and then modelling the observed line ratios to constrain the temperature, density and molecular abundance in each clump.

I measure the ^{12}CO SLEDs by placing the four ^{12}CO maps on a common astrometry/pixel scale using the $\mathcal{AIPS}$ task OHGEO, and seeding model maps for each ^{12}CO transition with 8 delta functions at the locations of the clumps (1,2,3,4) and their mirrored counterparts (1a,2a,3a,4a) as identified by SERCH. The 4 north-westerly clumps are constrained to have random flux densities between 0–150% of the peak seen in the corresponding real integrated image, and the flux densities of the four south-easterly clumps are determined relatively via the amplification map, on the assumption that they are mirror images of the northern clumps. In so doing, the clumps are considered to be marginally resolved structures in the ^{12}CO $J=1-0$ map, and fully unresolved objects containing the bulk of the flux in the mid-J maps. Then, the model map is convolved with the appropriate synthesised beam, and the goodness-of-fit of that model map is measured via the χ^2 statistic, where the four degrees of freedom are those of the four independent clump fluxes:

$$\chi^2 = \frac{N_{\rm pix}}{4} \times \frac{\Sigma({\rm Image} - {\rm Model})^2}{\Sigma({\rm Model})^2} \tag{4.3}$$

where $N_{\rm pix}$ is the number of pixels in each image (in each case, a 129×129 pix postage stamp with a pixel scale of 0.04-arcsec).

After 500 fits (one *major cycle*), I determine the set of values for which χ^2 reaches a minimum, re-centre on the best-fitting solutions and shrink the parameter space by 5%, whereupon another set of 500 random clump fluxes are fit within the available parameter space. This process continues for a minimum of 40 major cycles (20,000 fits in all), or until $\chi^2_{\rm min}$ has converged to within 1% across three successive major cycles.

Having thus determined the best-fitting observed SLED for each clump, this is then used to constrain an LVG model, computed using the RADEX radiative transfer code[2] (van der Tak et al., 2007).

RADEX computes the level populations, optical depths and intensities of each of the spectral lines of a chosen set of molecules by introducing the assumptions that: (i) the medium is homogeneous, in which case the escape probability assumption outlined in Chapter 1 holds; (ii) that collisional excitation of ^{12}CO occurs only via interactions with H_2; and (iii) that the velocity widths of all molecular lines are equal for a given cloud. The collision rates used by RADEX are functions of temperature, and are held, along with other physical properties of each molecule, in a database of molecular files maintained by the Leiden Atomic and Molecular Database (LAMBDA[3]), and are interpolated or extrapolated for $T_{\rm k}$ beyond the range contained within the datafile.

A suite of 800,000 model ^{12}CO spectra were generated for each clump (with the line width set appropriately in $\rm km\,s^{-1}$), assuming a spherical cloud geometry, for a grid of input parameters $T_{\rm k}$=20–90 K (in 15 steps of 5 K), n(H_2)=$10^{2-6}\,\rm cm^{-3}$ (in 200 equidistant steps) and $N_{\rm CO} = 4 \times 10^{18-24}\,\rm cm^{-2}$ (in 200 equidistant steps). These values are typical of molecular clouds seen in the local Universe (e.g. Richardson, 1985; Ostriker et al., 2010; Shetty et al., 2011). In each model run, the background temperature was fixed at $T_{\rm CMB} = 2.73 \times (1 + z) = 9.08$ K.

The observed ^{12}CO SLEDs for each of the four clumps are shown with the

[2]http://home.strw.leidenuniv.nl/∼moldata/radex.html
[3]http://home.strw.leidenuniv.nl/ moldata/

corresponding best-fitting models in Figure 4.7. The shapes of the individual SLEDs are qualitatively consistent with the source-averaged SLED seen in Danielson et al. (2011), which may be a consequence of the assumption that the bulk of the mid-J luminosity of the galaxy is contained within these clumps. The SLEDs all peak at $J_{\rm upper} \geq 5$, in keeping with results from studies of local starburst galaxies (e.g. M82 and NGC 6240; Weiß et al., 2005b; Meijerink et al., 2013), AGN (e.g. Mrk 231; van der Werf et al., 2010), and from the few high redshift SMGs thus far to have yielded well-sampled ^{12}CO SLEDs (e.g. GN20 and SMM J14011; Carilli et al., 2010; Sharon et al., 2013, respectively). The large error bars on the observed SLEDs are a result of degeneracies in the process of fitting clump fluxes to the maps, which are themselves a result of the poor angular resolution of the mid-J – particularly $J=3-2$ – PdBI maps.

The goodness-of-fit of these three-parameter models to the data is determined via the χ^2 statistic. With three measured ^{12}CO line intensity ratios to fit a model with three free parameters (and with substantial uncertainty in the measured line ratios due to the poor angular resolution of the mid-J ^{12}CO maps), we may expect to see significant degeneracies between parameters. Such a degeneracy is seen in Figure 4.8, in which I plot contours of constant χ^2 in the n(H_2)–$N_{\rm CO}/\Delta v$ plane, at the temperature for which the formal best fit to the data is achieved. The resulting degeneracies produce a "sausage shape" in the n(H_2)–$N_{\rm CO}/\Delta v$ plane for which χ^2 is a constant, implying that for all models, $N_{\rm CO}/\Delta v \propto$n($H_2$). Such a degeneracy is to be expected for models fit to observations of a single molecular species, which share a common optical depth (Sharon et al., 2013). To fully break these degeneracies and accurately constrain the properties of the ISM would require high angular resolution, high signal-to-noise observations of multiple transitions of a multitude of molecular and atomic species. While for any one species, an LVG model will likely produce degenerate results, study of multiple species, each with their own characteristic optical depth and excitation requirements may be expected to produce a concordance solution, as in Danielson et al. (2011). Nevertheless, with only ^{12}CO data available, models with excessively low n(H_2) and high $N_{\rm CO}/\Delta v$ can be definitively ruled out by introducing the constraint on the clump size that each clump be no more extended than the area covered by the VLA synthesised beam. The minimum-χ^2 fits to the data for the four clumps are summarised in Table 4.4, and span the range $\log\left[{\rm n}({\rm H_2})/{\rm cm^{-3}}\right] = 3.6$–$3.9$,

Table 4.4: RADEX-derived SMM J21352 gas clump properties

Clump	T_k (K)	$\log\left[\mathrm{n(H_2)/cm^{-3}}\right]$	α_{CO} ($\mathrm{K\,km\,s^{-1}\,pc^2}$)	M_{gas} ($\times 10^9\,\mathrm{M_\odot}$)
1	70	3.85 ± 0.37	< 7.78	$< 1.49 \pm 0.47$
2	70	3.59 ± 0.43	< 0.63	$< 0.29 \pm 0.07$
3	30	3.66 ± 0.56	< 9.40	$< 2.13 \pm 0.62$
4	70	3.89 ± 0.10	< 16.1	$< 2.03 \pm 0.77$

$\log\left[(\mathrm{N_{CO}}/\Delta \mathrm{v})/\mathrm{cm^{-2}km^{-1}s}\right] = 15.7$–$16.5$. Three of the clumps have minimum-χ^2 temperatures $T_{\mathrm{k}} \sim 70\,\mathrm{K}$, while the fourth appears to be significantly colder: $T_{\mathrm{k}} \sim 30\,\mathrm{K}$. If the temperatures of the gas and dust are coupled, then this Bimodality in temperature is in agreement with the dual-component dust model advanced by Ivison et al. (2010c) as a good fit to the far-IR SED of SMM J21352.

From the best-fitting models, I compute α_{CO} for each clump by first computing X_{CO}, which relates the column density of molecular hydrogen $\mathrm{N_{H_2}}$ to the velocity-integrated ^{12}CO $J=1$–0 line intensity W_{CO} (Equation 1.25), and then converting to units of $\mathrm{M_\odot\,(K\,km\,s^{-1}\,pc^2)^{-1}}$ via the conversion factor in Equation 1.27. Since RADEX deals with molecular hydrogen in terms of a volume density $\mathrm{n(H_2)}$, we are required to integrate the mean density along a path $\int ds$ (where $\int ds$ is an estimate of the line of sight through each cloud) in order to calculate the column density: $\mathrm{N_{H_2}} = \int \mathrm{n(H_2)} ds$.

This conversion from volume density to column density of $\mathrm{H_2}$ implies that the best α_{CO} is strictly an upper limit; the only estimate available for the sizes of the clumps is the constraint that they be no larger than the VLA synthesised beam ($\sim 130\,\mathrm{pc}$). If the clumps are in fact significantly more compact than this, then α_{CO} scales downward correspondingly.

These upper-limits ($\alpha_{\mathrm{CO}} < 7.78; < 0.63; < 9.40; < 16.1$) span the range of ULIRG-like – Milky Way GMC-like α_{CO}s, and, in conjunction with estimates on L'_{CO} allow upper-limits to the gas masses to be determined ($M_{\mathrm{gas}} < 1.49 \times 10^9; < 2.88 \times 10^8; < 2.13 \times 10^9; < 2.03 \times 10^9$). Depending on whether the total molecular gas mass of SMM J21352 is closer to the firm lower or upper limits determined in Section 4.3.2, these clumps may between them contain 10–60% of the total molecular gas budget of the system.

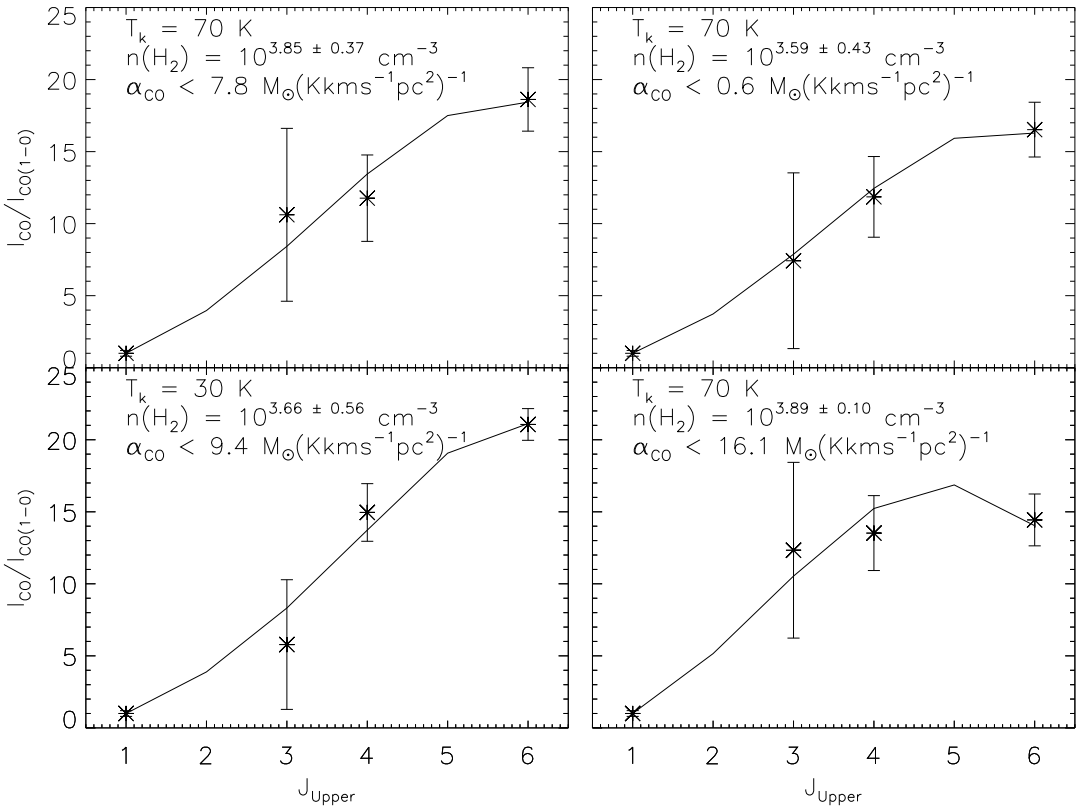

Figure 4.7: ^{12}CO SLEDs of four marginally resolved clumps in SMM J21352, with the model SLEDs from RADEX which best fit the data over-plotted. Models are generated across the parameter space $T_{\rm k}$=20–90 K (in 15 steps of 5 K), n(H_2)=10^{2-4} cm^{-3} (in 200 equidistant steps) and $N_{\rm CO} = 4 \times 10^{18-20}$ cm^{-2} (in 200 equidistant steps). The key physical parameters of the best fitting models are marked on each plot; I recover one clump with gas kinetic temperature $T_{\rm k} = 30$ K and three clumps with $T_{\rm k} = 70$ K, in good agreement with the dust temperature, which is modelled by Ivison et al. (2010c) according to a two component model. We may only compute an upper-limit to $\alpha_{\rm CO}$, due to the explicit assumption made by RADEX that the medium is homogeneous and isotropic, and that the model volume density of H_2, n(H_2) is related to the column density $N_{\rm H_2}$ via $N_{\rm H_2} = \int {\rm n(H_2)} ds$ for a column $\int ds$. I choose $\int ds = 130$ pc, on the assumption that the clouds each fill the VLA beam; if the clouds are significantly smaller than this, then the true column density of H_2 will be proportionally lower, and $\alpha_{\rm CO}$ will be driven downwards.

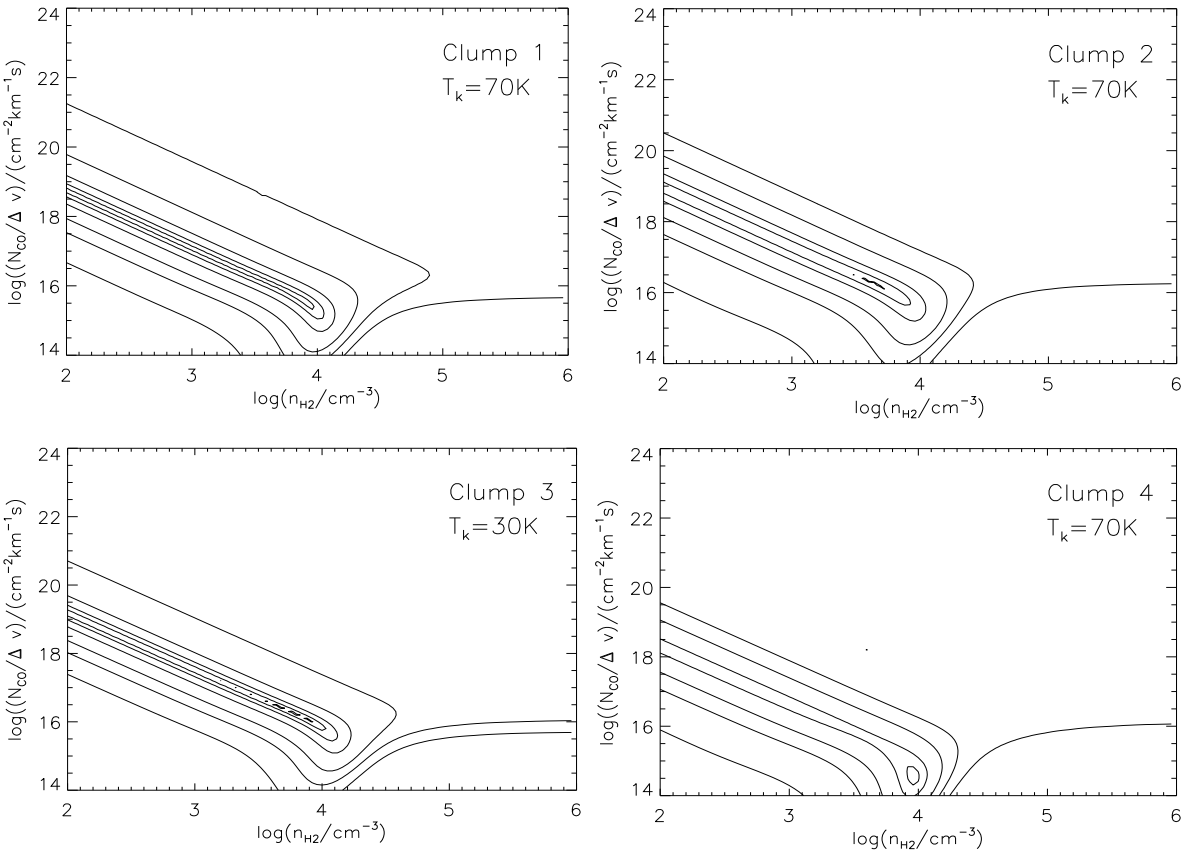

Figure 4.8: Contours of constant χ^2 in the n(H_2)–$N_{CO}/\Delta v$ plane for each of the four clumps, at the temperature which produces the minimum-χ^2 solution. Contours are at $\Delta\chi^2 = 0.1, 0.2, 0.4, 0.8, 1.6....$ With data for only a single molecular species, solutions are degenerate in this plane, however in the future, this degeneracy may be broken by complementary, high-resolution observations of additional molecular species.

The far-infrared/radio correlation

The processes of stellar birth, evolution and death lead to the emission of radiation at multiple wavelengths.

It has long been established that in local star-forming galaxies, there exists a tight correlation between the relative strengths of far-infrared and radio emission (e.g. Helou et al., 1985; Condon et al., 1991) on scales from $\sim 100\,\mathrm{pc}$ up to entire galaxies. Furthermore, this correlation is observed to hold ubiquitously over several orders of magnitude in luminosity, gas surface density and photon energy density, from giant molecular clouds and dwarf galaxies all the way up to the most massive ULIRGs (e.g. Arp 220; Yun et al., 2001).

This correlation is most readily understood within the framework of "calorimetry" (e.g. Voelk, 1989; Lacki & Thompson, 2010), in which UV and optical photons produced by young, massive stars are thought to be captured by dust and re-radiated at infrared wavelengths at a rate that is closely matched by that at which the same massive stars can inject energy in to the ISM via supernova shocks, which accelerate free electrons and positrons, giving rise to synchrotron emission. Provided the duration of the star formation event is greater than the $\sim 10\,\mathrm{Myr}$ timescale on which the first supernovae are produced, then the two processes can reach equilibrium, giving rise to the observed correlation.

The far-infrared/radio correlation (FIRRC) is commonly expressed via the single logarithmic parameter q_{IR}, where

$$q_{\mathrm{IR}} = \log_{10}\left[\frac{S_{\mathrm{IR}}}{3.75\times10^{12}\mathrm{W\,m^{-2}}} \times \frac{\mathrm{W\,m^{-2}\,Hz^{-1}}}{S_{1.4\,\mathrm{GHz}}}\right] \tag{4.4}$$

for 8–1000 μm infrared flux density S_{IR}, and where $S_{1.4\,\mathrm{GHz}}$ is the 1.4-GHz radio flux density, K-corrected assuming $S_\nu \propto \nu^\alpha$ for $\alpha \sim -0.8$.

Recently, Ivison et al. (2010a) exploited the best available *Herschel* and VLA data covering the GOODS-N field with *Spitzer*, SCUBA, AzTEC and MAMBO coverage to investigate the FIRRC from $z = 0$–2. After taking care to exclude strong AGN from the sample, they found that $q_{\mathrm{IR}} = 2.40 \pm 0.24$ invariantly of all other parameters

The apparent ubiquity of the FIRRC makes it a useful tool in defining samples of AGN, which may be seen to deviate from the correlation in one

of two distinct and opposite ways: (i) radio-quiet AGN may contribute to the heating of interstellar dust, while adding very little or no excess radio emission (e.g. Thomson et al., 2012); (ii) radio-loud AGN have powerful radio jets whose emission boosts $S_{1.4\,\mathrm{GHz}}$ by up to 2–4 dex due to the presence of strongly-emitting, compact radio cores and/or extended lobes and jets which are independent of the infrared-emitting interstellar dust (Sanders & Mirabel, 1996).

Using the latest SMA 870-μm continuum and VLA 4–8 GHz continuum images, I investigate the interplay between thermal dust emission and non-thermal synchrotron emission in SMM J21352. The high angular resolution of these maps coupled with the extreme magnification allows us to investigate the FIRRC in two distinct regimes: (i) as a galaxy-averaged quantity, for reference with existing studies at similar redshift; and (ii) at the sites of the gas clumps identified via ^{12}CO $J = 1-0$, by which we may hope to see whether these sub-galaxy units obey calorimetry and behave simply as "scaled down" versions of the whole galaxy, or whether there are any illuminating offsets from $q_{\mathrm{IR}} = 2.4$.

I do this by convolving the radio map with a Gaussian kernel to match the resolution of the SMA map, and measuring both the radio and 870-μm flux densities at the sites of the gas clumps identified via ^{12}CO $J=1-0$, over an area of pixels corresponding to one beam centred on each clump.

To compute S_{IR} at each clump, the observed infrared SED for the entire galaxy (Fig 4.9; Ivison et al., 2010c) was scaled to fit the measured 870-μm flux at that clump. This scaled SED was then integrated between 8–1000μm using the trapezium rule to produce an estimate of the infrared luminosity, L_{IR} of each of the identified clumps. The infrared flux density is then $S_{\mathrm{IR}} = L_{\mathrm{IR}}/4\pi D_{\mathrm{L}}^2$, where D_{L} is the luminosity distance to the source in metres.

The 1.4-GHz radio flux density of each clump is determined by measuring the flux density in the convolved 4–8-GHz radio map across the same clusters of pixels, and then applying a K-correction of the form $S_\nu \propto \nu^\alpha$, where the value $\alpha = -0.75$ is taken as appropriate for SMGs (e.g. Ibar et al., 2010).

Using these new data, I determine $q_{\mathrm{IR}} = 2.40 \pm 0.08$ for the entire galaxy, *cf.* $q_{\mathrm{IR}} = 2.42 \pm 0.06$ as determined by Ivison et al. (2010c) using VLA X-band (3.55 cm) and C-band (4.49 cm) measurements, and a spectral index $\alpha = -0.75$.

At the locations of the clumps, I find $q_{\mathrm{IR}} = 2.45 \pm 0.10$, 2.24 ± 0.13, 2.31 ± 0.10 and 2.59 ± 0.13, the median of which ($< q_{\mathrm{IR}} >= 2.39 \pm 0.23$) is consistent with

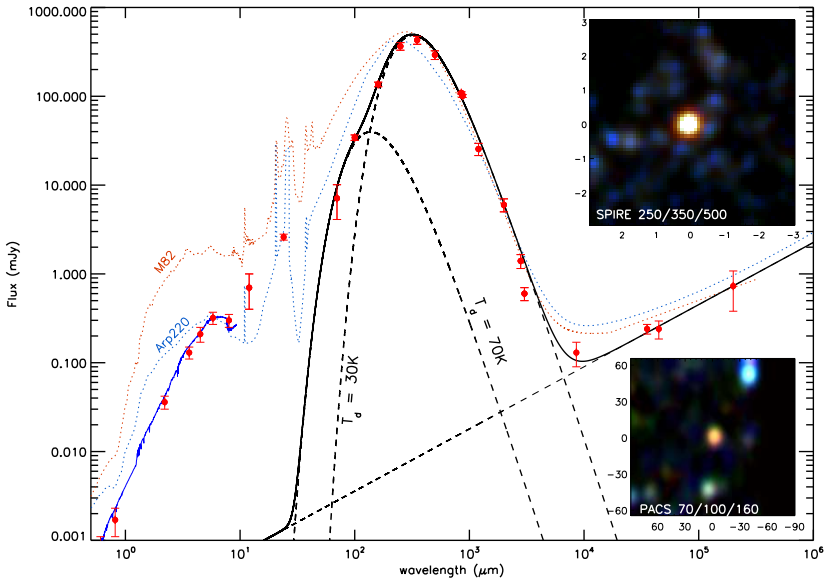

Figure 4.9: Rest-frame near-IR to radio SED of SMM J21352, reproduced from Ivison et al. (2010c). Herschel, SCUBA-2 and VLA observations supplement the photometry presented in Swinbank et al. (2010b). In the rest-frame and after accounting for gravitational magnification, SMM J21352 is less luminous than both Arp 220 and M 82, while the overall shape of the SED is well-fit by a pair of greybodies with characteristic $T_{\rm dust}$ = 30 and 70 K. *Inset:* Colour images generated from the *SPIRE* 250-, 350- and 500-μm and *PACS* 70-, 100 and 160-μm observations.

both the source-averaged value, and with the median value of 250-μm-selected galaxies observed by Ivison et al. (2010a), $< q_{\rm IR} >= 2.40 \pm 0.12$.

The Schmidt-Kennicutt Law

A critical ingredient in any attempt to understand galaxy formation and evolution is a proper characterisation of the processes by which diffuse baryonic matter comes to be locked up in stars. Unfortunately, the spatial scales on which star formation actually occurs remain beyond observational reach for all but the most nearby galaxies, and thus efforts to characterise these processes in distant galaxies are limited to the application of simplified "recipes", or star formation laws. In his seminal paper, Schmidt (1959) introduced the idea that the star formation rate is proportional to some power of the gas density. This relationship is most commonly expressed in terms of the observable surface densities as

$$\Sigma_{\rm SFR} \propto \Sigma_{\rm gas}^{N} \tag{4.5}$$

where a power law index N= 1.40 ± 0.15 has been measured for nearby infrared-selected starburst galaxies (Kennicutt, 1998, leading to this being known as the "Schmidt-Kennicutt" or S-K star formation law). While "gas" here refers in general to HI + H_2, we can make the assumption that distant SMGs are predominantly HI-poor (as their local ULIRG analogues typically are) and that to first order gas mass and H_2 mass are the same thing, in the knowledge that any uncertainty due to this assumption is likely to be overwhelmed by uncertainties in $\alpha_{\rm CO}$ (Ivison et al., 2011).

It has long been established that SMGs follow a Schmidt-type star-formation law (e.g. Greve et al., 2005), albeit apparently offset vertically with respect to the sequence established for gas-rich disk galaxies (e.g. Daddi et al., 2008, 2010; Dannerbauer et al., 2009), with SMGs having an apparently enhanced $L'_{\rm IR}/L_{\rm CO}$ – and hence SFR/$M_{\rm gas}$. This apparent offset has been interpreted as evidence of a dual star formation law at work in the high-redshift Universe, with BzK galaxies typifying the "main sequence" of ongoing, quiescent star formation activity, and SMGs forming stars in shorter-lived, more intense, hyper-efficient spurts due to major merger activity (e.g. Genzel et al., 2010). However, the interpretation of this apparent offset in the S-K law at high-redshift is complicated by the smorgasbord of ^{12}CO lines observed in different galaxy samples, and the range of gas excitation models used to convert them to the appropriate $L'_{\rm CO(1-0)}$, from which the star-formation law is actually deduced.

The high spatial resolution of the latest ^{12}CO $J=1-0$ and SMA rest-frame 870-μm maps for SMM J21352 enable us for the first time to evaluate the S-K relation as a function of position, inside a moderate redshift star-forming galaxy. The synthesised beam of the SMA continuum image is 0.59 × 0.45-arcsec at PA= 49.56°; by convolving the ^{12}CO $J=1$–0 map to this beam – roughly a factor 2× loss in resolution – it is possible to derive the ^{12}CO $J=1-0$ luminosities, $L'_{\rm CO(1-0)}$, of the regions around each of the SERCH-identified clumps in a similar manner to that in which $L_{\rm IR}$ and $S_{1.4\rm GHz}$ were determined in the preceding section.

To convert these observable values in to physical properties it is necessary to adopt the $L_{\rm IR} \rightarrow SFR$ conversion factor of K98, and choose a suitable

value of $\alpha_{\rm CO}$. The lowest of the lower-limits on $\alpha_{\rm CO}$ from my clump analysis is $\alpha_{\rm CO} = 0.63\,{\rm M}_{\odot}\,({\rm K\,km\,s^{-1}\,pc^2})^{-1}$, and I adopt this value of $\alpha_{\rm CO}$ for each of the four clumps; it will not be possible to significantly improve upon this assumption until even higher resolution data better estimate the sizes of the clumps, and thus better constrain the conversion from molecular hydrogen volume density to number density.

For comparison with the literature data, I evaluate both SFR and $M_{\rm gas}$ as surface densities $\Sigma_{\rm SFR}$ and $\Sigma_{\rm gas}$, with units ${\rm M_{\odot}\,yr^{-1}\,kpc^{-2}}$ and ${\rm M_{\odot}\,pc^{-2}}$ respectively; this relies on the same size estimates, both of the galaxy itself, and of the marginally resolved clumps. Star formation rates are derived by measuring the 870-μm flux density of each clump from the SMA map, scaling the SMM J21352 far-infrared-submillimetre-radio SED of Ivison et al. (2010c), and converting the inferred $L_{\rm IR}$ to SFR via the K98 conversion factor. To eventually free ourselves from the assumption that the clumps are merely "scaled-down" versions of the whole galaxy in terms of their far-infrared properties will require significant investment of ALMA time to probe the full, spatially resolved far-IR SED.

Acknowledging these various assumptions, I derive star formation rate surface densities of $\Sigma_{\rm SFR}$ = 70, 130, 100 and $50\,{\rm M_{\odot}\,yr^{-1}\,kpc^{-2}}$ and molecular gas mass surface densities $\Sigma_{\rm gas}$ = 5550, 6030, 5180 and $4330\,{\rm M_{\odot}\,pc^{-2}}$ for the four source-plane clumps, values which place them among the densest star-forming environments seen at high-redshift. Both SMM J21352 and the clumps lie within the scatter of the "observed SK plot" ($L'_{\rm IR}/L'_{\rm CO(1-0)}$; Figure 4.10) at the high and low mass ends respectively, while their positioning on the $\Sigma_{\rm SFR}/\Sigma_{\rm gas}$ plot sees them slightly offset from the "normal" star formation law, although as ever, this observational result needs to be accompanied by the caveat that $\Sigma_{\rm gas}$ estimates are only as robust as the values of $\alpha_{\rm CO}$ used to derive them. Here, by taking the lowest lower-limit on $\alpha_{\rm CO}$ and applying it indiscriminately to all clumps, I have likely biased $\Sigma_{\rm gas}$ low; if this is indeed the case, then at least three of the clumps could plausibly move to the right on the SK plot, and in to better agreement with the high surface density extension of the "normal" star formation law.

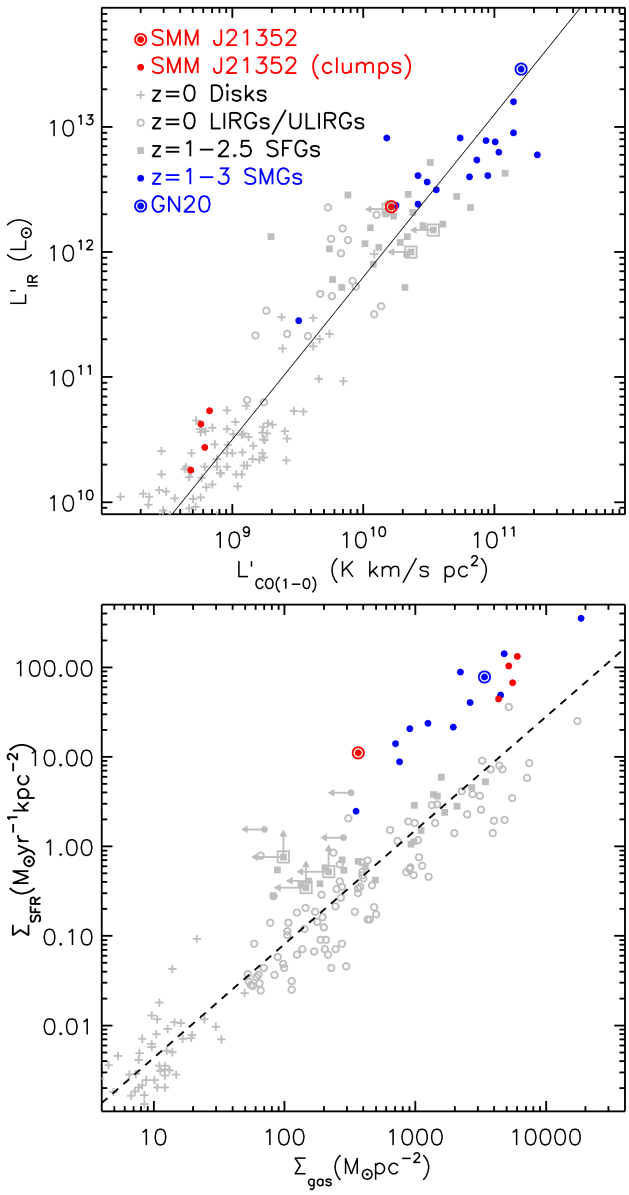

Figure 4.10: The Schmidt-Kennicutt plot, relating star formation and the availability of molecular gas. Local disks, LIRGs and ULIRGs and high-redshift star-forming (BzK) galaxies are taken from Genzel et al. (2010). SMGs with recent ^{12}CO $J=1-0$ measurements, including the GN20 object of Carilli et al. (2010) are shown. *Top:* The "observed" S-K relation. After correction for lensing, SMM J21352 is seen to be a "typical" SMG, while the analysis of the clumps extends the plot at high redshift to luminosities hitherto well below the confusion limit. *Bottom:* The surface density S-K relation, in which we convert the observed ^{12}CO $J=1-0$ luminosities in to gas masses using $\alpha_{\rm CO}=0.8$ for the whole galaxy and $\alpha_{\rm CO}=0.67$ for the clumps (see Section 4.3.3). The clumps in SMM J21352 populate the high-density tail of the "merger sequence"; subsequent downward revision of $\alpha_{\rm CO}$ would move them to the right on the plot, and back towards the "normal" star formation law.

4.4 Discussion and conclusions

I have presented a new, high resolution VLA map and data cube of ^{12}CO $J=1-0$ emission in the strongly lensed but otherwise "typical" SMG, SMM J21352. There being no evidence of flux having been significantly resolved out on long baselines, I consider the new flux, luminosity and gas mass estimates – within 5% of the values quoted by Danielson et al. (2011) based on single-dish GBT measurements – to be minor downward revisions to those figures.

Taking full advantage of the 0.3-arcsec resolving power of the VLA's BnA configuration, I have identified four pairs of clumps in the $J=1-0$ data cube, mirrored about the lensing critical curve. The positions of these clumps are inconsistent with those identified by Swinbank et al. (2010b) in their high-resolution Submillimeter Array map of the galaxy, motivating a re-visitation of the 870-μm continuum data. On close inspection of these data, it was discovered that the structure in the dirty image was dominated by sidelobe structure, and that the CLEANing of these sidelobes had likely led to an interpretation of the morphology of the source which, while qualitatively correct (there are eight identifiable image-plane clumps, consisting of four "real" clumps and four lensed counterparts), was inaccurate as regards the positioning and relative brightnesses of those clumps. A new map from the SMA archival data was made in which previously unused short *uv* spacings were added to the Very EXtended configuration data, yielding a modest degradation in resolution, but with the advantage of vastly better sidelobe structure, and fewer spurious artefacts on the final map. The ^{12}CO $J=1-0$ spectra of these clumps strongly suggest that they are the clumps X, Y, $Z1$ and $Z2$ reported by Danielson et al. (2011), who based their analysis on the decomposition of the ^{12}CO spectra in to multiple Gaussian components.

Having studied the relationships between different ^{12}CO transitions, rest-frame far-infrared emission and radio emission as a function of position within the ISM, it has been possible – for the first time – to investigate the ^{12}CO excitation conditions in ~ 130 pc sub-structures in a star-forming galaxy at $z \sim 2.3$. This has allowed us to determine the likely gas temperatures and molecular hydrogen volume densities, and place plausible upper-limits on the value of the ^{12}CO-to-H_2 conversion factor $\alpha_{\rm CO}$ for each of the clumps, which fall between those normally taken for ULIRGs and Milky Way GMCs. Depending on whether we adopt the

firm upper or lower limits on the total molecular gas in SMM J21352, these clumps may contain between 10–60% of the total molecular gas in the galaxy.

I use a brand-new 4–8 GHz C-band continuum map of SMM J21352 (Frazer Owen, *private communication*) to determine the radio flux density, and, in conjunction with the revised SMA map, test the applicability of the far-infrared/radio correlation to SMM J21352. These new data suggest that SMM J21352 as a whole sits on the correlation ($q_{\rm IR} = 2.40 \pm 0.08$), but that the clumps span a range of $q_{\rm IR} = 2.24$–2.59, which is a greater deviance from the mean than can be accounted for by the formal measurement errors; this may have some interesting implications for the ages of the clumps. As Bressan et al. (2002) point out, within the interpretational framework of calorimetry, slight deviations from the FIRRC are expected for star-forming systems whose luminosity-weighted age is sufficiently young; whereas the dust heating which produces thermal infrared emission is nearly concurrent with the onset of star-formation, the radio spectrum is at early times dominated by thermal HII emission, and only at later times do the first supernovae – which produce the non-thermal synchrotron radio emission – occur. The net effect of these differing timescales is that $q_{\rm IR}$ may go through three key phases: (i) the *starburst phase*, during which $q_{\rm IR}$ may start as high as 3, before reaching a minimum (as low as $q_{\rm IR} = 1.6$) after a few tens of Myr, as the increase in far-infrared emission due to dust heating is beaten by the much faster increase in radio emission as thermal free-free is overtaken by supernova synchrotron emission as the dominant source of radio power; (ii) a *post starburst phase*, during which time the heating of dust by low–intermediate mass stars continues to elevate $S_{\rm IR}$, but the majority of the massive stars that contribute to $L_{1.4\,\rm GHz}$ have already gone nova, resulting in $q_{\rm IR}$ rising upwards to $q_{\rm IR} = 2.4$; and (iii) a *quiescent phase*, which is much longer-lived than either of the preceding phases, and occurs after the heating of dust and SNR have reached equilibrium, when $q_{\rm IR}$ reaches a plateau. Under this interpretation of calorimetry theory, $q_{\rm IR} = 2.4$ ought only to be truly ubiquitous in galaxies whose luminosity-weighted age is greater than a few tens of Myr; for galaxies below this age, $q_{\rm IR} = 2.4$ is still a reasonable average, but one about which there should be significant scatter, reflecting the different timescales on which $S_{\rm IR}$ and $S_{1.4\,\rm GHz}$ are switched on. Thus, the variations seen in $q_{\rm IR}$ for the star-forming clumps within SMM J21352 are not unexpected, however to investigate this idea more rigorously will require

forthcoming ALMA observations of the rest-frame far-infrared emission, whose spatial resolution will surpass that of the existing SMA map, and facilitate direct comparison with the un-tapered VLA C-band continuum map.

Alternatively, the offsets in $q_{\rm IR}$ seen in the clumps may be evidence of differing diffusion timescales and mechanisms for cosmic ray electrons and UV photons in the ISM. Murphy et al. (2006) find similar offsets in the logarithmic 24 μm and 70 μm-to-radio surface brightness ratios for $\sim$ kpc regions within the disks of four nearby star-forming galaxies. These offsets go away when the infrared maps are smoothed with exponential kernels. The broad tails of these exponential kernels compared to the equivalent Gaussian kernels are motivated by empirical "leaky box" cosmic ray electron models (e.g. Bicay & Helou, 1990; Murphy et al., 2006), in which cosmic ray electrons, once formed, escape from the young protostellar environment more quickly than do the thermal infrared photons, leading to the radio maps having a correspondingly larger scale length ($\sim$ 1–5 kpc, *cf.* $\sim$ 100 pc in the infrared) and less clumpy structure than the infrared maps. Similar kpc-scale offsets in the FIRRC in spiral galaxy clumps are seen by Basu et al. (2012) and Dumas et al. (2011), though here the observed correlation is *tighter* in the (young) star-forming arms than in the quiescent inter-arm regions.

There are thus two competing effects which may explain the clump-scale offsets from $q_{\rm IR} = 2.4$ in SMM J21352, each of which operate on different timescales and may lead to opposing conclusions as to the ages of the clumps: (i) that the offsets are due to the $\sim$10 Myr lag between dust heating and the onset of the first supernovae; and (ii) that the offsets are due to the cosmic ray electron diffusion timescale being significantly shorter than that of the infrared photons, which can remain bound up in dust knots for $>$ 100 Myr before eventually escaping via a random walk process. Thus the clumps may be either *younger* than the bulk of the material in SMM J21352, or they may be *older*. The present data do not have the ability to distinguish between these two scenarios, however we can hope to revisit this dichotomy in future if we can obtain an estimate of the timescale on which radiation pressure and mechanical feedback can jointly disrupt the clumps in SMM J21352. Attempts to understand of the details of how galactic velocity fields are coupled to the turbulent dynamics of their constituent clouds – a necessary ingredient of such an age estimate – do, however, remain an area of ongoing research even in the local Universe (Krumholz & Dekel, 2010,

and references therein).

Lastly, I have used the new ^{12}CO $J = 1-0$ VLA data in conjunction with the latest SMA 870-μm continuum map to study the relationship between star formation and molecular gas, both in the galaxy as a whole, and at the positions of the clumps. In the former case, I make use of existing estimates of the total $L_{\rm IR}$ and size (r) from Ivison et al. (2010c) and Swinbank et al. (2011) respectively, while in the latter I again assume the clumps are ~ 130 pc in size, and introduce the additional postulate that the far-infrared SED of Ivison et al. (2010c) can be scaled by the 870-μm flux density of each clump to derive $L'_{\rm IR}$. This appears to be justified on the grounds that radiative transfer modelling of the multi-J ^{12}CO SLEDs reveal gas temperatures of 30 and 70 K, in remarkable agreement with the dual-temperature panchromatic dust SED of Ivison et al. (2010c), suggesting that the clumps are not significantly hotter than the bulk of the galaxy, unless gas and dust are completely thermally decoupled. The implied upper-limits on the ^{12}CO-to-H_2 conversion factor $\alpha_{\rm CO}$ derived via radiative transfer calculations are sensible, though these limits are sensitive to the sizes estimated (and hence the conversion from column density to volume density of H_2) for the clumps. Within the limitations of these assumptions, we see that SMM J21352 and the clumps all lie within the scatter of the $L'_{\rm IR}/L'_{\rm CO}$ plot at the high and the low luminosity ends respectively, in good agreement with the findings and implications of recent ^{12}CO $J=1-0$-based surveys (e.g. Harris et al., 2010; Ivison et al., 2011; Riechers et al., 2011b; Thomson et al., 2012), and that while marginally offset from the "normal" star formation law on the $\Sigma_{\rm SFR}/\Sigma$gas surface density plot, using a lower $\alpha_{\rm CO}$ than the upper limit will shift the clumps in to better agreement with a single star formation law.

Chapter 5

Summary and concluding remarks

In this thesis, I have demonstrated the power of the upgraded Karl G. Jansky VLA as a tool for studying the conditions of the interstellar medium (ISM) in distant star-forming galaxies. I have carried out 120 hours of observations with the VLA during its recent major hardware upgrade, making spatially resolved interferometric maps and data cubes of ^{12}CO $J = 1-0$ emission in a sample of four gravitationally lensed submillimetre galaxies (SMGs) at $z = 2.3$–2.9. ^{12}CO $J = 1-0$ is the best available tracer of the bulk of the molecular gas reservoir, but has only recently become feasible to study at high redshift, due to the increased sensitivity of Ka-band receivers at facilities such as the Robert C. Byrd Green Bank Telescope (GBT) and the VLA. In conjunction with existing observations of the more excited (mid-J) gas phase from the Plateau de Bure Interferometer (PdBI), these new data probing the cold molecular gas reservoir have allowed me to determine the relative importance of quiescent versus star-forming gas, and trace the spatial extent and velocity profiles of these two phases. I have found brightness temperature ratios $r_{(3-2)/(1-0)} < 1$ and line width ratios $\sigma_{\mathrm{CO}(1-0)/\mathrm{CO}(3-2)} > 1$ respectively, suggesting that the cold molecular gas reservoir in SMGs is massive, and extends beyond the region that is visible in the mid-J maps; this result is in keeping with similar observations in the local Universe, and highlights the limitations in previous molecular gas studies in distant galaxies which have typically focused only on the excited gas phase.

The high angular resolution of these new interferometric data has enabled us

to advance beyond simple models which assume a value for the ^{12}CO luminosity to H_2 gas mass conversion factor $\alpha_{\rm CO}$, and begin to think in terms of physically-motivated upper and lower limits to $\alpha_{\rm CO}$, and hence to $M_{\rm gas}$.

For the three moderately lensed SMGs in Chapter 3, upper-limits to $M_{\rm gas}$ were determined by estimating both the size of the gas reservoir and the breadth of the ^{12}CO $J = 1-0$ spectral line, assuming that the gas traces a virialised region, and arguing that the gas mass cannot exceed the implied dynamical mass. Lower limits to $M_{\rm gas}$ were determined by comparing the observed ^{12}CO $J = 3-2/J = 1-0$ brightness temperature ratios with canonical values for cold, quiescent versus star forming gas, and invoking the concept of a "maximal star formation efficiency" $\mathrm{SFE_{max}} = L_{\rm IR}/M_{\rm SF} \leq 500\,\mathrm{L_\odot\,M_\odot^{-1}}$, where $L_{\rm IR}$ is the bolometric infrared luminosity and $M_{\rm SF}$ is the fraction of the gas mass currently engaged in the fuelling of stars. For two of the three galaxies in this subsample – SMM J02399 and SMM J16359 – these upper and lower limits on the gas mass bracket those that would have been determined via the application of an assumed "ULIRG-like" $\alpha_{\rm CO} = 0.8\,\mathrm{M_\odot\,(K\,km\,s^{-1}\,pc^2)^{-1}}$, whereas in the third galaxy – SMM J14009 – the combination of an extremely compact morphology (~ 1 kpc) and relatively high brightness temperature ratio ($r_{(3-2)/(1-0)} = 0.95 \pm 0.12$) complicate the analysis, and lead to an estimate of $M_{\rm gas}$ that is $3\times$ lower than that found via an assumed $\alpha_{\rm CO} = 0.8$. This could imply either that the gas heating in SMM J14009 is dominated not by star formation but by the input of mechanical energy and/or hard X-rays from a hidden AGN, or that the assumption of virialised dynamics made in determining $M_{\rm dyn}$ is wrong.

During the period in which observations were made, the usable bandwidth of the VLA increased by nearly an order of magnitude; as a result, I was able to make 3σ detections of 115-GHz continuum emission in two of the three galaxies in this sample. These observations were used to provide anchorage at the high-frequency end of the radio spectrum, which enabled me – in conjunction with well-sampled far-infrared and radio spectra from the literature – to de-convolve the radio spectra of these two galaxies in to their components arising due to dust, optically-thin free-free emission, and synchrotron emission. The optically-thin free-free emission provides an extinction-free estimate of the star-formation rate, $\mathrm{SFR_{radio}}$, which can be compared with that derived from the infrared luminosity, $\mathrm{SFR_{IR}}$. By comparing these two estimates of SFR, I was able to measure the

excess infrared emission not arising from star formation, but from some other source, presumably a hidden AGN. The resulting AGN bolometric fractions – $L[\mathrm{AGN}]/L_{\mathrm{IR}} = 35\%$ and 55% for SMM J02399 and SMM J14009, respectively – are broadly consistent with existing estimates for these sources based on their mid-IR and X-ray spectral properties.

These estimates of $\mathrm{SFR}_{\mathrm{radio}}$ may be used in conjunction with the updated measurements of M_{gas} from this work to estimate gas consumption timescales $\tau_{\mathrm{gas}} = M_{\mathrm{gas}}/\mathrm{SFR}$ =110 and 180 Myr for SMM J14009 and SMM J02399 respectively, suggesting that they are churning through their massive gas reservoirs rapidly enough to produce the stellar mass of a local giant elliptical galaxy before $z \sim 1$.

Efforts to probe the morphologies and dynamics of these SMGs via position-velocity diagrams have been inconclusive, owing chiefly to the low surface brightness of the ^{12}CO $J = 1-0$ line (even when gravitationally lensed), and the lack of signal-to-noise in these data when they are binned in to frequency channels. Furthermore, while gravitational lensing is responsible for making these SMGs targetable in ^{12}CO $J=1-0$ in the first place, the fact that they are lensed necessitates that their emission be ray-traced through the gravitational potential of the foreground cluster before any meaningful morphological conclusions can be drawn. Had these observations benefitted from a full complement of upgraded EVLA antennas throughout, then there may have been enough signal-to-noise in the data to attempt this, however without such serendipity, consideration of the dynamics of these SMGs is necessarily limited to crude estimates of the spatial extent of the gas reservoir, and limits on the dynamical mass. It is thus not yet possible to say whether the gas in these SMGs traces the potential wells of major mergers, or of massive, rotationally supported disks.

The extreme magnification of SMM J21352–0102 means that that source warrants separate consideration from the rest of the sample for two principle reasons: (i) it allows high-resolution VLA observations to probe physical scales of ~ 130 pc, comparable to the sizes of giant molecular clouds (GMCs), the sites in which star formation is seen to occur in local galaxies; and (ii) it boosts the flux of this otherwise "typical" (*i.e.* star formation-dominated) SMG far enough above the confusion noise for it to be studied in a level of detail that is unprecedented at such high redshift.

I have reduced and presented new ^{12}CO $J=1-0$ data for SMM J21352, revisited archival 870-μm observations with the Submillimeter Array and produced a new, moderately-high resolution map of the rest-frame far-infrared emission, and have presented a new C-band, 4–8 GHz radio continuum map made by Frazer Owen. These I have used in conjunction with existing spectral data cubes of the mid-J ^{12}CO emission from the PdBI to revise existing estimates of the total $M_{\rm gas}$ and the spatial extent of the gas reservoir, and conduct a study of the relationships between dust, star formation, and its fuelling via cold molecular gas in four clumps identified from the ^{12}CO data cube. Within these clumps, I have carried out radiative transfer modelling, constrained by the observed ^{12}CO spectral line energy distribution (SLED), and have derived estimates of the gas density and temperature, as well as plausible upper limits on the appropriate $\alpha_{\rm CO}$ conversion factor for each clump. This modelling produces solutions that are somewhat degenerate in the n(H_2)–$N_{\rm CO}/\Delta v$ plane for a given temperature, T_k, however the formal χ^2-minimum models indicate that between 10–60 % of the total molecular gas in SMM J21352 is contained within these cool ($T_{\rm k}$ = 30–70 K), dense ($\log\left[{\rm n}({\rm H_2})/{\rm cm^{-3}}\right]$ = 3.6–3.9) clumps. We can hope to lower the statistical uncertainty of these fits by observing the mid/high-J ^{12}CO emission at a spatial resolution comparable to that of the new VLA $J=1-0$ map (*i.e.* with ALMA), however to break the fundamental degeneracies in the radiative transfer modelling will require complementary high-resolution observations of optically-thin tracers, such as ^{13}CO and HCN.

By comparing the gas surface density ($\Sigma_{\rm gas}$) from the ^{12}CO $J=1-0$ map, and the star formation surface density ($\Sigma_{\rm SFR}$) from the 870-μm map, and taking the derived upper-limits on $\alpha_{\rm CO}$, we see that these clumps lie at the high density end of the SMG-like "merger sequence" on the Schmidt-Kennicutt plot. However, the data are also consistent with an extension of the "normal" star formation law at high surface density if $\alpha_{\rm CO}$ in each clump is lower than the maximal value that comes from the radiative transfer modelling.

Lastly, using the new 870-μm SMA map with the latest high resolution 4–8 GHz radio continuum map, I have computed $q_{\rm IR}$, the logarithmic ratio of the far infrared flux density to 1.4-GHz radio flux density, both for SMM J21352 as a whole, and for the clumps individually. When taken as a single object, SMM J21352 has $q_{\rm IR} = 2.40\pm0.08$, placing the galaxy exactly on the observed far-

infrared/radio correlation (FIRRC) for star-forming galaxies. $q_{\rm IR}$ for the clumps show tentative evidence of offsets from the FIRRC, which may be due to the differing timescales for the onset (or diffusion) of infrared and radio emission, implying that the clumps are younger (or older) than the bulk of the galaxy.

Taken together, these spatially resolved molecular gas observations have yielded the following key insights into the state of the ISM in dusty, star-forming galaxies at $z \sim 2.5$;

1. Observed ^{12}CO $J=1-0$ luminosities of SMGs, $L'_{\rm CO}$, are ~ 1.5–$2\times$ greater than those which have traditionally been inferred based on observations of the brighter mid-J lines and assumed thermalisation, thus implying that SMGs host more massive gas reservoirs for a given value of $\alpha_{\rm CO}$ than has previously been appreciated.

2. Efforts to calculate $M_{\rm gas}$ from $L'_{\rm CO}$ have begun to move beyond reliance on ad-hoc "disk" and "merger" values for $\alpha_{\rm CO}$, and in to the era in which a variety of observational techniques and modelling can be used to achieve a concordant "best-estimate" for each galaxy or star-forming region.

3. Using appropriate values for $\alpha_{\rm CO}$, I find $M_{\rm gas} \sim 10^{9-10}{\rm M}_\odot$ in SMGs, representing a substantial reservoir of fuel that could sustain a star formation rate of $100\,{\rm M}_\odot\,{\rm yr}^{-1}$ for up to 10–100 Myr.

4. In conjunction with typical stellar masses from the literature (e.g. Hainline et al., 2011), these new observations imply high gas mass fractions $M_{\rm gas}/M_\star = 10$–40%, which may allow SMGs to form the stellar mass of local giant elliptical galaxies by $z \sim 1$.

5. Recent upgrades to the VLA have enabled the first detections of $\nu_{\rm rest} = 115\,{\rm GHz}$ continuum emission at $z \sim 2.5$, providing a novel diagnostic for the bolometric AGN fraction, $L[{\rm AGN}]/L_{\rm IR}$.

6. High resolution interferometric observations through gravitationally lensed clusters remains our best tool for the study of distant galaxies, with concordant high-resolution submillimetre, radio continuum and spectral line data allowing the detailed physics of the dense environments in which stars form to be studied for the first time at $z = 2.3$

In the time since these data were taken, the EVLA hardware upgrade has been completed, broadening its capabilities yet further. In conjunction with a fully operational ALMA array, eMERLIN/VLBI and the forthcoming Square Kilometre Array (SKA) and pathfinders, we are entering a golden age of interferometry, in which radio astronomers will finally be able to produce maps with the resolution and dynamic range to which optical/near-IR astronomers have become accustomed. Together, these new and forthcoming instruments will permit the study of the inter-stellar medium in high-redshift galaxies in exquisite detail, thus enabling the history of galaxy formation and evolution, and of stellar mass build-up in the Universe to be pieced together in unprecedented detail.

Bibliography

Aguirre P., Baker A. J., Menanteau F., Lutz D., Tacconi L. J., 2013, ApJ, 768, 164

Alaghband-Zadeh S. et al., 2012, MNRAS, 424, 2232

Alexander D. M., Bauer F. E., Chapman S. C., Smail I., Blain A. W., Brandt W. N., Ivison R. J., 2005, ApJ, 632, 736

Banerji M., Chapman S. C., Smail I., Alaghband-Zadeh S., Swinbank A. M., Dunlop J. S., Ivison R. J., Blain A. W., 2011, MNRAS, 418, 1071

Barger A. J., Cowie L. L., Sanders D. B., Fulton E., Taniguchi Y., Sato Y., Kawara K., Okuda H., 1998, Nature, 394, 248

Basu A., Roy S., Mitra D., 2012, ApJ, 756, 141

Baugh C. M., Lacey C. G., Frenk C. S., Granato G. L., Silva L., Bressan A., Benson A. J., Cole S., 2005, MNRAS, 356, 1191

Bicay M. D., Helou G., 1990, ApJ, 362, 59

Binney J., Merrifield M., 1998, Galactic Astronomy, Princeton Series in Astrophysics Series. University Press Group Limited

Blain A., Combes F., Draine B., Pfenniger D., Revaz Y., 2003, The Cold Universe: Saas-Fee Advanced Course 32, 2002. Swiss Society for Astrophysics and Astronomy, Saas-Fee advanced course 32, lecture notes 2002, Swiss Society for Astrophysics and Astronomy. Springer

Blain A. W., Chapman S. C., Smail I., Ivison R., 2004, ApJ, 611, 725

Blain A. W., Smail I., Ivison R. J., Kneib J.-P., 1999, MNRAS, 302, 632

Blain A. W., Smail I., Ivison R. J., Kneib J.-P., Frayer D. T., 2002, Phys. Rep., 369, 111

Bothwell M. S. et al., 2013, MNRAS, 429, 3047

Bressan A., Silva L., Granato G. L., 2002, A&A, 392, 377

Briggs D. S., 1995, PhD thesis, New Mexico Institute of Mining and Technology

Brown R. L., Vanden Bout P. A., 1991, AJ, 102, 1956

Bruzual G., Charlot S., 2003, MNRAS, 344, 1000

Caputi K. I., Dole H., Lagache G., McLure R. J., Dunlop J. S., Puget J.-L., Le Floc'h E., Pérez-González P. G., 2006, A&A, 454, 143

Caputi K. I. et al., 2007, ApJ, 660, 97

Carilli C. L. et al., 2002, ApJ, 575, 145

Carilli C. L. et al., 2010, ApJ, 714, 1407

Carilli C. L., Walter F., 2013, ARA&A, 51, 105

Carilli C. L., Yun M. S., 1999, ApJ, 513, L13

Chabrier G., 2003, PASP, 115, 763

Chapman S. C., Blain A. W., Ivison R. J., Smail I. R., 2003, Nature, 422, 695

Chapman S. C., Blain A. W., Smail I., Ivison R. J., 2005, ApJ, 622, 772

Chary R., Elbaz D., 2001, ApJ, 556, 562

Combes F., Boissé P., Mazure A., Blanchard A., 2006, Galaxies and Cosmology, Astronomy and Astrophysics Library. Springer

Condon J. J., 1992, ARA&A, 30, 575

Condon J. J., Anderson M. L., Helou G., 1991, ApJ, 376, 95

Condon J. J., Kaplan D. L., 1998, ApJS, 117, 361

Cornwell T., Braun R., Briggs D. S., 1999, in Astronomical Society of the Pacific Conference Series, Vol. 180, Synthesis Imaging in Radio Astronomy II, Taylor G. B., Carilli C. L., Perley R. A., eds., p. 151

Cox P. et al., 2011, ApJ, 740, 63

Curtis H. D., 1921, Bull. Nat. Res. Coun., 3, 171

Daddi E., Dannerbauer H., Elbaz D., Dickinson M., Morrison G., Stern D., Ravindranath S., 2008, ApJ, 673, L21

Daddi E. et al., 2007, ApJ, 670, 156

Daddi E. et al., 2010, ApJ, 714, L118

Danielson A. L. R. et al., 2011, MNRAS, 410, 1687

Dannerbauer H., Daddi E., Riechers D. A., Walter F., Carilli C. L., Dickinson M., Elbaz D., Morrison G. E., 2009, ApJ, 698, L178

Davé R., Finlator K., Oppenheimer B. D., Fardal M., Katz N., Kereš D., Weinberg D. H., 2010, MNRAS, 404, 1355

de Jong T., Boland W., Dalgarno A., 1980, A&A, 91, 68

Dekel A. et al., 2009, Nature, 457, 451

Downes D., Solomon P. M., 1998, ApJ, 507, 615

Dumas G., Schinnerer E., Tabatabaei F. S., Beck R., Velusamy T., Murphy E., 2011, AJ, 141, 41

Dunlop J. S., 2011, in Astronomical Society of the Pacific Conference Series, Vol. 446, Galaxy Evolution: Infrared to Millimeter Wavelength Perspective, Wang W., Lu J., Luo Z., Yang Z., Hua H., Chen Z., eds., p. 209

Dunne L., Eales S., Edmunds M., Ivison R., Alexander P., Clements D. L., 2000, MNRAS, 315, 115

Ebbels T. M. D., Le Borgne J.-F., Pello R., Ellis R. S., Kneib J.-P., Smail I., Sanahuja B., 1996, MNRAS, 281, L75

Elbaz D. et al., 2011, A&A, 533, A119

Ellis R. S., Smail I., Dressler A., Couch W. J., Oemler, Jr. A., Butcher H., Sharples R. M., 1997, ApJ, 483, 582

Emerson D., 1998, Interpreting Astronomical Spectra. Wiley

Engel H. et al., 2010, ApJ, 724, 233

Farrah D. et al., 2006, ApJ, 641, L17

Finkelstein K. D. et al., 2011, ApJ, 742, 108

Fixsen D. J., Dwek E., Mather J. C., Bennett C. L., Shafer R. A., 1998, ApJ, 508, 123

Floc'h E. L., Cosmos Collaboration, 2011, in Astronomical Society of the Pacific Conference Series, Vol. 446, Galaxy Evolution: Infrared to Millimeter Wavelength Perspective, Wang W., Lu J., Luo Z., Yang Z., Hua H., Chen Z., eds., p. 185

Fomalont E. B., Perley R. A., 1999, in Astronomical Society of the Pacific Conference Series, Vol. 180, Synthesis Imaging in Radio Astronomy II, Taylor G. B., Carilli C. L., Perley R. A., eds., p. 79

Förster Schreiber N. M. et al., 2009, ApJ, 706, 1364

Forte J. C., Vega E. I., Faifer F., 2012, MNRAS, 421, 635

Frayer D. T. et al., 1999, ApJ, 514, L13

Frayer D. T., Ivison R. J., Scoville N. Z., Yun M., Evans A. S., Smail I., Blain A. W., Kneib J.-P., 1998, ApJ, 506, L7

Genzel R., Baker A. J., Tacconi L. J., Lutz D., Cox P., Guilloteau S., Omont A., 2003, ApJ, 584, 633

Genzel R. et al., 1998, ApJ, 498, 579

Genzel R. et al., 2010, MNRAS, 407, 2091

Glover S. C. O., Mac Low M.-M., 2011, MNRAS, 412, 337

Goldreich P., Kwan J., 1974, ApJ, 189, 441

Graham J. R., Liu M. C., 1995, ApJ, 449, L29

Greve T. R. et al., 2005, MNRAS, 359, 1165

Greve T. R., Sommer-Larsen J., 2008, A&A, 480, 335

Hainline L. J., Blain A. W., Smail I., Alexander D. M., Armus L., Chapman S. C., Ivison R. J., 2011, ApJ, 740, 96

Harris A. I. et al., 2012, ApJ, 752, 152

Harris A. I., Baker A. J., Zonak S. G., Sharon C. E., Genzel R., Rauch K., Watts G., Creager R., 2010, ApJ, 723, 1139

Hayward C. C., Kereš D., Jonsson P., Narayanan D., Cox T. J., Hernquist L., 2011, ApJ, 743, 159

Helou G., Bicay M. D., 1993, ApJ, 415, 93

Helou G., Soifer B. T., Rowan-Robinson M., 1985, ApJ, 298, L7

Hempel A., Schaerer D., Egami E., Pelló R., Wise M., Richard J., Le Borgne J.-F., Kneib J.-P., 2008, A&A, 477, 55

Hildebrand R. H., 1983, QJRAS, 24, 267

Hodge J. A., Carilli C. L., Walter F., de Blok W. J. G., Riechers D., Daddi E., Lentati L., 2012, ApJ, 760, 11

Hodge J. A. et al., 2013, ApJ, 768, 91

Hogg D. W., 1999, ArXiv Astrophysics e-prints

Holland W. S. et al., 1999, MNRAS, 303, 659

Hopkins P. F., 2012, MNRAS, 423, 2016

Hubble E. P., 1926, ApJ, 64, 321

Hughes D. H. et al., 1998, Nature, 394, 241

Ibar E., Ivison R. J., Best P. N., Coppin K., Pope A., Smail I., Dunlop J. S., 2010, MNRAS, 401, L53

Iglesias-Páramo J. et al., 2007, ApJ, 670, 279

Israel F. P., 1997, A&A, 328, 471

Ivison R. J. et al., 2002, MNRAS, 337, 1

Ivison R. J. et al., 2010a, A&A, 518, L31

Ivison R. J., Papadopoulos P. P., Smail I., Greve T. R., Thomson A. P., Xilouris E. M., Chapman S. C., 2011, MNRAS, 412, 1913

Ivison R. J. et al., 2012, MNRAS, 425, 1320

Ivison R. J., Smail I., Barger A. J., Kneib J.-P., Blain A. W., Owen F. N., Kerr T. H., Cowie L. L., 2000, MNRAS, 315, 209

Ivison R. J., Smail I., Le Borgne J.-F., Blain A. W., Kneib J.-P., Bezecourt J., Kerr T. H., Davies J. K., 1998, MNRAS, 298, 583

Ivison R. J., Smail I., Papadopoulos P. P., Wold I., Richard J., Swinbank A. M., Kneib J.-P., Owen F. N., 2010b, MNRAS, 404, 198

Ivison R. J. et al., 2013, ApJ, 772, 137

Ivison R. J. et al., 2010c, A&A, 518, L35

Jarosik N. et al., 2011, ApJS, 192, 14

Karim A. et al., 2013, MNRAS, 432, 2

Kennicutt, Jr. R. C., 1998, ApJ, 498, 541

Kneib J.-P., 2010, in The Impact of HST on European Astronomy, Macchetto F. D., ed., Springer, p. 183

Kneib J. P., Mellier Y., Fort B., Mathez G., 1993, A&A, 273, 367

Kneib J.-P., Neri R., Smail I., Blain A., Sheth K., van der Werf P., Knudsen K. K., 2005, A&A, 434, 819

Kneib J.-P., van der Werf P. P., Kraiberg Knudsen K., Smail I., Blain A., Frayer D., Barnard V., Ivison R., 2004, MNRAS, 349, 1211

Kovács A., Chapman S. C., Dowell C. D., Blain A. W., Ivison R. J., Smail I., Phillips T. G., 2006, ApJ, 650, 592

Kovács A. et al., 2010, ApJ, 717, 29

Kroupa P., 2001, MNRAS, 322, 231

Krumholz M. R., Dekel A., 2010, MNRAS, 406, 112

Lacki B. C., Thompson T. A., 2010, ApJ, 717, 196

Lequeux J. L., 2005, The Interstellar Medium. Springer

Leverington D., 1995, A history of astronomy from 1890 to the present, Practical Astronomy Series. Springer-Verlag

Lubin L. M., Postman M., Oke J. B., Ratnatunga K. U., Gunn J. E., Hoessel J. G., Schneider D. P., 1998, AJ, 116, 584

Lutz D., Valiante E., Sturm E., Genzel R., Tacconi L. J., Lehnert M. D., Sternberg A., Baker A. J., 2005, ApJ, 625, L83

Maraston C., 2005, MNRAS, 362, 799

Meijerink R. et al., 2013, ApJ, 762, L16

Meijerink R., Spaans M., Israel F. P., 2006, ApJ, 650, L103

Michalowski M., Hjorth J., Watson D., 2010, A&A, 514, A67

Michalowski M. J., Dunlop J. S., Cirasuolo M., Hjorth J., Hayward C. C., Watson D., 2012, A&A, 541, A85

Morton D. C., Noreau L., 1994, ApJS, 95, 301

Murphy E. J. et al., 2006, ApJ, 638, 157

Murphy E. J. et al., 2011, ApJ, 737, 67

Narayanan D., Krumholz M., Ostriker E. C., Hernquist L., 2011, MNRAS, 418, 664

Narayanan D., Krumholz M. R., Ostriker E. C., Hernquist L., 2012, MNRAS, 421, 3127

Negrello M. et al., 2010, Science, 330, 800

Neri R. et al., 2003, ApJ, 597, L113

Oke J. B. et al., 1995, PASP, 107, 375

Omont A., 2007, Reports on Progress in Physics, 70, 1099

Ostriker E. C., McKee C. F., Leroy A. K., 2010, ApJ, 721, 975

Papadopoulos P. P., Seaquist E. R., 1999, ApJ, 516, 114

Papadopoulos P. P., van der Werf P., Xilouris E., Isaak K. G., Gao Y., 2012, ApJ, 751, 10

Peacock J., 1998, Cosmological Physics, Cambridge Astrophysics Series. Cambridge University Press

Peeters E., Spoon H. W. W., Tielens A. G. G. M., 2004, ApJ, 613, 986

Peraiah A., 2001, An Introduction to Radiative Transfer: Methods and Applications in Astrophysics. Cambridge University Press

Perley R. A., Chandler C. J., Butler B. J., Wrobel J. M., 2011, ApJ, 739, L1

Perley R. A., Dreher J. W., Cowan J. J., 1984, ApJ, 285, L35

Pilbratt G. L. et al., 2010, A&A, 518, L1

Pope A. et al., 2008, ApJ, 675, 1171

Pope A. et al., 2006, MNRAS, 370, 1185

Richardson K. J., 1985, PhD thesis, Department of Physics, Queen Mary College, University of London

Riechers D. A. et al., 2013, Nature, 496, 329

Riechers D. A. et al., 2010, ApJ, 720, L131

Riechers D. A. et al., 2011a, ApJ, 733, L11

Riechers D. A., Hodge J., Walter F., Carilli C. L., Bertoldi F., 2011b, ApJ, 739, L31

Robertson H. P., 1935, ApJ, 82, 284

Rodighiero G. et al., 2010, A&A, 518, L25

Rodighiero G. et al., 2011, ApJ, 739, L40

Rowan-Robinson M. et al., 1991, Nature, 351, 719

Salpeter E. E., 1955, ApJ, 121, 161

Sanders D. B., Mirabel I. F., 1996, ARA&A, 34, 749

Schmidt M., 1959, ApJ, 129, 243

Schwab F. R., 1980, in Society of Photo-Optical Instrumentation Engineers (SPIE) Conference Series, Vol. 231, Society of Photo-Optical Instrumentation Engineers (SPIE) Conference Series, Rhodes W. T., ed., pp. 18–25

Schwab F. R., 1984, AJ, 89, 1076

Scoville N., 2004, in Astronomical Society of the Pacific Conference Series, Vol. 320, The Neutral ISM in Starburst Galaxies, Aalto S., Huttemeister S., Pedlar A., eds., p. 253

Seaquist E. R., Ivison R. J., Hall P. J., 1995, MNRAS, 276, 867

Serjeant S. et al., 2008, MNRAS, 386, 1907

Shapley A. E., Steidel C. C., Adelberger K. L., Dickinson M., Giavalisco M., Pettini M., 2001, ApJ, 562, 95

Shapley H., 1921, Bull. Nat. Res. Coun., 3, 194

Sharon C. E., Baker A. J., Harris A. I., Thomson A. P., 2013, ApJ, 765, 6

Shetty R., Glover S. C., Dullemond C. P., Klessen R. S., 2011, MNRAS, 412, 1686

Siringo G. et al., 2009, A&A, 497, 945

Sjouwerman L. O., Pihlström Y. M., 2008, ApJ, 681, 1287

Slipher V. M., 1917, Lowell Observatory Bulletin, 3, 59

Smail I., Ivison R., Blain A., Kneib J. P., Owen F., 2000a, in Astronomical Society of the Pacific Conference Series, Vol. 195, Imaging the Universe in Three Dimensions, van Breugel W., Bland-Hawthorn J., eds., p. 248

Smail I., Ivison R. J., Blain A. W., 1997, ApJ, 490, L5

Smail I., Ivison R. J., Blain A. W., Kneib J.-P., 2002, MNRAS, 331, 495

Smail I., Ivison R. J., Owen F. N., Blain A. W., Kneib J.-P., 2000b, ApJ, 528, 612

Smolčić V. et al., 2012, A&A, 548, A4

Solomon P. M., Barrett J. W., 1991, in IAU Symposium, Vol. 146, Dynamics of Galaxies and Their Molecular Cloud Distributions, Combes F., Casoli F., eds., p. 235

Solomon P. M., Downes D., Radford S. J. E., 1992, ApJ, 398, L29

Spitzer L., 1987, Dynamical evolution of globular clusters. Princeton University Press

Springel V. et al., 2005, Nature, 435, 629

Stone E. C., Miner E. D., 1989, Science, 246, 1417

Swinbank A. M., Chapman S. C., Smail I., Lindner C., Borys C., Blain A. W., Ivison R. J., Lewis G. F., 2006, MNRAS, 371, 465

Swinbank A. M. et al., 2008, MNRAS, 391, 420

Swinbank A. M. et al., 2011, ApJ, 742, 11

Swinbank A. M. et al., 2005, MNRAS, 359, 401

Swinbank A. M. et al., 2010a, MNRAS, 405, 234

Swinbank A. M. et al., 2010b, Nature, 464, 733

Tacconi L. J. et al., 2008, ApJ, 680, 246

Tacconi L. J. et al., 2006, ApJ, 640, 228

Targett T. A. et al., 2013, MNRAS, 432, 2012

Targett T. A., Dunlop J. S., McLure R. J., Best P. N., Cirasuolo M., Almaini O., 2011, MNRAS, 412, 295

Taylor G., Carilli C., Perley R., (U.S.) N. R. A. O., 1999, Synthesis imaging in radio astronomy II: a collection of lectures from the Sixth NRAO/NMIMT Synthesis Imaging Summer School, held at Socorro, New Mexico, USA, 17-23 June, 1998, Astronomical Society of the Pacific conference series No. v. 2. Astronomical Society of the Pacific

Thompson A., Moran J., George W. Swenson J., 2008, Interferometry and Synthesis in Radio Astronomy. Wiley

Thompson A. R., 1999, in Astronomical Society of the Pacific Conference Series, Vol. 180, Synthesis Imaging in Radio Astronomy II, Taylor G. B., Carilli C. L., Perley R. A., eds., p. 11

Thomson A. P. et al., 2012, MNRAS, 425, 2203

Tielens A. G. G. M., 2005, The Physics and Chemistry of the Interstellar Medium. Cambridge University Press

Uson J. M., Bagri D. S., Cornwell T. J., 1991, ApJ, 377, L65

Valiante E., Lutz D., Sturm E., Genzel R., Tacconi L. J., Lehnert M. D., Baker A. J., 2007, ApJ, 660, 1060

van der Tak F. F. S., Black J. H., Schöier F. L., Jansen D. J., van Dishoeck E. F., 2007, A&A, 468, 627

van der Werf P. P. et al., 2010, A&A, 518, L42

Voelk H. J., 1989, A&A, 218, 67

Walker A. G., 1937, Proceedings of the London Mathematical Society, s2-42, 90

Walker M. G., Mateo M., Olszewski E. W., Peñarrubia J., Wyn Evans N., Gilmore G., 2009, ApJ, 704, 1274

Walter F., Weiss A., Scoville N., 2002, ApJ, 580, L21

Wardlow J. L., 2010, PhD thesis, Department of Physics, University of Durham

Wardlow J. L. et al., 2011, MNRAS, 415, 1479

Weiß A., Downes D., Walter F., Henkel C., 2005a, A&A, 440, L45

Weiß A., Ivison R. J., Downes D., Walter F., Cirasuolo M., Menten K. M., 2009, ApJ, 705, L45

Weiß A., Neininger N., Henkel C., Stutzki J., Klein U., 2001, ApJ, 554, L143

Weiß A., Walter F., Scoville N. Z., 2005b, A&A, 438, 533

Williams J. P., de Geus E. J., Blitz L., 1994, ApJ, 428, 693

Wilson T., Rohlfs K., Hüttemeister S., 2009, Tools of Radio Astronomy, Astronomy and Astrophysics Library. Springer

Young J. S., Scoville N. Z., 1991, ARA&A, 29, 581

Yun M. S., Carilli C. L., 2002, ApJ, 568, 88

Yun M. S., Reddy N. A., Condon J. J., 2001, ApJ, 554, 803

Publications

Ivison, R. J, Papadopoulos, P. P., Smail, I., Greve, T. R., **Thomson, A. P.**, Xilouris, E. M. and Chapman, S. C.
Tracing the molecular gas in distant submillimetre galaxies via CO(1-0) imaging with the Expanded Very Large Array, MNRAS, 2011, 412, 1913

Swinbank, A. M., Papadopoulos, P. P., Cox, P., Krips, M., Ivison, R. J., Smail, I., **Thomson, A. P.**, Neri, R., Richard, J. and Ebeling, H.
The Interstellar Medium in Distant Star-forming Galaxies: Turbulent Pressure, Fragmentation, and Cloud Scaling Relations in a Dense Gas Disk at z = 2.3, ApJ, 2011, 742, 11

Thomson, A. P. and Ivison, R. J. and Smail, I. and Swinbank, A. M. and Weiss, A. and Kneib, J.-P. and Papadopoulos, P. P. and Baker, A. J. and Sharon, C. E. and van Moorsel, G. A.
VLA imaging of ^{12}CO $J = 1 - 0$ and free-free emission in lensed submillimetre galaxies, MNRAS, 2012, 425, 2203

Sharon, C. E., Baker, A. J., Harris, A. I., **Thomson. A. P.**
VLA mapping of the CO(1-0) line in SMM J14011+0252, ApJ, 2013, 765, 6

Riechers, D. A. and Bradford, C. M. and Clements, D. L. and Dowell, C. D. and Perez-Fournon, I. and Ivison, R. J. and Bridge, C. and Conley, A. and Fu, H. and Vieira, J. D. and Wardlow, J. and Calanog, J. and Cooray, A. and Hurley, P. and Neri, R. and Kamenetzky, J. and Aguirre, J. E. and Altieri, B. and Arumugam, V. and Benford, D. J. and Bethermin, M. and Bock, J. and Burgarella, D. and Cabrera-Lavers, A. and Chapman, S. C. and Cox, P. and Dunlop, J. S. and Earle, L. and Farrah, D. and Ferrero, P. and Franceschini, A. and Gavazzi, R. and Glenn, J. and Gonzalez Solares, E. A. and Gurwell, M. A. and Halpern, M. and Hatziminaoglou, E. and Hyde, A. and Ibar, E. and Kovacs, A. and Krips, M. and Lupu, R. E. and Maloney, P. R. and Martinez-Navajas, P. and Matsuhara, H. and Murphy, E. J. and Naylor, B. J. and Nguyen, H. T. and Oliver, S. J. and Omont, A. and Page, M. J. and Petitpas, G. and Rangwala, N. and Roseboom, I. G. and Scott, D. and Smith, A. J. and Staguhn, J. G. and Streblyanska, A. and **Thomson, A. P.** and Valtchanov, I. and Viero, M. and Wang, L. and Zemcov, M. and Zmuidzinas, J.
A Dust-Obscured Massive Maximum-Starburst Galaxy at a Redshift of 6.34, arXiv:1304.4256